

Electronic Theses and Dissertations, 2004-2019

2018

Electrochemical Microsensors for In Situ Monitoring of Chemical Compounds in Engineered and Natural Aquatic Systems

Jared Church
University of Central Florida

 Part of the [Environmental Engineering Commons](#)
Find similar works at: <https://stars.library.ucf.edu/etd>
University of Central Florida Libraries <http://library.ucf.edu>

This Doctoral Dissertation (Open Access) is brought to you for free and open access by STARS. It has been accepted for inclusion in Electronic Theses and Dissertations, 2004-2019 by an authorized administrator of STARS. For more information, please contact STARS@ucf.edu.

STARS Citation

Church, Jared, "Electrochemical Microsensors for In Situ Monitoring of Chemical Compounds in Engineered and Natural Aquatic Systems" (2018). *Electronic Theses and Dissertations, 2004-2019*. 6370. <https://stars.library.ucf.edu/etd/6370>

ELECTROCHEMICAL MICROSENSORS FOR *IN SITU* MONITORING OF CHEMICAL
COMPOUNDS IN ENGINEERED AND NATURAL AQUATIC SYSTEMS

by

JARED K. CHURCH

B.A. Chemistry, University of South Florida, 2012

M.S. Env.E., University of Central Florida, 2015

A dissertation submitted in partial fulfillment of the requirements
for the degree of Doctor of Philosophy
in the Department of Civil, Environmental, and Construction Engineering
in the College of Engineering and Computer Science
at the University of Central Florida
Orlando, Florida

Summer Term
2018

Major Professor: Woo Hyung Lee

© 2018 Jared Church

ABSTRACT

The adaption of needle-type electrochemical microsensor (or microelectrode) techniques to environmental science and engineering systems has transformed how we understand mass transport in biotic and abiotic processes. Their small tip diameter (5-20 μm) makes them a unique experimental tool for direct measurements of analytes with high spatial and temporal resolutions, providing a quantitative analysis of flux, diffusion, and reaction rate at a microscale that cannot be obtained using conventional analytical tools. However, their applications have been primarily limited to understanding mass transport dynamics and kinetics in biofilms. With the advancement of sensor fabrication and utilization techniques, their potential applications can surpass conventional biofilm processes. In this dissertation, microsensors were utilized to elucidate mass transport and chemical reactions in multidisciplinary research areas including biological nutrient uptake, oily wastewater treatment, photocatalytic disinfection, and plant disease management, which have not yet explored using this emerging technology.

The main objective of this work was to develop novel microsensors and use them for better understanding various natural and engineered aquatic systems. These include; 1) investigating localized photo-aeration and algal-bacterial symbiotic interaction in an advanced algal-bacterial biofilm process for nutrient removal from wastewater, 2) characterizing oil-in-water emulsions for better understanding bilge water emulsion stability, 3) evaluating sun-light driven photocatalytic reactions using a novel MoS_2 nanofilm for water disinfection and microcystins-LR removal, 4) developing a zinc ion-selective microsensor and applying them for monitoring the transport of zinc in citrus trees, and 5) integrating heavy metal detection using anodic stripping voltammetry (ASV) in a microelectrode platform for plant applications.

Overall, microsensors capable of measuring pH, oxidation-potential reduction (ORP), dissolved oxygen (DO), ammonia (NH₃), hydrogen peroxide (H₂O₂), and zinc (Zn²⁺) were developed and applied to the systems described above to significantly contribute to a better understanding of interfacial transport mechanisms in various natural and engineered systems.

ACKNOWLEDGMENTS

I thank all who contributed in the completion of this thesis in one way or another. First, I would like to give thanks to God without whom nothing is possible.

I am so grateful for my advisor, Dr. Woo Hyoung Lee, who guided me with understanding and generous guidance and support. With his ambitious attitude, I was able to immerse myself in a broad range of research involvement. I would also like to thank my dissertation committee, Dr. Andrew Randall, Dr. Karin Chumbimuni-Torres, and Dr. Anwar Sadmani for their guidance and encouragement during this work.

I would like to thank my collaborators; Stephanie Armas, Parth Patel, Ashraful Islam, Dr. Eric Jung, Dr. Hodon Ryu, and the MISA team for their support and professionalism. I express deep gratitude to the NSWCCD, EPA, NASA and MISA center for funding this research. I especially thank Danielle Paynter, Sang Lee, and Dr. Swadeshmukul Santra for their cooperation and support.

I express my thanks to Maria Real-Robert for her guidance in the lab, from whom I learned the analytic techniques needed for the completion of this research. I would also like to thank my research group friends: Dr. Xiangmeng Ma, Dr. Jaehoon Wang, Faris Munshi, Ikenna Ezeodurukwe, Conner Thompson, and Dr. Xiaochen Wang for their help with laboratory work and support.

Finally, I dedicate this work to my wife, Haillie, for her devotion and endless support. I thank my parents and family and parents-in-law and their family members for their love, support and endless encouragement.

TABLE OF CONTENTS

LIST OF FIGURES	xii
LIST OF TABLES	xviii
CHAPTER ONE: INTRODUCTION.....	1
Goals and objectives.....	3
Dissertation Organization.....	3
CHAPTER TWO: MASS TRANSPORT IN ENVIRONMENTAL ENGINEERING: A LITERATURE REVIEW	6
Introduction	6
Diffusive Mass Transport.....	7
Diffusive Transport Processes in Environmental Engineering	9
Abiotic mass transport processes.....	10
Biotic mass transport processes.....	11
References	16
CHAPTER THREE: APPLICATION OF MICROSENSORS TO ALGAL-BACTERIAL BIOFILMS FOR ADVANCED WASTEWATER TREATMENT	18
Abstract	18
Introduction	19
Materials and Methods	21
Microalgae cultivation, bacteria inoculation, and synthetic wastewater preparation	21
Photo-SBR.....	22
Analytical methods	23

Microprofiling	24
Illumina sequencing.....	26
Results	27
Nutrient removal and biomass growth.....	27
Photo-aeration using microalgae	31
Interactions between algal and bacteria biofilms	35
Genetic diversity of algae-bacteria consortia for wastewater treatment.....	36
Discussion	39
MAIFAS vs. suspended micro-algae bacteria consortium for nutrient removal in wastewater	39
Effect of Chl. <i>a</i> to biomass ratio on nutrient removal	41
Interactions between algal and bacteria biofilms	43
Challenges and future prospects.....	43
Conclusions	44
References	45
CHAPTER FOUR: APPLICATION OF MICROSENSORS TO BILGE WATER EMULSIONS FOR <i>IN SITU</i> CHARACTERIZATION	48
Abstract	48
Introduction	49
Materials and Methods	51
Preparation of Emulsions.....	51
Characterization of Bulk Properties.	52

<i>In Situ</i> Emulsion Characterization Using Microsensors.....	53
Results and Discussion.....	55
Visual Observations.....	55
Contact Angle	56
Interfacial Surface Tension.....	58
CLSM Analysis	59
Chemical Microprofiles of Oil Water Interfaces.....	61
Effect of Mass Transport on the Stability of Simulated Bilge water Emulsions.....	68
Conclusions	69
References	71
CHAPTER FIVE: APPLICATION OF MICROSENSORS FOR CHARATERIZATION OF A NOVEL NOBLE METAL-COATED MoS ₂ NANOFILM PHOTOCATALYST FOR DEGRADATION OF EMERGING WATER CONTAMINATS	74
Abstract	74
Introduction	75
Materials and Methods	77
Synthesis and validation of MoS ₂ films with vertically aligned layers	77
Photocatalytic degradation of MC-LR using microsensors.....	79
XTT reduction assay for monitoring ROS production	80
Degradation of MC-LR	80
Results and Discussion.....	81
Conclusion.....	94

References	95
 CHAPTER SIX: APPLICATION OF MICROSENSORS TO CITRUS PLANTS FOR DETERMING THE FOLIAR UPTAKE OF Zn ²⁺ IN HLB TREATMENTS	
Abstract	99
Introduction	100
Materials and Methods	102
Zinc Ion-Selective Membrane Cocktail.....	102
Preparation of Zn ²⁺ SC- μ -ISEs.....	102
Characterization of Zn ²⁺ SC- μ -ISEs.....	104
Determination of ion fluxes.....	105
Results and Discussion.....	107
Sensor Characterization.....	107
Surface profiling.....	109
Conclusion.....	112
References	114
 CHAPTER SEVEN: A NOVEL APPROACH FOR <i>IN SITU</i> MONITORING OF Zn ²⁺ IN CITRUS PLANTS USING TWO-STEP SQUARE WAVE ANODIC STRIPPING VOLTAMMETRY	
Abstract	117
Introduction	117
Methods.....	120
Metallic bismuth microelectrode design and fabrication	120

Microelectrode performance evaluation using SWASV	121
In situ application to citrus leaves	122
Results and discussion.....	123
Zn ²⁺ detection using two-step SWASV	123
Effect of plant pH on microelectrode response	125
Effect of tip size and mass transfer on SWASV response.....	126
In situ detection of Zn ²⁺ using SWASV in the vascular bundle of citrus plants	129
Conclusions	131
References	133
CHAPTER EIGHT: CONCLUSIONS, IMPACTS, AND OUTLOOK.....	135
Conclusions	135
Broader Impacts and Outlook	138
APPENDIX A: COPYRIGHT USE OF PUBLISHED MANUSCRIPTS.....	139
APPENDIX B: SUPPLEMENTAL INFORMATION: APPLICATION OF MICROSENSORS TO ALGAL-BACTERIAL BIOFILMS FOR ADVANCED WASTEWATER TREATMENT	142
APPENDIX C: SUPPLEMENTAL INFORMATION: APPLICATION OF MICROSENSORS TO BILGE WATER EMULSIONS FOR <i>IN SITU</i> CHARACTERIZATION.....	145
APPENDIX D: SUPPLEMENTAL INFORMATION: APPLICATION OF MICROSENSORS FOR CHARACTERIZATION OF A NOVEL NOBLE METAL-COATED MoS ₂ NANOFILM PHOTOCATALYST FOR DEGRADATION OF EMERGING WATER CONTAMINANTS ..	156
MoS ₂ adsorption model.....	157
ROS monitoring using XTT	158

APPENDIX E: SUPPLEMENTAL INFORMATION: CHAPTER 7: A NOVEL APPROACH
FOR *IN SITU* MONITORING OF Zn²⁺ IN CITRUS PLANTS USING TWO-STEP SQUARE
WAVE ANODIC STRIPPING VOLTAMMETRY..... 160

LIST OF FIGURES

Figure 1- 1. Typical experimental setup for microprofiling and examples of microprofiling data and surface mapping data.....	2
Figure 2- 1. Illustration of diffusive mass transport as a function of time where (a) is the time the chemical was injected and (b) is the chemical gradient formed by diffusion (adopted from Logan (2000))......	8
Figure 2- 2. Substrate concentration profile and flow velocity distribution near and within a biofilm. (From Lewandowski and Beyenal (2013)).	11
Figure 2- 3. a) Diagram of a typical microprofiling experimental set up and b) typical microprofile.....	14
Figure 3- 1. Schematic diagram of microalgae-based IFAS (MAIFAS) SBR and two controls (IFAS SBR and algae SBR without IFAS media).	22
Figure 3- 2. (a) pH, (b) ammonia, (c) COD and (d) total phosphorus (TP) effluent changes in IFAS control, MAIFAS and suspended algae control SBRs over 150 days. Mechanical aeration was applied to all reactors during the aerobic sequence of Phase I. Only light was applied to MAIFAS and suspended reactors during the aerobic sequence of Phase II.	28
Figure 3- 3. (a) MLSS, (b) MLVSS, (c) Chl. <i>a</i> and (d) Chl. <i>a</i> /biomass ratio in IFAS control, MAIFAS and suspended algae control SBRs over 150 days. Biomass samples were taken during the aerobic phase. Mechanical aeration was applied to all reactors during the aerobic sequence of Phase I. Only light was applied to MAIFAS and suspended reactors during the aerobic sequence of Phase II.	30
Figure 3- 4. DO concentrations during an SBR cycle after (a) 30, (b) 60 and (c) 90 days of growth. Mechanical aeration was applied to IFAS control during aerobic phase. $76.2 \mu\text{mol m}^{-2} \text{S}^{-1}$	

¹ of fluorescent light (no mechanical aeration) was applied to the MAIFAS and Suspended reactors during aerobic phase.....	32
Figure 3- 5. DO microprofiles of MAIFAS biofilms under 76.2 $\mu\text{mol m}^{-2} \text{S}^{-1}$ of white fluorescent light and darkness after (a) 40 days, (b) 80 days, (c) 130 days and (d) 150 days of growth. Reference lines represent biofilm thickness over time.....	34
Figure 3- 6. Cross-sectional image ($\times 40$ magnification and 50 μm thickness) of MAIFAS biofilm at 130 and 160 days. The biofilm was mounted in tissue freezing media.	35
Figure 3- 7. (a) pH and (b) ammonia microprofiles of MAIFAS biofilms under 76.2 $\mu\text{mol m}^{-2} \text{S}^{-1}$ of white fluorescent light and darkness after 140 days of growth. Reference lines represent biofilm thickness over time.....	36
Figure 3- 8 Effect of Chl. <i>a</i> to biomass ratio on a) ammonia removal and b) phosphorus removal during mechanical aeration (Phase I) and c) ammonia removal and d) phosphorus removal during photoaeration (Phase II).....	42
Figure 4- 1. Visual observation of various oil-in-water emulsion samples over time. The surfactant concentration of 100 ppm was used to prepare the macroemulsion samples.	56
Figure 4- 2. The effects of NaCl concentrations on (a) the static contact angle of water (DI water only, 100 ppm SDS, or Triton X-100) in oil (NSBM #4) and (b) the surface tension of water-in-oil pendant drops. Temp. was constant at 24°C. Quartz was used as a substrate for contact angle measurements. Waiting time was 60 s for each reading. Interfacial tension of either water-in-oil or oil-in-water showed similar trends.	59
Figure 4- 3. CLSM images of emulsions prepared with 100 ppm SDS or 100 ppm Triton X-100 at various salinities at the initial and 24-hour interval. All samples were taken at the middle of the emulsion layer.	61

Figure 4- 4. Spatial pH changes in (a) a NSBM #4 and surfactant sample (100 ppm Triton X-100 vs. SDS) and (b) a mineral oil and surfactant sample. 0 μm represents the oil-water interface. DI water only was used to prepare surfactant solution. 63

Figure 4- 5. The effects of anionic surfactant and salinity on the spatial and temporal pH, DO, and ORP changes in oil-in-water emulsion (1% NSBM #4 + SDS). (a) pH profiles without NaCl, (b) pH profiles with 0.1M NaCl, (c) DO profiles without NaCl, (d) DO profiles with 0.1M NaCl, (e) ORP profiles without NaCl, and (f) pH profiles with 0.1M NaCl. 0 μm represents the point at which the sensor signal was obtained by contact with the oil. The interface between oil and emulsion was changed over time within the grey area in each profile. 66

Figure 4- 6. The effects of non-ionic surfactant and salinity on the spatial and temporal pH, DO, and ORP changes in oil-in-water emulsion (1% NSBM #4 + Triton X-100). (a) pH profiles without NaCl, (b) pH profiles with 0.1M NaCl, (c) DO profiles without NaCl, (d) DO profiles with 0.1M NaCl, (e) ORP profiles without NaCl, and (f) pH profiles with 0.1M NaCl. 0 μm represents the point at which the sensor signal was obtained by contact with the oil. The interface between oil and emulsion was changed over time within the grey area in each profile. 67

Figure 5- 1. Concept for photocatalytic degradation of MC-LR and TEM characterizations of MoS_2 films with vertically-aligned layers. (a) Schematic illustration for photocatalytic degradation using MoS_2 films. (b) Image of an as-grown MoS_2 film. (c) HRTEM image to show vertically-aligned 2D MoS_2 layers. (d) ADF-STEM image and atomic structure comparison of vertically-aligned 2D layers. (e) HRTEM image to show the uniform distribution of Pt nanoparticles on the vertically-aligned 2D layer edges. (f) Close-up image to show that vertical 2D layer edges are well maintained even after Pt incorporation. 83

Figure 5- 2. Structural and chemical characterizations by Raman, PL, and XPS. (a) Raman spectra obtained from the MoS₂ films grown with Mo seed layers of various thicknesses. (b) A1g/E1 2g intensity ratio and frequency difference of A1g–E1 2g as a function of Mo thickness. (c) PL spectra obtained from the corresponding MoS₂ films. XPS spectra of a MoS₂ film for (d) Mo3d and (e) S2p core levels. 85

Figure 5- 3. Band structure determination by optical and electrical characterizations. (a) UV-vis spectrum from a MoS₂ film with thickness of 20 nm. The inset shows the extraction of band gap (E_g). (b) UPS measurement for the determination of VB position in the MoS₂ film. (c) Surface potentials of MoS₂ and reference Au measured by scanning kelvin probe microscopy. (d) Band structure of the MoS₂ film with respect to the redox potentials for hydrogen- or oxygen evolution reactions. (e) Current-voltage characteristics of a MoS₂ film on a SiO₂/Si substrate. Inset shows the optical image of the corresponding device. 88

Figure 5- 4. *In situ* monitoring of ROS production. (a) H₂O₂ and dissolved oxygen (DO) microsensors for *in situ* characterizations of H₂O₂ production and O₂ consumption (b) Image of H₂O₂ and DO microsensors immersed in a water bath (c) ROS production from MoS₂ films of various types measured by absorbance of XTT-formazan at 470 nm (optical density [OD]₄₇₀). (d) DO concentration microprofiles of various MoS₂ films (e) H₂O₂ and DO concentration microprofiles at the surface of Pt-coated MoS₂ film. 0 μm represents the top surface of the film. All the microprofiles were obtained after ~30 min exposure to water..... 90

Figure 5- 5. Photocatalytic degradation of MC-LR at pH 5.8. (a) Removal of MC-LR as a function of illumination time (initial MC-LR concentration of 250 μg L⁻¹). (b) Comparison of adsorption with various samples after two hour illumination. (c) Comparison of MC-LR removal for Pt + MoS₂ and Au/Pd + MoS₂ at concentrations of 250 μg L⁻¹ and

500 $\mu\text{g L}^{-1}$. (d) Determination of rate constants for the photocatalytic degradation of MC-LR with Pt + MoS₂ and Au/Pd + MoS₂ based on the pseudo first-order kinetics. (e) XPS characterizations to show the appearance of N1s peaks in MC-LR tested samples (sample 1 and 2) in comparison to pristine samples (sample 3 and 4). Sample 1,3 and 2,4 were prepared from Mo films of 10 nm and 15 nm thickness, respectively..... 92

Figure 6- 2. Diagram and photograph of SC- μ -ISE 1 (left) and SC- μ -ISE 2 (right)..... 103

Figure 6- 3. Schematic diagram of microprofiling set-up for flux determination of zinc foliar/root uptake..... 106

Figure 6- 4. Zn²⁺ calibration curves obtained with (A) SC- μ -ISE 1 and (B) SC- μ -ISE 2. (Inset: recorded potential time traces of respective SC- μ -ISEs). All measurements were done in triplicates..... 108

Figure 6- 5. pH stability study of Zn²⁺ SC- μ -ISE 1. Measurements were conducted in triplicates. 108

Figure 6- 6. Microprofiles of various Zn²⁺ bulk concentrations using SC- μ -ISE 2 on A) leaves and B) roots of sour orange seedlings. (On Figure 3A, black squares indicate 0 mM, red circles 0.20 mM, blue triangles 1.3 mM, pink triangles 6.0 mM, and green rhombus 15.2 mM Zn²⁺. On Figure 3B, black squares indicate 6.3 mM and red circles 13.0 mM Zn²⁺)..... 110

Figure 6- 7. Zn²⁺ flux as a function of bulk concentration in leaves and roots of sour orange citrus seedlings..... 111

Figure 7- 1. A concept diagram of the two-step SWASV determination of Zn²⁺ in the vascular bundle of citrus plants..... 122

Figure 7- 2. SWASV responses of the developed Bi microelectrode (tip size: 6 μm in diameter) to various Zn²⁺ concentrations (1–200 ppm) between (a) a conventional method: deposition

(stirred) and stripping (unstirred) in pH 4.5 acetate buffer and (b) a two-step SWASV method: deposition (unstirred) in $ZnCl_2$ solution and stripping (unstirred) in pH 4.5 acetate buffer at 23°C. Insets: Calibration curves from 1-100 ppm Zn^{2+} 124

Figure 7- 3. pH effect on SWASV responses to Zn^{2+} concentrations during pre-concentration (inset: SWASV voltammogram of the Bi microelectrode with various pre-concentration pH values). 126

Figure 7- 4. Mass transfer effect on Zn^{2+} detection: Zn^{2+} SWASV calibration curves of various tip sizes of Bi microelectrodes under (a) stirred and (b) unstirred conditions during a deposition step. Insets: Expanded view of sensor response from 0 to 50 ppm Zn^{2+} 127

Figure 7- 5. In situ application of the developed microelectrodes for plants. (a) Pre- and post-calibration curves of combined bismuth/Pt reference microelectrode using a two-step SWASV method. (b) In situ detection of Zn^{2+} in untreated (DI water) and treated (1 mM $ZnCl_2$) citrus leaves using the double barrel Bi/Pt microelectrode..... 130

LIST OF TABLES

Table 3- 1. Distribution of bacterial 16S rRNA and 16S rDNA.....	38
Table 6- 1. Observed experimental selectivity coefficients for Zn ²⁺ cocktail with corresponding slopes for interfering ions based on the unbiased separate solutions methods	109
Table 6- 2. Estimated flux of Zn ²⁺ into leaves of roots of sour orange seedlings using the developed SC-μ-ISE 2	112
Table 7- 1. The effect of tip size on the mass transport interference of SWASV response to Zn ²⁺ using the developed Bi microelectrode.....	128

CHAPTER ONE: INTRODUCTION

The adaption of needle-type electrochemical microsensors to environmental systems has transformed how we study biofilms, mats, and sediments. With such small tip diameters (6-20 μm), they can be used to perform measurements at the microscale which can provide mechanistic information that cannot be obtained from bulk-scale measurements. Microsensors have the advantage of providing *in situ* measurements of analyte across an interface or within a biofilm without destroying the sample. They also provide a faster response time compared to macrosensors and have low sensitivity to stirring which minimizes artifacts due to turbulence.

Microsensors are used to develop microprofiles by measuring an analyte vertically through an interface and logging the data at defined points in space. From the measured concentration profiles, important kinetic parameters at a given location can be determined. These include net specific consumption and production rates (k), constituent flux (J), diffusion coefficient (D), analyte biofilm penetration and concentration variability (Figure 1-1).

Electrochemical needle-type microsensors, microelectrodes, use well-known electrochemical concepts to measure an electrochemical signal in the form of either a potential difference (mV vs. Ag/AgCl) or current (pA). Those that measure potential difference are called potentiometric microelectrodes and those that measure current under controlled potential are amperometric microelectrodes. Potentiometric microelectrodes typically use an ion-selective membrane to create a potential difference between the working and reference electrodes that corresponds to analytic concentrations. Examples of ion-selective microelectrodes include, pH, ammonia, chloride, sodium, fluoride and nitrate. Ion selective microelectrodes that rely on liquid ion exchange membranes have short lifetimes and are not typically commercially available. For ion-selective microelectrodes the chemical potential of the ion activity within the sensor is

constant and the Nernst equation can be used to describe the response of the sensor. Another potentiometric microelectrode is the phosphate sensor which does not rely on an ion-selective membrane but instead uses a corrosion mechanism where cobalt oxides is converted to cobalt phosphate in the presence of phosphate. Amperometric microelectrodes measure analyte by measuring current. A current is produced by polarizing the tip of the sensor to a specific potential which corresponds to an oxidation/reduction reaction of the analyte. Examples of amperometric microelectrodes include oxygen, hydrogen, and hydrogen peroxide.

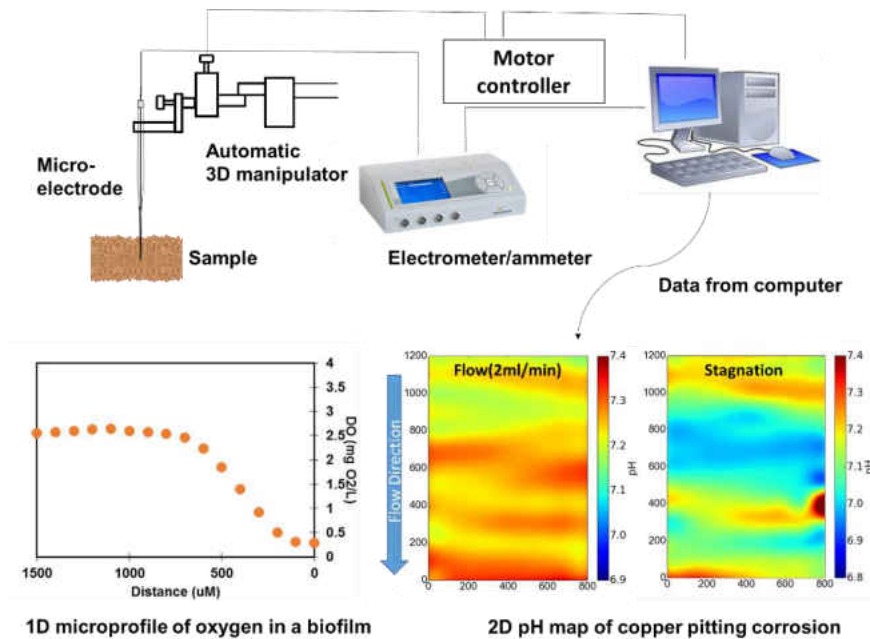


Figure 1- 1. Typical experimental setup for microprofiling and examples of microprofiling and surface mapping data

Traditionally, microsensors applications have been limited to understanding mass transport dynamics and kinetics in biofilms; however, their potential applications surpass conventional biofilm processes. Mass transport chemistry is also fundamental to biological nutrient uptake, oily wastewater treatment, photocatalytic disinfection, and plant disease management; yet, microsensors studies in these areas of research have not been explored.

Goals and objectives

The main objective of this research was to develop novel microsensors for quantifying mass transport kinetics in engineered and natural water systems. Chemical microprofiles measured in this research include, pH, dissolved oxygen (DO), oxidation-reduction potential (ORP), free chlorine, monochloramine, hydrogen peroxide (H₂O₂), and zinc. This dissertation focuses on four applications of microsensors to understand environmental engineering problems. 1) investigating the feasibility of algal biofilms for localized photo-aeration in advance wastewater treatment, 2) evaluating the performance of microelectrodes across an oil-water interface for characterizing emulsion stability in bilge water, 3) evaluating photocatalytic reactions using microelectrodes for water disinfection and emerging contaminants removal (i.e. microcystins-LR) and 4) developing zinc microsensors for monitoring the transport of zinc in citrus trees.

Dissertation Organization

This dissertation is organized in eight chapters. Chapter 1 presents introductory information and overview of this research. Chapter 2 provides a literature review and discussion of the principles of mass transport processes and determination of mass transport kinetics using microsensors.

Chapter 3 describes results from the application of a microsensor to a novel microalgal-bacterial wastewater treatment process. This chapter specifically discusses the kinetics and mass transport of oxygen and ammonia within microalgal biofilms; however, the role of chl. *a* to biomass ratio and algal growth rate on photooxygenation by microalgae are also discussed. Other results from this paper include nutrient removal efficiencies and bacterial community structure. The results of this study were submitted to *Bioresour. Technol.* (Impact Factor: 6.65).

Chapter 4 focuses on the use of microsensor for the characterization of bilge water emulsions. This study utilized needle-type microsensors and confocal laser scanning microscopy (CLSM) for characterizing simulated bilgewater emulsions with different type of surfactants (Triton X-100 and sodium dodecyl sulfate [SDS]) under various NaCl concentrations at micro-scale. A diffusion process was clearly visualized across the oil/water interface which appears to be related to emulsion formation kinetics and mass transfer. The results of this study was published in *Langmuir* (Impact Factor: 3.883).

Chapter 5 investigates photocatalytic reaction kinetics of a newly developed vertically-aligned MoS₂ photocatalyst by *in situ* characterization of ROS generation using microsensors. Moreover, it was demonstrated that the coating of thin noble metal layers on top of pristine MoS₂ films significantly improves the photocatalytic efficiency of ROS production. The underlying mechanisms for the observed photocatalytic reactions as well as their governing parameters are also discussed. This work was published in *Scientific Reports* (Impact Factor: 4.259).

Chapter 6 and 7 discusses the use of microsensors in monitoring and quantifying the movement of Zn²⁺ in citrus plants for optimized HLB management. Chapter 6 looks at developing and characterizing a solid contact micro-ion-selective electrode (SC- μ -ISE) for the determination of zinc transport in sour orange seedlings using a non-invasive microelectrode ion flux estimation (MIFE) technique. This work was published in *Electroanalysis* (Impact Factor: 2.851). Chapter 7 presents *in situ* detection of Zn²⁺ using a novel two-step square wave anodic stripping voltammetry (SWASV)-based needle-type microsensor for citrus plant applications. This work was published in MRS communications (Impact Factor: 3.01).

Chapter 8 contains conclusions and recommendations developed from this research and the appendices provide detailed methodology and supplemental information.

CHAPTER TWO: MASS TRANSPORT IN ENVIRONMENTAL ENGINEERING: A LITERATURE REVIEW

Introduction

Over the last several decades, development and production of environmental pollutants in the United States has grown exponentially (Robinson 2009). Therefore, responsible disposal practices are needed to ensure public health and environmental protection. Environmental engineers (EnvE) are needed to design systems to treat water and remove toxic chemicals (Cooper 2015). This requires an understanding of equilibrium thermodynamics, chemical reaction kinetics and mass transfer in engineered and natural systems to predict the fate of these contaminants (Logan 2012). Among these, the idea of mass flux is one of the most useful tools of chemical process modeling because of the interest in mass transport into or out of certain regions. Thus, many publications have been dedicated to the development of mass transport model equations (He et al. 2000, Yang et al. 2007, You and Liu 2002). Therefore, it is important to understand and apply these models to water treatment design.

Despite a working knowledge of mass transport models, environmental engineers are often left with little control over system conditions for transport calculations. The natural variability of environmental processes often leads to poor reliability between modeled and actual mass transport processes. Therefore, *in situ* determination of mass transport kinetics is extremely valuable to environmental engineers (Logan 2012). Within the last decade, the adaption of needle-type electrochemical microsensors to environmental systems has transformed how we study mass transport processes (Bishop et al. 1995, de Beer and Schramm 1999, Lewandowski et al. 1995). With such small tip diameters (3-20 μm), they can be used to perform measurements at the microscale which can give important kinetic parameters at a given location. These include production rates (k), constituent flux (J), and diffusion coefficient (D). With this information,

environmental engineers can better design and optimize water treatment processes (Lee et al. 2009).

This brief review on the fundamentals of mass transport mechanisms in environmental engineering processes discusses diffusive mass transport examples in environmental engineering, including mass transport processes in abiotic and biofilm processes, and looks at methods for determining mass transport kinetics using microsensors.

Diffusive Mass Transport

Diffusion can be an important mass transport mechanism for gases, molecules, ions and small particles. Transport by molecular diffusion is relatively slow compared to other bulk transport processes (Clark 2011). For example, if a small amount of chemical is placed in a beaker of water, the chemical would slowly diffuse from the areas of high concentration to the areas of low concentration. After enough time, the chemical in the beaker would reach an equal final concentration. While this process is much slower than stirring the beaker, diffusion transporting can play a significant role in many areas of environmental engineering.

In order to understand diffusion transport equations, it is important to understand the mechanism of how chemicals are transported by molecular diffusion. Brownian motion can be defined as the motion of a single molecule driven by thermal energy (Logan 2012). Although the exact path of any one molecule cannot be predicted, we can quantify the net effect of Brownian motion of the transport of all the molecules in the system. For example, if all molecules movement is random, there is no net change in molecules that are homogenous; however, if a new chemical is introduced, the random motion of the molecules will carry them away from their initial location. This random motion of molecules away from their initial location can be

described by Fick's First Law where a change in concentration in a fluid changes with distance from the point of injection. Figure 2-1 demonstrates diffusive mass transport.

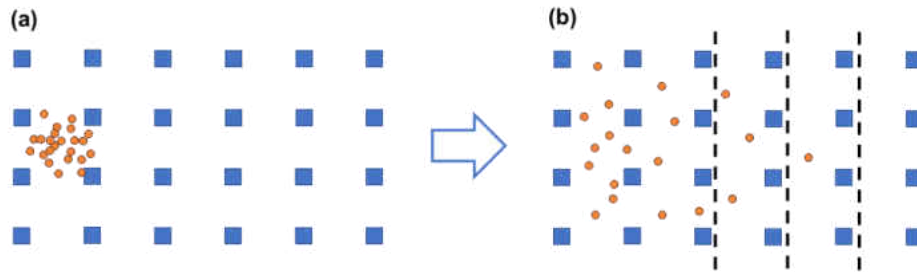


Figure 2- 1. Illustration of diffusive mass transport as a function of time where (a) is the time the chemical was injected and (b) is the chemical gradient formed by diffusion (adopted from Logan (2000)).

Looking at Figure 2-1, it is clear that the flux of a chemical at any point is proportional to the concentration gradient at that point. This can be described mathematically using Fick's First Law, or

$$j_{Cw,z} = -D_{Cw} \frac{dc_{Cw}}{dz} \quad (2-1)$$

Where $j_{Cw,z}$ is the mass flux of C through phase w in the z direction. $\frac{dc_{Cw}}{dz}$ is the gradient of C at any point Z and D_{Cw} is a known diffusion coefficient (Logan 2012). The molecular diffusion coefficient is a basic property of a chemical. It is different for every chemical and every phase and is a function of temperature. Typically, diffusion coefficient can be found in references; however, they can also be determined experimentally (Revsbech et al. 1998) or using correlations. For example, diffusion coefficients are closely related to the molecular weight of the molecule. The Wilke-Chang correlation is commonly used for predicting the diffusivity of small compounds in aqueous solution.

$$D_{cl} = \frac{7.4 \times 10^{-8} T (\Phi_l M_t)^{1/2}}{\mu_l V_{C,b}^{0.6}} \quad (2-2)$$

Where, D_{cl} is the diffusivity of the chemical in $\text{cm}^2 \text{s}^{-1}$, μ_l is the viscosity of the solvent, T is the absolute temperature in K, M is the molecular weight of the liquid, V_C is the molal volume of the chemical at the normal boiling point in $\text{cm}^3 \text{g mol}^{-1}$, and Φ_l is the association parameter for the liquid phase (Wilke and Chang 1955).

Fick's law and other special diffusive transport equations are used to describe the transport of molecules due to its thermal energy (Clark 2011). Dispersion is when a chemical is transported due to bulk or turbulent motion and should not be confused with diffusive transport. While both transport mechanisms play an important role in reactor design, diffusive transport is the dominant transport mechanism for the processes discussed in this dissertation (e.g., biofilm, emulsion, and photocatalytic kinetics).

Diffusive Transport Processes in Environmental Engineering

Mass transport modeling is an essential tool for environmental engineers. Applications include determining adsorption kinetics, concentration polarization in membrane processes, advance oxidation kinetics, and biological processes like determining substrate utilization kinetics of biofilms. In abiotic processes, transport can usually be simplified into three theories of mass transport; 1) stagnate film theory where mass transport is through a layer assumed to be stagnant, 2) penetration theory where chemical is gas phase penetrate into a falling liquid film and boundary layer theory where transport to a flat surface is assumed to be a uniform flow field (Clark 2011, Logan 2012). Biological mass transport can be more complex. Biofilms can increase and decrease in thickness. They can be heterogenous by nature and can die off at the bottom of the biofilm due to lack of nutrients (Lewandowski and Beyenal 2013). Below, mass transport in abiotic and biotic systems are briefly discussed.

Abiotic mass transport processes

Diffusive transport is typically used to describe mass transport from a bulk liquid to a solid uniform surface. This is because mass transport for dispersive mechanisms decrease as liquid velocity decrease. Approaching the surface of a liquid solid interface, liquid velocity decreases to a point where it is almost stagnant and diffusive transport mechanisms are dominant. This layer is called the diffusion boundary layer. Below this layer, Fick's first law can be used to describe mass transport.

While Fick's first law is commonly used for mass transport kinetics, the model is often over simplified which has given rise to many mass transport models that are specific to certain applications (Clark 2011). For example, in membrane processes it can be assumed that there is no net mass transfer of the diffusing species at steady state. In this case there is a flow toward the membrane, therefore there is a convective flux toward the membrane surface. Since the concentration of analyte is going to be higher at the membrane surface, there is also a diffusive transport away from the membrane. Therefore, the following equation can be used.

$$\ln\left(\frac{C_g}{C_b}\right) = (u - z) \frac{\delta}{D_{AB}} \quad (2-3)$$

where δ is the thickness of the particle layer above the membrane, C_g is the particle concentration at the surface of the membrane and C_b is the concentration in the bulk. The term $(u - z)$ is the mass-average velocity or membrane-permeate flow velocity (Clark 2011). The equation above demonstrates how mass transport model can be developed; however, this model may be over simplified and others have developed more accurate models that include the increasing concentration of particles as the fluid is passing through the membrane and diffusivity through the support layer of the membrane.

Biotic mass transport processes

A significant portion of mass transport modeling in environmental engineering is focused on the kinetics of biofilms (Lazarova and Manem 1995, Rittman and McCarty 1981, Wuertz et al. 2003). Depending on the bulk substrate concentration and the biofilm thickness, it can be possible to determine system order kinetics which is very useful for biological reactor design. In a simplified biofilm model, there are two boundary layers above the biofilm surface: the mass transport boundary layer and the hydrodynamic boundary layer. Within the respective boundary layers gradients are formed with flow velocity and nutrient concentration decreasing towards the biofilm surface (Lewandowski and Beyenal 2013). This is illustrated in Figure 2-2.

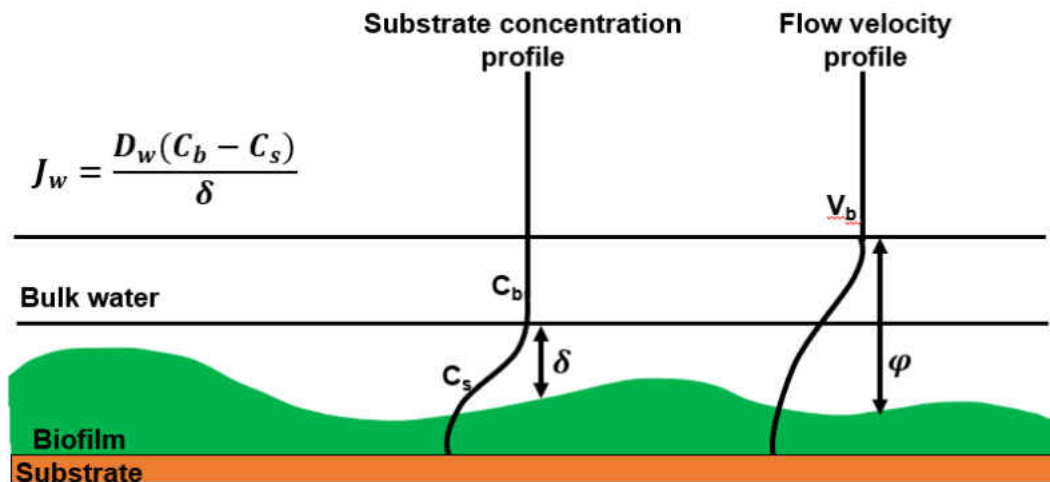


Figure 2- 2. Substrate concentration profile and flow velocity distribution near and within a biofilm. (From Lewandowski and Beyenal (2013)).

As flow velocity decreases approaching the biofilm surface, the mechanism of chemical transport changes from dispersive or convection to diffusion transport. Since microorganism metabolize nutrients faster than it is delivered by diffusion, a concentration profile within the hydrodynamic boundary is formed. The layer above the biofilm where the nutrient concentration decreases as a result of diffusion is called the mass transport boundary layer. Below the biofilm

surface different factors affect mass transport, for example, the density and porosity of the biofilm; therefore, the chemical profile above and below the surface of the biofilm need to be combined to get a representative picture of the overall mass transport. Therefore, chemical component distribution above and within a biofilm need to be measured to determine overall mass transport.

The substrate concentration profile external to the biofilm surface is the flux (J) of the substrate to the biofilm which is described in the following equation

$$J_w = \frac{D_w(C_b - C_s)}{\delta} \quad (2-4)$$

Where $C_b - C_s$ the difference between the substrate concentration in the bulk solution and at biofilm surface, (Dw) is the diffusion coefficient in water and (δ) is the thickness of the mass transfer boundary layer(Lewandowski and Beyenal 2013). Once inside the biofilm the substrate is transported by diffusion and consumption by the biofilms according the Monod-type kinetics (Lazarova and Manem 1995). At steady state the rate of substrate delivery by diffusion equals the rate of microbial substrate utilization therefore the following equation can be used.

$$D_f \frac{d^2 C}{dz^2} = \mu_{max} \frac{C}{K_{sM} + C} \frac{X_f}{Y_{s/s}} \quad (2-5)$$

Where D_f is the average effective diffusivity of the growth-limiting nutrient in the biofilm (m^2/s), z is the distance from the bottom (m), L_f is the thickness of the biofilm (m), X_f is the average biofilm density (kg/m^3), $Y_{x/s}$ is the yield coefficient (kg microorganisms/kg nutrient), μ_{max} is the maximum specific growth rate (s^{-1}), K_{sM} is the Monod half-rate constant (kg/m^3), C is the growth-limiting substrate concentration (kg/m^3), and C_s is the growth limiting substrate concentration at the biofilm surface (kg/m^3)(Lewandowski and Beyenal 2013).

Determination of Mass Transport Kinetics

Traditional mass flux measurement is done sampling bulk water; however, this is not preferred because slow mass transport processes may not be detected. Therefore, direct measurement of the concentration between the bulk water and the surface is needed for accurate determination of mass transport kinetics. The development of needle type microsensors has enabled researchers to measure mass transport directly due to its small tip size of only a few microns. This allows for measurements approaching a mass transport interface and though the interface without disturbing the sample.

To measure a chemical profile, a microsensor is attached to a computer-controlled micromanipulator to move the tip of the sensor through the mass transport interface. The computer software moves and records position according to user set parameters. Measurements typically begin 1000-3000 μm above the substrate and readings are taken every 10 to 100 μm . Depending on the microelectrode type, a multimeter is used to monitor potential or current from the microsensor. The multimeter must be sensitive enough to detect picoammeter changes due to small tip size of the sensor. Microsensors are very fragile therefore, they need to be calibrated before and after each experiment to ensure they were not damaged. A guide sensor can be used to help the user avoid damaging the sensor on a hard substrate.

The sample is placed in a flow cell with a constant flow of liquid over the sample (e.g. 2 ml/min) to develop conditions constant with boundary layer theory. A microscope can be used to track the position of the microsensor and a lab stand can position the sample within view of the microscope. The experiment should be performed in a Faraday cage to avoid electrostatic interferences. Figure 2-3(a) shows an experimental set up for a typical micro profiling experiment.

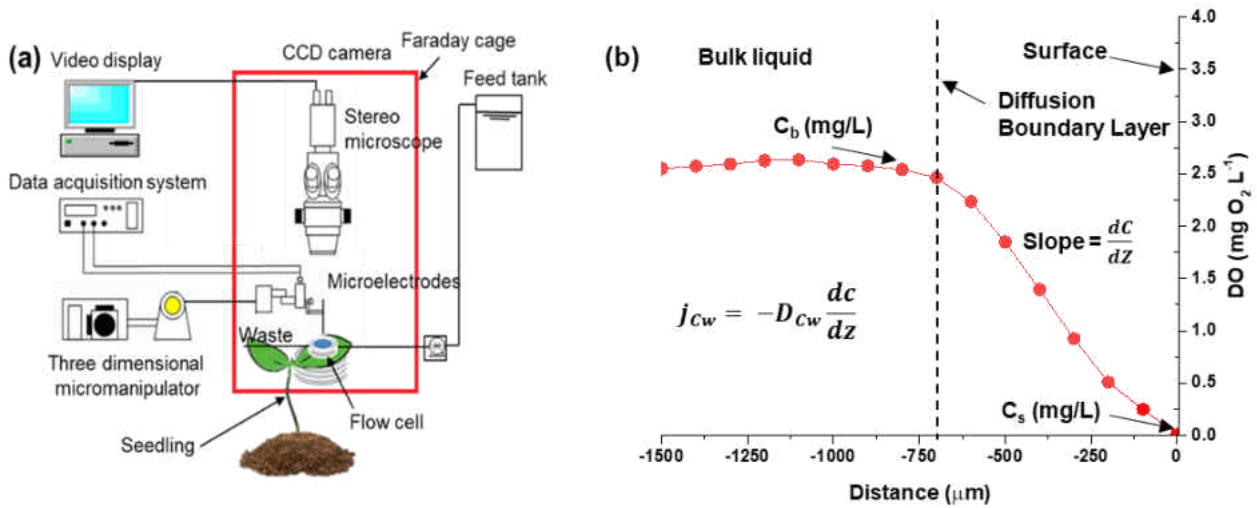


Figure 2- 3. a) Diagram of a typical microprofiling experimental set up and b) typical microprofile

Figure 2-3(b) displays a typical microprofile where dissolved oxygen is measured from 1500 μm to 0 μm above a reactive surface. Bulk concentration (C_b) is calculated from the average reading above the diffusion boundary layer and surface concentration (C_s) is found at the surface of the substrate. The slope is calculated by subtracting the concentration from the bulk to the surface and dividing by the distance between the diffusion boundary layer. This can be multiplied by a known diffusion coefficient to calculate flux.

The effective diffusion coefficient biofilms and sediments can also be determined using microprofiles (Revsbech 1989). Apparent diffusion coefficient is an essential parameter for calculating diffusive mass transport. Under non-steady state concentrations chemical profiles are described by Fisk's second law of diffusion

$$\frac{dC}{dt} = D_s \frac{d^2C}{dx^2} + (P - R) \quad (2-6)$$

Where P and R are the rates of production or consumption at depth x to time t .

Microchemical profiles taken over time can be used to determine D_s if there is no biological production or consumption of the substrate (Revsbech 1989). Therefore, the sediment needs to be disinfected before micro profiling. It is also important to conduct diffusion coefficient experiments at a well-defined temperature because even a small temperature can result in a significant difference in D_s . A study by Revsbech (1988) discusses the methods for determination diffusion coefficients using microsensors in more detail.

References

- Bishop, P.L., Zhang, T.C. and Fu, Y.-C. (1995) Effects of biofilm structure, microbial distributions and mass transport on biodegradation processes. *Water Science and Technology* 31(1), 143-152.
- Clark, M.M. (2011) *Transport modeling for environmental engineers and scientists*, John Wiley & Sons.
- Cooper, C.D. (2015) *Introduction to environmental engineering*, Long Grove, IL : Waveland Press, [2014].
- de Beer, D. and Schramm, A. (1999) Micro-environments and mass transfer phenomena in biofilms studied with microsensors. *Water Science and Technology* 39(7), 173-178.
- De Beer, D., Stoodley, P., Roe, F. and Lewandowski, Z. (1994) Effects of biofilm structures on oxygen distribution and mass transport. *Biotechnology and bioengineering* 43(11), 1131-1138.
- He, W., Yi, J.S. and Van Nguyen, T. (2000) Two-phase flow model of the cathode of PEM fuel cells using interdigitated flow fields. *AIChE Journal* 46(10), 2053-2064.
- Lazarova, V. and Manem, J. (1995) Biofilm characterization and activity analysis in water and wastewater treatment. *Water research* 29(10), 2227-2245.
- Lee, W.H., Seo, Y. and Bishop, P.L. (2009) Characteristics of a cobalt-based phosphate microelectrode for in situ monitoring of phosphate and its biological application. *Sensors and Actuators B: Chemical* 137(1), 121-128.
- Lewandowski, Z. and Beyenal, H. (2013) *Fundamentals of biofilm research*, CRC press.
- Lewandowski, Z., Stoodley, P. and Altobelli, S. (1995) Experimental and conceptual studies on mass transport in biofilms. *Water Science and Technology* 31(1), 153-162.
- Logan, B.E. (2012) *Environmental transport processes*, John Wiley & Sons.
- Revsbech, N.P. (1989) Diffusion characteristics of microbial communities determined by use of oxygen microsensors. *Journal of Microbiological Methods* 9(2), 111-122.
- Revsbech, N.P., Nielsen, L.P. and Ramsing, N.B. (1998) A novel microsensor for determination of apparent diffusivity in sediments. *Limnology and Oceanography* 43(5), 986-992.
- Rittman, B. and McCarty, P.L. (1981) Substrate flux into biofilms of any thickness. *Journal of the Environmental Engineering Division* 107(4), 831-849.
- Robinson, B.H. (2009) E-waste: an assessment of global production and environmental impacts. *Science of the total environment* 408(2), 183-191.

Wilke, C. and Chang, P. (1955) Correlation of diffusion coefficients in dilute solutions. *AIChE Journal* 1(2), 264-270.

Wuertz, S., Bishop, P.L. and Wilderer, P.A. (2003) *Biofilms in wastewater treatment*, IWA Publishing.

Yang, W., Zhao, T. and Xu, C. (2007) Three-dimensional two-phase mass transport model for direct methanol fuel cells. *Electrochimica Acta* 53(2), 853-862.

You, L. and Liu, H. (2002) A two-phase flow and transport model for the cathode of PEM fuel cells. *International Journal of Heat and Mass Transfer* 45(11), 2277-2287.

CHAPTER THREE: APPLICATION OF MICROSENSORS TO ALGAL-BACTERIAL BIOFILMS FOR ADVANCED WASTEWATER TREATMENT

Abstract

The removal of nitrogen (N) and phosphorus (P) from synthetic wastewater was investigated in a novel microalgae integrated fixed film activated sludge (MAIFAS) sequencing batch reactor (SBR) to better understand microalgal/bacterial biofilms in wastewater treatment. The MAIFAS system removed >99% ammonia and 51% P without the need for mechanical aeration, a marked improvement over the suspended microalgae sludge control, which only removed 57% ammonia and 49% P from synthetic wastewater. A microscopic investigation using microelectrodes showed well-defined photo-oxygenation by the MAIFAS biofilms with surface DO concentrations reaching 6.7 mg O₂/L compared to 1.2 mg O₂/L in the bulk solution. This localized oxygenation appears to contribute to increased ammonia removal within the biofilm. Ammonia microprofiles revealed no significant ammonia removal in the algal portion of the biofilm indicating the role of algae biofilm in the MAIFAS reactor is mostly aiding photo-oxygenation. Genetic sequencing revealed that the addition of microalgae to the IFAS system promoted significant changes in the bacterial community structure and altered metabolic activity of several bacterial groups. In particular, the MAIFAS biofilms showed a large population of *Candidatus Accumulibacter* compared to the IFAS control (55% vs. <1%). Overall, this research represents a novel strategy for reducing energy consumption while meeting stringent effluent standards using a hybrid symbiotic microalgae-based IFAS technology.

Introduction

As the human population increases and environmental requirements become more stringent, the need for sustainable water treatment that meet regulatory standards and reduce energy consumption has become a top priority in the water industry (EPA, 2006). To address these issues, microalgal treatment systems have been studied as a low-cost, environmentally friendly, wastewater treatment alternative to conventional wastewater treatment processes. Algae's nutritional and chemical requirements offer opportunities for advanced bioremediation and biofuel production by integrating industrial and municipal utilities with algal systems for a holistic approach to managing urban resources. For example, microalgae (such as *Chlorella vulgaris*) have been used to treat wastewater because of their nutrient (nitrogen [N] and phosphorous [P]) uptake potential without having to rely on an organic carbon source (González et al. 2008, Boelee et al. 2011). In addition, microalgae have drawn attention as a renewable energy source because of their potential for high biomass and lipid productivity (15–300 times more than conventional crops-to-biodiesel production) (Church et al. 2017, Hwang et al. 2016, Pate et al. 2011).

In recent years, several studies have coupled algal photosynthesis with conventional biological nutrient removal processes. In these systems, algal photosynthesis is used to dramatically decrease energy consumption by reducing energy costs associated with mechanical aeration (i.e., 45–75% of plant energy costs (Rosso et al., 2008)) (González et al., 2008; Karya et al., 2013). For example, Karya et al. (2013) achieved full ammonia removal from wastewater (50 mg NH₄⁺-N L⁻¹) without mechanical aeration and found that 85% of the removal was due to nitrification. Likewise, Wang et al. (2015) used a microalgal-bacterial consortium to remove more than 90% total nitrogen (TN) from digested swine manure (300 mg NH₄⁺-N L⁻¹) and

contributed to 80% of removal to nitrification/denitrification. However, these systems rely on fast growing microalgae to supply oxygen and slow growing nitrifying bacteria for nitrification/denitrification; thereby limiting solid retention times (SRTs) that can be used to support both organisms. Ideally, the SRT for algae and nitrifying bacteria should be uncoupled to improve nutrient removal efficiencies.

Over the past two decades, many wastewater treatment plants in the United States (U.S.) have found that fixed film technologies (i.e., moving bed bioreactors [MBBR] and integrated fixed film activated sludge [IFAS]) provide an effective alternative for expanding or improving existing wastewater treatment facilities, with respect to nitrification, due to its relatively small footprint (Onnis-Hayden et al., 2011). This is because the nitrifying bacteria tend to establish themselves on biofilm carriers and thus can be retained even when suspended nitrifiers would be washed out of the system (e.g., at low temperatures or short solids retention time [SRT]). While both MBBR and IFAS systems are suitable for biological N removal through nitrification, IFAS systems can be optimized for both biological N and P removal because the SRT for nitrifiers and polyphosphate-accumulating organisms (PAOs) are uncoupled. Previous research has demonstrated that nitrifiers colonized IFAS media while PAOs existed mainly in suspension (Kim et al., 2010; Sriwiriyarat and Randall, 2005 Onnis-Hayden et al., 2011). By applying this concept to an algal-bacterial wastewater process, it is hypothesized that algal biofilm can be formed on the IFAS media and provide oxygen sufficiently to nitrifying biofilm, while maintaining a SRT suitable for P removal by suspended algal-bacterial consortium.

This study presents a novel symbiotic microalgae-based IFAS (MAIFAS) technology as a strategy for reducing energy consumption while meeting stringent effluent standards. The overall goal of this research was to determine whether the developed MAIFAS process can improve on

existing IFAS process by uncoupling photo-aeration between suspended solids for P removal and biofilms for nitrification. To do this, three lab-scale sequencing batch reactors (SBRs) (i.e., MAIFAS, IFAS [control], suspended microalgae [negative control]) were operated and evaluated for 150 days for nutrient removal and photo-aeration. Interactions between microalgae and bacteria as well as mechanisms of N and P removal in the MAIFAS system were elucidated using multiscale investigations which include microelectrodes, next-generation molecular methods, and a series of batch studies.

Materials and Methods

Microalgae cultivation, bacteria inoculation, and synthetic wastewater preparation

Chlorella vulgaris (UTEX 2714, UTEX Algae Culture Collection, Austin, TX) is commonly used to study microalgal wastewater treatment (De-Bashan et al., 2002; Wang et al., 2010) and thus was selected as a model microalga in this study. The *C. vulgaris* strain was grown in 1L glass bottles (13951L, Corning Inc., Corning, NY) containing 500 mL of Bold's basal medium (BBM). The bottles were incubated at room temperature (23°C) under continuous cool-white fluorescent light illumination of 20 $\mu\text{mol m}^{-2} \text{S}^{-1}$ photosynthetically active radiation (PAR) (Apollo Horticulture T5, 6400K Fluorescent bulbs) and stirred at 50 rpm. Initially, the culture was aerated using an aquarium air pump to supply CO₂ to the algae. After reaching stationary phase, the culture was used to inoculate SBR experiments. The activated sludge was collected from the return activated sludge of a local wastewater treatment plant (Iron Bridge, Orlando, FL) for seeding the SBRs. Synthetic wastewater with the following composition was used as a growth media: 240 mg L⁻¹ sodium acetate, 57.5 mg L⁻¹ NH₄Cl, 51 mg L⁻¹ K₂HPO₄, 83 mg L⁻¹ MgSO₄, 13 mg L⁻¹ CaCl₂, 65 mg L⁻¹ yeast extract and 65 mg L⁻¹ beef extract equivalent in total

to 300 mg L⁻¹ chemical oxygen demand (COD), 30 mg TN L⁻¹ and 10 mg P L⁻¹ (Jabari et al., 2014). 500 mg L⁻¹ NaHCO₃ was also added to provide sufficient alkalinity for nitrification.

Photo-SBR

Three lab-scale SBRs (4L) were constructed with plexiglass and operated in the sequence of fill, mix, aerate, idle, settle, and decant phases using a programmable logic controller (PLC) (Chronrol, San Diego, CA) (Fig. 3-1 and Fig. B1). The reactors were operated at room temperature (22-24 °C) and in 12 h cycles consisting of feeding (10 min), anaerobic step (80 min), aerobic step (300 min), anoxic step (150 min), aerobic step (60 min), settling (90 min) and decanting (30 min). 40% of the bulk working volume was filled with AnoxKaldnes (K1) biofilm carriers (Veolia, Lund, Sweden) (specific surface area of 500 m²/m³) in two IFAS SBRs (MAIFAS and IFAS control). The third reactor with no media was used as a negative control. The reactors were operated with 12 h hydraulic residence time (HRT) and 30 d SRT_{suspended} (wasting during the aerobic phase). The pH was not controlled and ranged from 7.4 to 8.1 during the 12 h SBR cycle. All three SBRs were mixed during the anaerobic, aerobic and anoxic phases using an overhead stirrer.

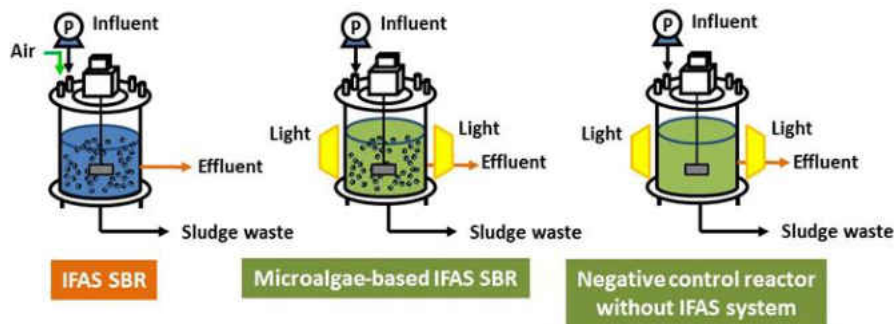


Figure 3- 1. Schematic diagram of microalgae-based IFAS (MAIFAS) SBR and two controls (IFAS SBR and algae SBR without IFAS media).

Before experiments, the two IFAS reactors were first inoculated with activated sludge for 60 days using the synthetic wastewater to develop a nitrifying biofilm on the K1 media. During this time, all three reactors showed 71 to >99% ammonia removal, 66 to 97% COD removal and >99% TP removal. After biofilm formation on the K1 media was observed, Phase I began with the addition of 500 mg L⁻¹ *C. vulgaris* to the MAIFAS and suspended control SBRs. The SBRs seeded with algae were exposed to fluorescent light (76.2 μmol m⁻² S⁻¹ PAR) during aerobic phases. Air was supplied to all reactors during Phase I to develop the nitrifiers. A Chlorophyll *a* (Chl. *a*) to biomass ratio above 10.25 mg g⁻¹ was designed to provide enough oxygen by green algae to the system for nitrification to occur (Karya et al., 2013); however, even after 75 days (Phase I), the Chl. *a* to biomass ratio was still under 6 mg g⁻¹ and thus the wastewater composition was adjusted to promote microalgal growth (Phase II). Ammonia and P concentrations were increased to 70 mg N L⁻¹ and 20 mg P L⁻¹, respectively, while COD was decreased to 150 mg L⁻¹. During Phase II, air supply to the algae reactors was turned off to evaluate the capability of microalgal photo-oxygenation. The SBRs were operated under Phase II conditions for 75 days.

Analytical methods

Samples (50 mL) were taken from the effluent during the withdrawal stage twice a week for water quality analysis. The samples were filtered using 45 μm glass fiber filters (934-AH, Whatman) and analyzed for pH, ammonia, total phosphorus (TP), and chemical oxygen demand (COD). pH and ammonia were measured using pH and ammonia probes (Intellical™ pH Electrode PHC20; IntelliCAL™ ammonia probe, ISENH318101, Hach, Loveland, Colorado). TP was measured using Hach Method 8180 (ascorbic acid method test) and COD was measured using Hach Method 8000. Duplicate samples were processed during each sampling point.

Additionally, hourly samples were taken through a 12hr SBR cycle and analyzed for nitrate, nitrite, and dissolved oxygen (DO). Nitrate and nitrite were measured using the cadmium reduction method (Hach Methods 8039 and 8192, respectively). DO was measured using a DO probe (407510, Extech, Nashua, New Hampshire).

Suspended biomass was determined using the Standard Methods (APHA, AWWA, and WEF, 1999) for Solids (SM 2540). Chlorophyll *a*, which was used to monitor algal growth, was measured using a modified version of the SM10200 H.2.b. method (APHA, AWWA, and WEF, 1999). Briefly, a 5 mL sample was centrifuged at 13,000 rpm for 10 minutes. The supernatant was discarded and 5 mL of 96% methanol was added to the remaining pellet. This mixture was vortexed for 10 minutes and incubated at 60 °C for 15 minutes. The sample was then cooled at 4°C for 30 minutes and centrifuged at 13,000 rpm for 10 minutes. The supernatant's absorbance at 666 and 653 nm was measured using a spectrophotometer (DR900, Hach, Loveland, Colorado) to determine Chl. *a* based on equation (3-1).

$$\text{Chlorophyll } a \text{ (mg/L)} = 15.65A_{666} - 7.34A_{653} \quad (3-1)$$

Where A_{666} is the absorbance of light at 666nm and A_{653} is the absorbance of light at 653 nm.

Microprofiling

DO concentration and pH microprofiles were measured using a DO microsensor (tip diameter: 50 μ m) and pH microsensor (tip diameter: 10 μ m) (UNISENSE A/S, Denmark). Ammonia concentration microprofiles were measured using a fabricated ammonia ion selective microelectrode (tip diameter: 30 μ m) following methods described in Lewandowski (2014). The DO microsensor was calibrated in respective oxygen saturated (aeration: 8.6 mg O₂/L at 23°C) and oxygen depleted (nitrogen bubbling: 0% DO) artificial wastewater. The pH microelectrode

was calibrated in standard buffer solutions (pH 4, 7, and 10, Fisher Scientific, Hampton, NH). The ammonia microsensor was calibrated in artificial wastewater with varying ammonia chloride concentrations. Microsensors were calibrated before and after each profile.

For microprofile measurements, a K1 biofilm carrier was removed from the reactor, gently cut in half using a scalpel (Disposable Scalpel No. 10, Thermo Scientific, Waltham, MA), and placed in a customized flow cell that allowed a flow of wastewater over the biofilm at a rate of 2 mL/min (Lee et al. 2009). The sample was held in place using a clamp (VTHH, Veleman Inc., Forth Worth, TX). The positioning and movement of the microsensor tip in the sample was accomplished using a three-dimension (3D) micromanipulator (UNISENSE A/S, Denmark) and observed using a stereomicroscope with a CCD camera (World Precision Instruments, Sarasota, FL). A Ag/AgCl reference electrode (MI-401, Microelectrodes Inc.) was positioned in the flow cell using a helping hand (VTHH, Veleman Inc., Forth Worth, TX) and a lab jack (Model 110, Swiss Boy lab jack, Fisher Scientific) was used to center the biofilm within the view of the stereomicroscope. The microprofile measurements were conducted in a Faraday cage (81-334-04, Technical Manufacturing Co. Peabody, MA) to minimize electrical interference. A florescent light was used to provide $76.2 \mu\text{mol m}^{-2} \text{S}^{-1}$ of light (the same as the MAIFAS SBR operation) to the microalgae integrated fixed biofilm carrier during profiling measurements. A photo of the experimental set up is shown in Figure B2. Microprofile measurements were performed from 3,000 μm above to the surface of the K1 media to the surface at every 100 μm with 5 seconds intervals between each measurement. Two replicate profiles were taken for each parameter.

Illumina sequencing

DNA and RNA extraction, PCR and high-throughput amplicon sequencing

Total RNA and DNA were extracted from 5 MAIFAS (micro-algae seeded reactor) and 3 IFAS (control reactor) biofilm samples as previously described (Pitkänen et al. 2013) with some minor modifications. Briefly, the AllPrep DNA/RNA Mini Kit (Qiagen GmbH, Hilden, Germany) was used to extract total nucleic acid. RNA was further purified using Ambion TURBO DNA-free DNase Kit (Life Technologies, Grand Island, NY). The concentration and purity of RNA and DNA were determined using the Qubit 2.0 Fluorometer with Qubit RNA and dsDNA HS assay kits, respectively (Life Technologies, Grand Island, NY). cDNA was generated using random hexamer primed Superscript III system for RT-PCR (Life Technologies, Grand Island, NY). Samples (cDNA and DNA) were stored at -20°C until used for next generation sequencing. cDNA and DNA were used as templates to generate independent libraries targeting bacterial 16S ribosomal RNA genes (rDNA) and transcripts (rRNA). We used barcoded 16S rRNA gene targeting primers (i.e., 515F and 806R) as described in Caporaso et al. (2011) and sequenced the targeted product (i.e., 291 bp) in both directions using an Illumina MiSeq PE250 sequencing kit (Caporaso et al. 2011). Sequencing was performed at the Cincinnati Children's Hospital Medical DNA Sequencing and Genotyping Core facility.

Next generation sequencing data preprocessing and analysis

Sequence reads (16S rDNA- and 16S rRNA-based) were processed and analyzed using mothur software (Schloss et al. 2009). Sequence reads that did not fit the following criteria were discarded from further analyses. This includes reads that did not form contigs, deviated considerably from the expected PCR size product, had ambiguous bases, or had homopolymers greater than 8 bases long. Sequence reads were grouped at a 97 % similarity and the consensus

sequences were then identified using mothur and the Silva (Quast et al. 2012) database as a reference. Prior to the classification analysis, a prescreening step was performed with a randomly selected subset of all the sequences generated per sample (n=10,000) to further filter out chimeras and difficult to align sequences. Excel was used to determine the overall relative abundance of representative sequences at different taxonomic levels (e.g., class, order, family, genus). Sequences were analyzed using Blast (<http://www.ncbi.nlm.nih.gov/BLAST/>) and RDP classifier (Wang et al. 2007) to further confirm their phylogenetic affiliation and to classify sequences at a low taxonomic level (genus and species) whenever possible.

Results

Nutrient removal and biomass growth

Phase I. Mechanical aeration

During Phase I, all reactors were mechanically aerated during aerobic phases. Figure 3-2 shows influent and effluent pH, ammonia, COD and TP changes during the experiment. After the inoculation of microalgae, it took 37 days for the system to show consistent nutrient removal. Before this, the IFAS control exhibited excellent COD, ammonia, and TP removal (95%, 80%, and 89%, respectively) but reactors containing microalgae (MAIFAS and suspended) displayed poor nutrient removal (<60% for COD, ammonia, and TP). However, once the algae was acclimated, no detectable ammonia and no more than 26 mg L⁻¹ COD were found in the effluent of all three reactors. Likewise, TP removal was above 70% for all reactors for the end of Phase I with the exception of a one-week period where TP exceeded 5 mg P L⁻¹ in the effluent of the suspended reactor. The effluent pHs of the SBRs containing microalgae were found to be higher than the IFAS control, particularly in towards the end of Phase I. For example, the effluent pH of the MAIFAS and suspended reactors were approximately 8.2 for days 50-75; however, the IFAS

control and influent was about 7.6. This could be due to the algae consuming CO₂, which would increase the pH.

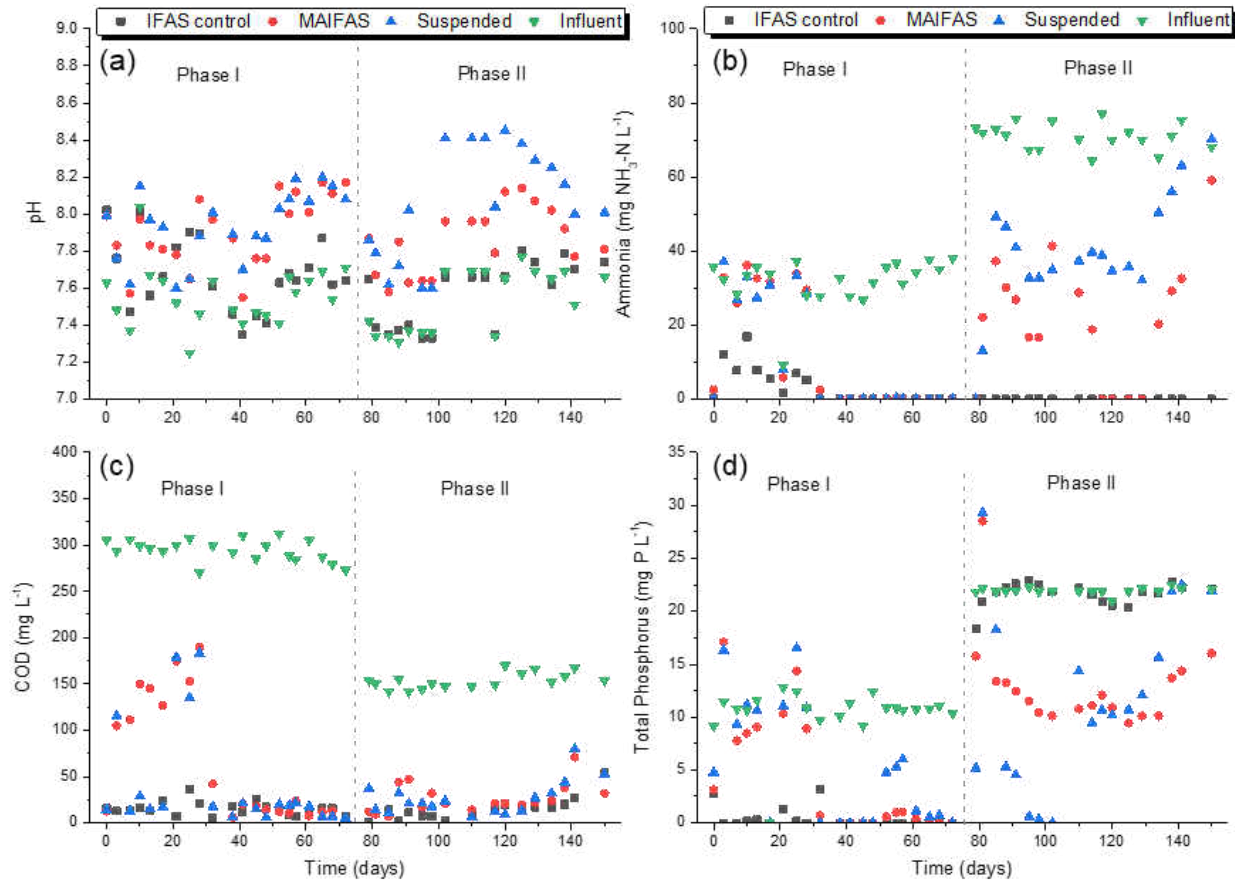


Figure 3- 2. (a) pH, (b) ammonia, (c) COD and (d) total phosphorus (TP) effluent changes in IFAS control, MAIFAS and suspended algae control SBRs over 150 days. Mechanical aeration was applied to all reactors during the aerobic sequence of Phase I. Only light was applied to MAIFAS and suspended reactors during the aerobic sequence of Phase II.

Figure 3-3 shows the characteristics of the suspended biomass in each reactor over the 150-day experiment. During Phase I, all SBRs exhibited decreasing mixed liquor suspended solids (MLSS) and mixed liquor volatile suspended solids (MLVSS) for the first 30 days after inoculation of *C. vulgaris*. The suspended SBR had a starting MLVSS of 5,250 mg L⁻¹ and decreased to 3,500 mg L⁻¹, the MAIFAS SBR had a starting MLVSS of 2,000 mg L⁻¹ and decreased to 1,000 mg L⁻¹, and the IFAS control reactor has a starting MLVSS of 2000 mg L⁻¹

and decreased to 1,800 mg L⁻¹ after the first 30 days. After this initial decrease, the MLVSS concentration was consistent for the remainder of Phase I. While all reactors displayed excellent nutrient removal throughout Phase I, the reactors were all supplied with oxygen during the aeration phases of the SBR sequence. This may have impeded the growth of microalgae. During Phase I, the growth of microalgae was limited to 5.76 mg g⁻¹ in the MAIFAS reactor and 1.76 mg g⁻¹ in the suspended reactor (Fig. 3-3(d)).

Phase II. Photo-aeration

In Phase I, it was found that microalgal growth may be hindered by competition for nutrients with the activated sludge. Therefore, in Phase II, nutrient concentrations were increased to 70 mg NH₃-N L⁻¹ ammonia and 20 mg P L⁻¹ total phosphorus (TP) in an attempt to further support microalgal growth. Furthermore, preliminary batch experiments (Fig. B3) demonstrated that growth rates slow down significantly when *C. vulgaris* opts for heterotrophic growth and results in poor photo-aeration. Therefore, influent COD was reduced to 150 mg L⁻¹ and the MAIFAS and suspended reactors were no longer mechanically aerated during Phase II.

The change in experimental conditions (i.e., increase in influent N and P concentrations, reduction of COD input, and cessation of mechanical aeration) clearly increased microalgal growth. Chl. *a* concentration increased from 3.28 to 44.95 mg L⁻¹ and 4.15 to 9.53 mg L⁻¹ in the suspended and MAIFAS SBRs, respectively. This growth in algae also increased the Chl. *a* to suspended biomass ratio to 20.3 and 13.01 mg g⁻¹ in the MAIFAS and suspended reactors, respectively. MLVSS decreased by 43% in the IFAS control and 26% in the MAIFAS. This decrease was likely attributed to the decreased influent COD concentration in Phase II. While there was an initial decline in nutrient removal during Phase II in the MAIFAS and suspended SBRs, nutrient removal was relatively improved after 40 days in Phase II. The control IFAS

reactor was still able to remove all 70 mg N-NH₃ L⁻¹ ammonia of influent (100% ammonia removal). The adjusted experimental conditions impeded P removal in the control IFAS reactor which may be due to the decreased suspended biomass (MLVSS) (< 1,000 mg L⁻¹) (Fig. 3-3(a)); however, the reactors with algae, MAIFAS and suspended, demonstrated 51 and 98% P removal, respectively. Furthermore, the algae bacteria consortia showed excellent settling with a sludge volume index (SVI) ranging from 74 to 160 with less than 1 mg L⁻¹ Chl. *a* in the effluent (Fig. B4).

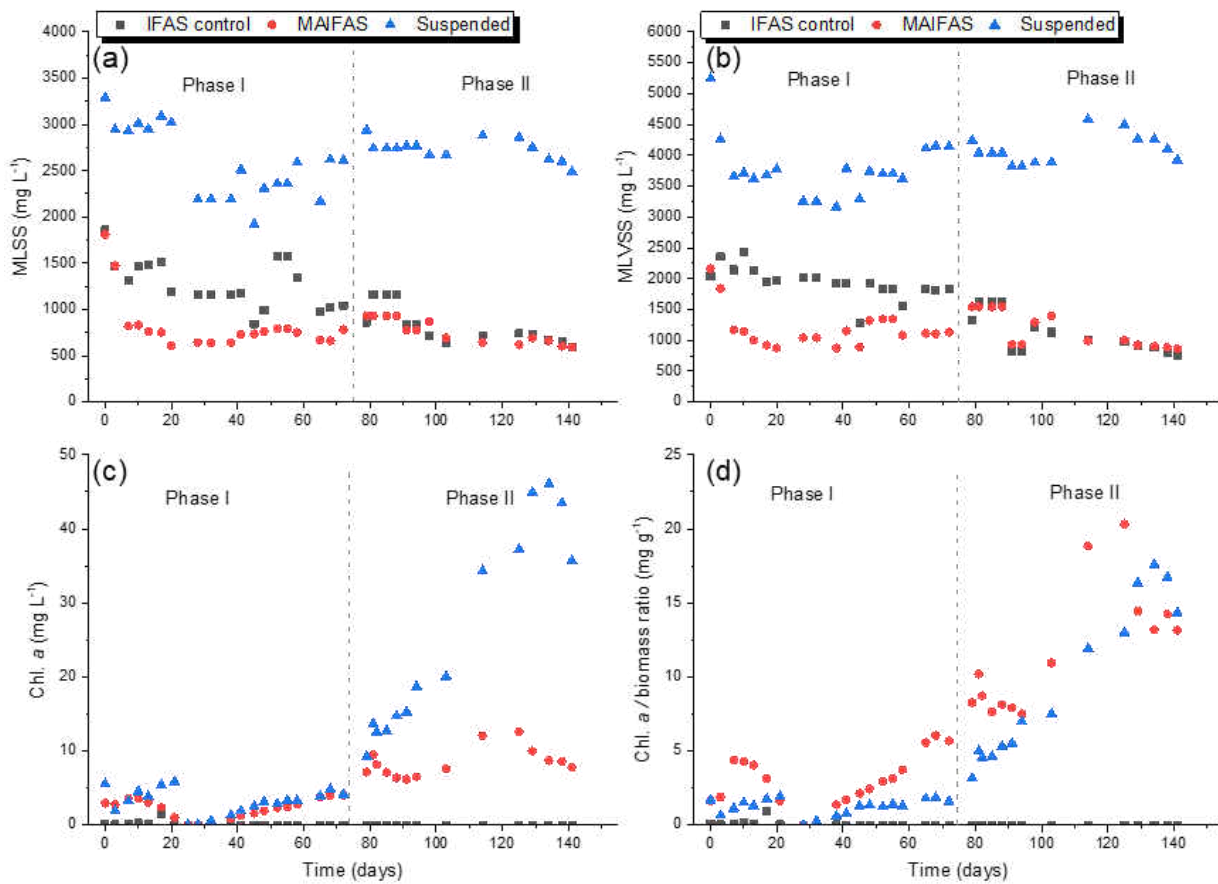


Figure 3- 3. (a) MLSS, (b) MLVSS, (c) Chl. *a* and (d) Chl. *a*/biomass ratio in IFAS control, MAIFAS and suspended algae control SBRs over 150 days. Biomass samples were taken during the aerobic phase. Mechanical aeration was applied to all reactors during the aerobic sequence of Phase I. Only light was applied to MAIFAS and suspended reactors during the aerobic sequence of Phase II.

There was a slight increase in effluent pH in the suspended reactors from Phase I (pH 8.2) to Phase II (pH 8.5) (Fig. 3-2(a)), indicating algal growth and increased photosynthetic activity in the reactors. While pH increases may have stripped some ammonia from the system, the highest pH observed during the aerated phase was 8.5, indicating that the majority of the ammonia removal was biological N removal, not ammonia stripping.

Photo-aeration using microalgae

DO was carefully monitored throughout the experiments (Phase I and II) to evaluate microalgae photo-aeration as an alternative to energy-intensive mechanical aeration. Bulk DO concentration was monitored without mechanical aeration in the algae reactors during the entire SBR cycle for each reactor at 30 d, 60 d and 90 d after inoculation (Fig. 3-4). It appears that the microalgae do not provide enough DO for nitrification at 30 and 60 d (Phase I), requiring the change of influent water quality and more time for stable algal growth in the system. At 90 d (Phase II), DO concentration increased to $1.3 \text{ mg O}_2 \text{ L}^{-1}$ and $0.6 \text{ mg O}_2 \text{ L}^{-1}$ in the MAIFAS and suspended SBRs, respectively, indicating photo-aeration. The IFAS control reactor was mechanically aerated during the aerobic phases of the SBR cycle; hence, the DO reached saturation during this phase. This finding demonstrates that microalgae can provide sufficient oxygen required for nitrification and COD removal particularly when the Chl. *a* to biomass ratio exceeds 7.9 mg g^{-1} (MAIFAS Chl. *a* to biomass ratio after 90 days). A study by Wang et al. (2015) found similar results for a photo-SBR that was used to process the liquid fraction of anaerobically digested swine manure. They found that a Chl. *a* to biomass ratio of approximately 24 mg g^{-1} was able to supply 74% of the required DO for nitrification.

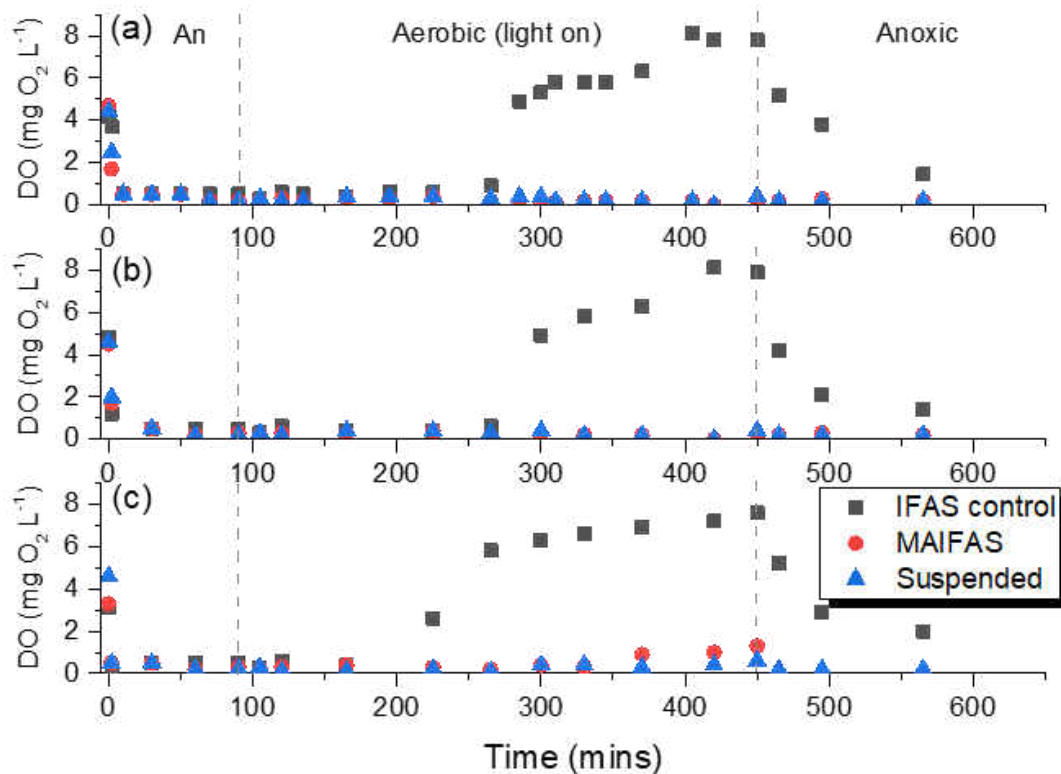


Figure 3- 4. DO concentrations during an SBR cycle after (a) 30, (b) 60 and (c) 90 days of growth. Mechanical aeration was applied to IFAS control during aerobic phase. $76.2 \mu\text{mol m}^{-2} \text{S}^{-1}$ of fluorescent light (no mechanical aeration) was applied to the MAIFAS and Suspended reactors during aerobic phase.

While DO concentrations in the bulk provided some indication of photo-aeration, direct oxygen transfer measurements within a microalgal-bacteria biofilm provides valuable kinetic information. Therefore, DO microsensors were used to measure DO concentration microprofiles from the bulk into the biofilms of the MAIFAS and IFAS SBRs which were taken after 40, 80, 130, and 150 d of operation (Fig. 3-5). The microprofile measurements were conducted between dark and light conditions to confirm the photo-aeration by algal biofilm. Biofilm thickness was 600, 1,300, 1,800, and 2,100 μm at 40, 80, 130, and 150 days of operations, respectively. DO concentration microprofiles after 40 days of biofilm growth (Fig. 3-5(a)) showed a decrease in

DO from 3.0 mg O₂ L⁻¹ in the bulk phase to 0.2 mg O₂ L⁻¹ at the substrate with a 100 μm diffusion boundary layer (DBL) which indicates the activity of aerobic bacteria (nitrifiers and heterotrophs) within the biofilm. When the light was turned off, there was an initial decrease by 0.5 mg O₂ L⁻¹ from 1,500 to 600 μm, after which the O₂ concentration decreased to 0.32 mg O₂ L⁻¹. After 80 d, biofilm thickness was increased to 1,300 μm. The DO profile exhibited a 1 mg O₂ L⁻¹ increase in DO at the biofilm surface (Fig. 3-5(b)) by microalgal photosynthetic oxygen production. After 130 d of operation (55 days of Phase II), DO concentrations increased to 6.8 mg O₂ L⁻¹ at the surface of the biofilm with the lights on. ΔDO between light on and off was 3.3 mg O₂ L⁻¹ (Fig. 3-5(c)). This large amount of oxygen production at the biofilm surface made it possible for DO to penetrate into the whole biofilm where DO was present at the substratum (0.3 mg O₂ L⁻¹) which means the underlying nitrifying biofilm had ample supply of oxygen for nitrification. Without light, the bulk DO penetrated only 69% of the total biofilm thickness. This outcome shows that there was an algal biofilm present on top of the bacterial biofilm which can assist in photo-aeration and this localized algal photo-aeration improved the utilization of aerobic bacteria throughout the biofilm depth, which was not possible through mechanical aeration. Altogether, these findings provide evidence of the feasibility of a microalgae-based IFAS wastewater treatment process to achieve low energy consumption while meeting stringent effluent standards using symbiotic microalgae fluidized media. A microscopic cross-sectional image of the biofilm shows the bottom layer is comprised mostly of a dense mixed culture nitrifying biofilm where the top layer is a mixture of algae and heterotrophic bacteria (Fig. 3-6). In addition, DO consumption within the biofilm was faster at the base of the biofilm (0-600μm) compared to the top layer of biofilm (>600μm) (Fig. 3-5). This clearly shows well-defined stratification of microbiological communities between the top and bottom layer. This

configuration of bacterial communities seems possible considering nitrifying bacteria are known to be photosensitive (Kaplan et al., 2000).

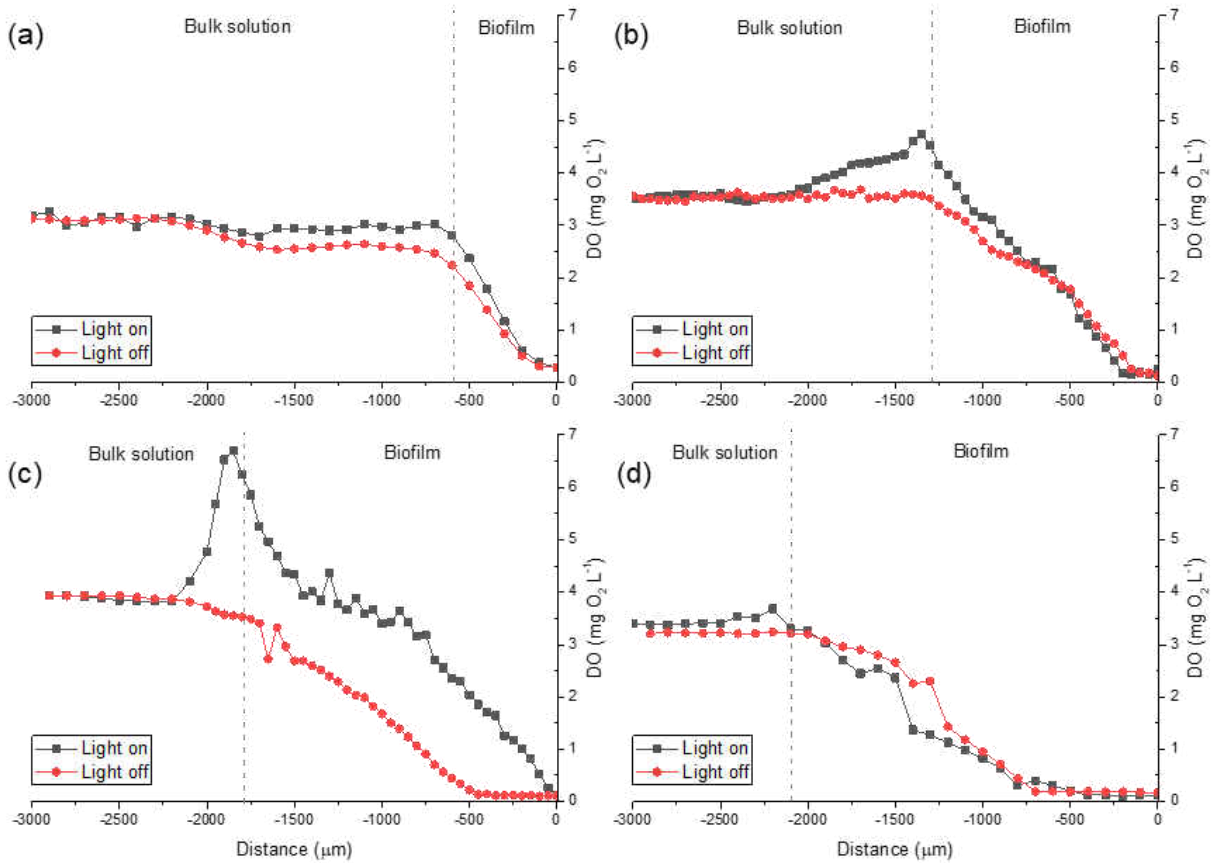


Figure 3- 5. DO microprofiles of MAIFAS biofilms under $76.2 \mu\text{mol m}^{-2} \text{S}^{-1}$ of white fluorescent light and darkness after (a) 40 days, (b) 80 days, (c) 130 days and (d) 150 days of growth. Reference lines represent biofilm thickness over time.

After 150 d, the DO concentration microprofiles of MAIFAS biofilms displayed the loss of a photo-oxygenating layer on the surface of the biofilm, showing no difference between light and dark conditions with a similar DO decreases from $3 \text{ mg O}_2 \text{ L}^{-1}$ in the bulk to $0 \text{ mg O}_2 \text{ L}^{-1}$ at $800 \mu\text{m}$ above the substrate surface (Fig. 3-5(d)). Therefore, the lower nitrifying biofilm appears to be unable to get oxygen for nitrification. This is consistent with the fact that ammonia removal decreased from 99% on day 130 to 11% on day 150 (Fig. 3-2(b)). It is still unclear why there was a significant loss of the phototrophic biofilm at this time of operation. A possible explanation for

the loss of the photo-oxygenating microalga biofilm would be algal biofilm sloughing due to the precedent nutrient starvation (100% ammonia removal) (Schnurr et al. 2013), decreasing algal growth from days 129 to 141 (Fig. 3-3(c)).

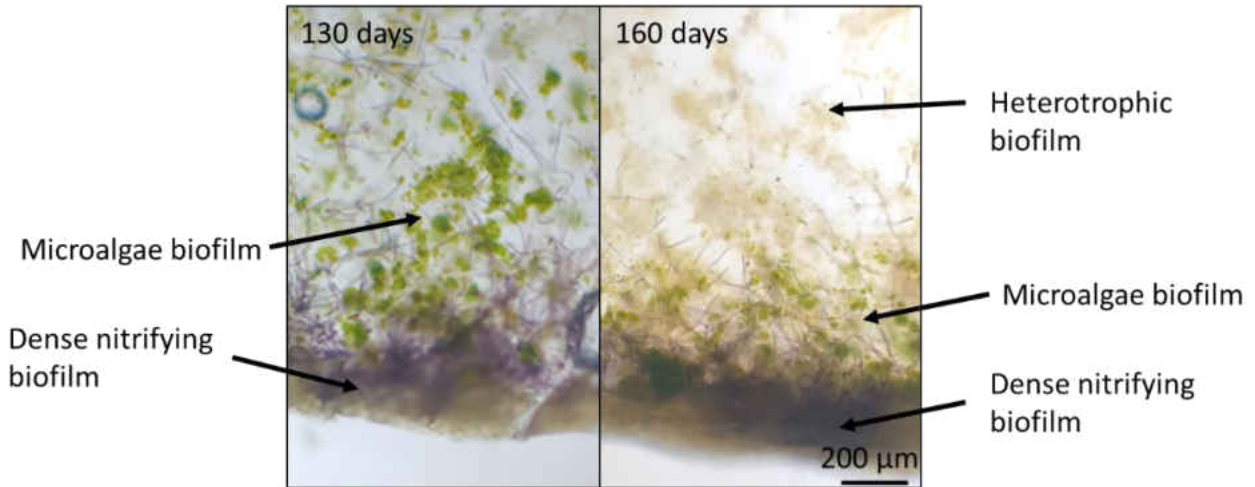


Figure 3- 6. Cross-sectional image ($\times 40$ magnification and $50\mu\text{m}$ thickness) of MAIFAS biofilm at 130 and 160 days. The biofilm was mounted in tissue freezing media.

Interactions between algal and bacteria biofilms

To further understand the interactions between algal and bacteria biofilms, pH and ammonia concentration microprofiles were measured in Phase II of MAIFAS operation. pH decreased from 7.3 to 6.7 in the lower $1,000\ \mu\text{m}$ of the biofilm when the light was on (Fig. 3-7(a)), indicating consumption of alkalinity and nitrification. In addition, there was a slight pH increase ($600\ \mu\text{m}$ above the biofilm surface), from 7.3 to 7.4, which indicates photosynthesis. Likewise, ammonia concentration decreased from $72\ \text{mg N L}^{-1}$ to $67\ \text{mg N L}^{-1}$ in the lower $250\ \mu\text{m}$ of the biofilm (Fig. 3-7(b)). This finding was interesting because there was no consumption of ammonia in the upper portion of the biofilm meaning the algal portion of the biofilm was not consuming

ammonia. Hence, the role of algae biofilm in the MAIFAS reactor is mostly aiding photo-oxygenation.

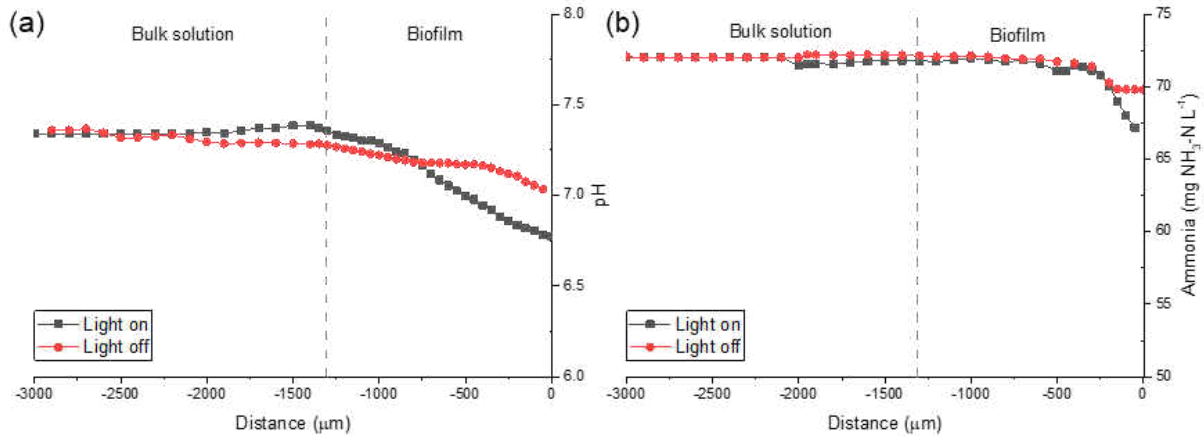


Figure 3- 7. (a) pH and (b) ammonia microprofiles of MAIFAS biofilms under $76.2 \mu\text{mol m}^{-2} \text{S}^{-1}$ of white fluorescent light and darkness after 140 days of growth. Reference lines represent biofilm thickness over time.

Genetic diversity of algae-bacteria consortia for wastewater treatment

A total of 70,525 and 69,592 sequences were analyzed from the rDNA and rRNA libraries and used to describe the bacterial composition and identity of metabolically active bacteria between the MAIFAS and the IFAS reactors. The sequencing data suggested that there were some similarities in bacterial composition between the reactors. Each reactor included members of bacterial phyla such as Proteobacteria (e.g., alpha-, beta- and gamma-Proteobacteria), Bacteroidetes (*Cytophagia*, *Flavobacteriia*, *Saprospirae*), Nitrospirae (*Nitrospira*), and Acidobacteria (*Chloracidobacterium*) (Table 3-1). However, there were some striking differences in relative abundance between reactor types. For example, while members of the beta-proteobacteria were among the most abundant groups in both reactors, some of the species were more prevalent in one reactor type. Specifically, *Candidatus Accumulibacter* was predominant in the MAIFAS reactor but barely detected in the IFAS reactor. In contrast, *Dechloromonas* represented >5% of the sequences in the IFAS reactor versus < 0.4% in the

MAIFAS reactor. A similar result was observed for *Acinetobacter* (*gamma*-Proteobacteria) as far as its relative abundance in the IFAS reactor was concerned.

Differences in relative abundance of several bacterial groups were also noted when sequencing library type results were compared. In the MAIFAS reactor, *Candidatus Accumulibacter* were more abundant in the rRNA (55%) than in the rDNA sequencing library (< 1%). In both reactors *Comamonadaceae*- and *Nitrosomonadaceae*-like sequences were more abundant in the rRNA sequencing libraries. In the IFAS reactor, *Acinetobacter* was more than twice as abundant in the rRNA library than in the rDNA library. In other cases, the abundance of a bacterial group decreased in the rRNA libraries. This was the case for *Aeromonas*, *Lysobacter*, *Nitrospira*, *Flavobacteriia*, and *Saprospirae*. Sequences related to members of the phylum *Caldithrix* were greater in the MAIFAS rRNA while totally absent in the IFAS reactor. The presence of this bacterial group is intriguing as it has primarily been associated with hydrothermal sediments and considered to be nitrate reducing bacteria and obligately anaerobic (Miroshnichenko et al. 2003). Although the role of *C. abyssi* in the MAIFAS reactor is unknown at this point, genome sequencing analysis of has revealed that carbohydrates such as starch, cellobiose, glucomannan and xyloglucan several can support its growth (Kublanov et al. 2017). As rRNA transcripts are associated with protein synthesis, rRNA-based data have been used as a proxy for assessing the relative activity levels in several aquatic matrices (Pitkänen et al. 2013, Revetta et al. 2011). Moreover, shifts in rRNA:rDNA ratios may signal overall changes in relative metabolic activity in a given bacterial group (Kapoor et al. 2015a, Kapoor et al. 2015b). Using this rationale, our data suggest that some groups are not only present in the reactor but more metabolically active than other groups. For example, rRNA:rDNA ratios suggest that *Nitrosomonadaceae* may be more actively involved in nitrogen removal than *Nitrospira*,

particularly in the MAIFAS reactor. However, the fact that both nitrifying bacterial groups are present suggests that they might be occupying different ecological niches within these reactors. Moreover, several *Nitrosomonas* species were identified (e.g., *N. communis*, *N. europaea*, *N. oligotropha*, *N. ureae*), suggesting that ammonia removal is conducted by multiple populations. Additionally, the lower rRNA:rDNA ratios of several members of Bacteroidetes suggest that they are not removing organic carbon at a high rate as implied by their abundances in the rDNA libraries. Low metabolic activity of *Bacteroidetes* have also been observed in wastewater nitrifying enrichments (Kapoor et al. 2016).

Table 3- 1. Distribution of bacterial 16S rRNA and 16S rDNA

Class	Genus	MAIFAS-Mean		IFAS-Mean	
		RNA (n=8584)	DNA (n=8570)	RNA (n=8714)	DNA (n=9234)
Alpha-Proteobacteria	<i>Rhodobacteraceae</i> *	-	18	33	145 (1.6%)
	<i>Woodsholea</i>	14	127 (1.5%)	93 (1.1%)	97 (1.1%)
Beta-Proteobacteria	<i>Candidatus</i>	4719 (55%)	754 (8.8%)	64	44
	Accumulibacter				
	<i>Comamonadaceae</i> *	603 (7.0%)	192 (2.2%)	904 (10%)	377 (4.1%)
	<i>Nitrosomonadaceae</i> *	126 (1.5%)	29	208 (2.4%)	30
	<i>Nitrosomonas</i>	62	16	70	14
	<i>Dechloromonas</i>	34	36	477 (5.5%)	565 (6.1%)
	<i>Zoogloea</i>	39	113 (1.3%)	220 (2.5%)	399 (4.3%)
	Unclassified	701 (8.2%)	620 (7.2%)	3576 (41%)	2368 (26%)
Gamma-Proteobacteria	<i>Acinetobacter</i>	20	26	806 (9.3%)	379 (4.1%)
	<i>Aeromonas</i>	-	90 (1.1%)	17	308 (3.3%)
	<i>Lysobacter</i>	-	45	62	110 (1.2%)
	<i>Rheinheimera</i>	-	-	42	51
Nitrospira	<i>Nitrospira</i>	21	89 (1.0%)	131 (1.5%)	322 (3.5%)
Acidobacteria	<i>Chloracidobacterium</i>	21	124 (1.5%)	411 (4.7%)	304 (3.3%)
Cyanobacteria**	Unclassified	21	50	29	15
Cytophagia	<i>Cytophagaceae</i> *	-	58	-	64
	Unclassified	-	146 (1.7%)	80	428 (4.6%)
Flavobacteriia	<i>Flavobacterium</i>	-	-	-	107 (1.2%)
	<i>Cloacibacterium</i>	-	-	17	191 (2.1%)
Phycisphaerae	Unclassified	23	103 (1.2%)	46	55
Saprospirae	<i>Chitinophagaceae</i> *	-	683 (8.0%)	21	902 (9.8%)
	<i>Saprospiraceae</i> *	72	1558 (18%)	-	59
Unclassified	<i>Caldithrix</i>	183 (2.1%)	17	-	-

* Family, ** Phylum, - less than 10 sequences

Also notable is the fact that *Candidatus Accumulibacter*-like sequences were relatively rare in the IFAS reactor while over six times more abundant in the rRNA libraries than in the rDNA libraries in the MAIFAS reactor, suggesting that this bacterial group may be playing an active role in P removal in the algae-seeded reactors (MAIFAS). Previous studies have reported *Candidatus Accumulibacter phosphatis* as a dominant member of enhanced biological phosphorus removal (EBPR) sludge microbial communities (Flowers et al. 2013). In fact, *Candidatus Accumulibacter* is capable of P removal in wastewater enrichments employing different oxygenic conditions (Camejo et al. 2016). Also related to P removal were the dynamics of *Dechloromonas spp.* whose relative abundance significantly decreased in the MAIFAS samples. Members of this genus have been shown to accumulate polyphosphate. As other potential PAO were not detected or were present in very low numbers, the results of this study implicate *Candidatus Accumulibacter* and *Dechloromonas* as the primary P removing bacteria in the MAIFAS and IFAS, respectively. The role of difficult to classify beta-proteobacteria cannot be discarded. Our data strongly suggest that there may be biochemical interactions between the microalgae and different bacterial groups that promote the enrichment, and furthermore, stimulate the metabolic activity of *Candidatus Accumulibacter*, resulting in an increase of P removal.

Discussion

MAIFAS vs. suspended micro-algae bacteria consortium for nutrient removal in wastewater

The MAIFAS system removed >99% ammonia and 51% P without the need for mechanical aeration, a marked improvement over the suspended microalgae sludge control, which only removed 57% ammonia and 49% P from synthetic wastewater. Ammonia removal in suspended microalgae-bacteria reactors were comparable to other microalgae wastewater treatment studies.

He et al. (2013) observed 97% ammonia removal in municipal wastewater (29–174 mg NH₄⁺-N L⁻¹) and Zhao et al. (2014) reported 90% TN removal in landfill leachate (261 mg NH₄⁺-N L⁻¹) using a microalgae-bacteria consortium.

N removal in these systems were reported to be achieved through N assimilation by biomass and nitrification/denitrification pathways. For example, Su et al. (2012) found that 61–93% of N removal was due to N assimilation. Wang et al. (2015) proposed a shortcut N removal mechanism in suspended algal bacteria systems where low DO and carbon concentrations favored ammonia oxidizing bacteria (AOB) over nitrite oxidizing bacteria (NOB) activity in the presence of algae. This removal process required less DO and organic carbon compared to conventional biological nutrient removal (BNR) processes. In the current study, 16S rRNA gene sequencing analysis of the MAIFAS biofilms suggests that this shortcut N removal may be significant in our system with relatively high abundance of AOB (1.5% *Nitrosomonadaceae*) compared to NOB (0.2% *Nitrospira*).

Biological P removal using algae-based biological processes is less common than N removal, but can be achieved. For example, Gonzales et al. (2008) found 80% P removal from swine manure wastewater using *Chlorella sorokiniana* suspension and Posadas et al. (2013) reported 85% removal from domestic wastewater using a suspended mixed algae culture. A biofilm study showed only a 34% removal from dairy manure using an algal turf scrubber.

In the current study, it was found that P removal was similar between the MAIFAS and suspended algae reactors in Phase II with an average of 51% removal from both reactors. Based on this observation it is likely the suspended portion of the biomass that is responsible for P removal. In fact, we found that P removal is not necessarily dependent on Chl. *a* to biomass ratio in the MAIFAS reactor system, suggesting that P removal may not be attributed to algal

assimilation. 16s rRNA sequencing revealed high concentrations of *Candidatus Accumulibacter* in MAIFAS biofilms compared to the IFAS control (55% vs. <1%) likely due to EBPR's contribution in P removal in microalgae systems.

Effect of Chl. *a* to biomass ratio on nutrient removal

Several studies have noted the importance of algae to biomass ratio for nitrification in algal-bacterial consortia (Su et al., 2012). A study by Medina and Neis (2007) demonstrated that increasing Chl. *a* to biomass ratios (1 to 34 mg chl. *a*/ g SS) increased TN removal. In this study, ammonia removal was compared to Chl. *a* to biomass ratio in Phase I and II between the MAIFAS and suspended reactors (Fig. 3-8) to elucidate N and P removal mechanisms by algal-bacterial symbiosis. Chl. *a* to biomass ratio appeared to have no effect on ammonia removal in Phase I when the reactor was being mechanically aerated. This means that the activated sludge was responsible for majority of the ammonia removal under mechanically aerated conditions. During Phase II, the Chl. *a* to biomass ratio had impacts on ammonia removal in the MAIFAS and suspended reactors (Fig. 3-8(c)). Both reactors show increasing ammonia removal with increasing Chl. *a* to biomass ratio; however, the MAIFAS reactor had better ammonia removal compared to the suspended reactor (Fig. 3-8(c)). This could be due to the fact that ammonia oxidizing bacteria (AOB) are photosensitive (Kaplan et al., 2000) and light intensity was increased for Phase II. For Chl. *a* to biomass ratio, both reactors followed a similar trend where for every 1 mg Chl. *a* g⁻¹ VSS increase there was a 3.1% increase in ammonia removal. Therefore, microalgae are presumably responsible for removing ammonia either through assimilation or by providing oxygen for nitrification. A similar study using *Scenedesmus sp.* algae and bacterial flocs for wastewater treatment estimated 13% of N was removed via algal assimilation and 85% of N was removed via photo-aeration for nitrification (Karya et al., 2013).

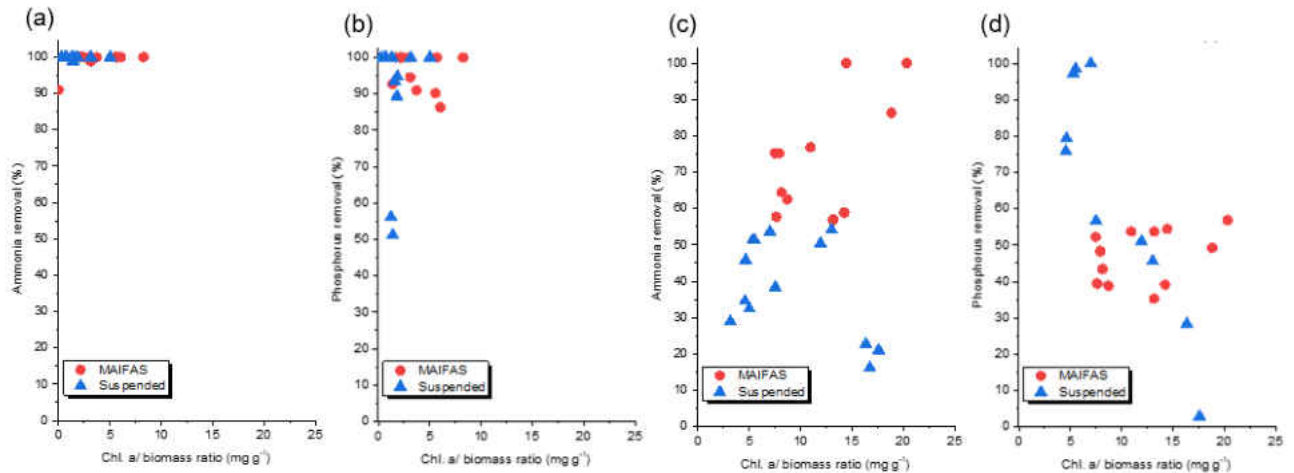


Figure 3- 8 Effect of Chl. *a* to biomass ratio on a) ammonia removal and b) phosphorus removal during mechanical aeration (Phase I) and c) ammonia removal and d) phosphorus removal during photoaeration (Phase II).

While N removal by algal-bacterial consortia has been well studied, P removal using algal bacteria consortia is still in early stages of investigation and the mechanism for P removal is not well understood. Our data shows that when the algal-bacterial consortium was mechanically aerated (Phase I), P removal was not related to Chl. *a* to biomass ratio (Fig. 3-8(b)). This finding suggests that with mechanical aeration (Phase I), algae was not responsible for significant amounts of P removal. During Phase II, the role of algae in P removal appears to be different between the MAIFAS and suspended reactors. In the MAIFAS reactor, P removal was comparable between 35% and 51% despite Chl. *a* to biomass ratio. However, the suspended reactor showed decreased P removal with increased Chl. *a* to biomass ratio, indicating that unlike ammonia removal, P removal depends primarily on wasting of suspended bacteria. From the bacterial community analysis, a large amount of *Candidatus* Accumulibacter was found in the biofilms of the MAIFAS reactor (55% of 16S rDNA sequences). Given that P removal only occurs through wasting, it is likely that a significant *Candidatus* Accumulibacter population in the suspended biomass of the MAIFAS reactor was contributing to P removal.

Interactions between algal and bacteria biofilms

There is limited information on the interactions between algal and nitrifying biofilms; however, there are many studies that evaluate algal biofilms for nutrient removal. For example, algal turf scrubbers have been shown to remove an average of $1,110 \text{ mg N m}^{-2} \text{ d}^{-1}$ (Craggs, 1996) and RABR have achieved nitrogen removal rates of $14,100 \text{ mg N m}^{-2} \text{ d}^{-1}$ (Christenson and Sims, 2012). Therefore, it was expected that the algal biofilms in the MAIFAS reactor would contribute significantly to ammonia removal; however, microprofiles revealed no ammonia consumption in the algal portion of the biofilm. While the reason for this is unclear, the role of microalgae in the MAIFAS system was to provide oxygen to the nitrifying biofilm and protect the nitrifying biofilm from sloughing (Babu, 2011).

Challenges and future prospects

Integrating microalgae with IFAS configuration can provide many benefits including reduced the costs of mechanical aeration, uncoupling SRTs of suspended and biofilms for reduced footprint, and potential application as feedstock for biofuel production. This study has demonstrated >99% ammonia removal and 51% P removal without the need for mechanical aeration or carbon addition. However, any microalgae-based wastewater treatment technologies come with inherent challenges (e.g., the need for sustained sunlight for photo-aeration must be satisfied). While the developed MAIFAS system demonstrated promising results, controlling the growth of algal biofilm can be challenging and the effect of co-growth of bacteria and algae in IFAS media on nutrient removal can be compounded in the operation of algal-biofilm processes. For example, when algal growth rate decreases, there is a loss of nutrient removal due to the reduced photo-aeration as well as the formation of new biofilms on top of the algal biofilms, reducing available light for photosynthesis. It was also found that it takes time to stabilize the

MAIFAS system and there is significant variability in nutrient removal in the MAIFAS operation (Fig. 3-3). Therefore, it is important to fully understand the ecology of algal-bacterial interactions in algae-based technologies. Future work in this direction would aim to reduce the SRT to avoid the growth of heterotrophic bacteria over the fast-growing microalgae in suspended portions or select local algal strains that are better suited for maintaining healthy microbial communities. In addition, although *C. vulgaris* was used as the seed algae, it may not be the dominant algae in a mature system. Thus, time-course analysis of the algal community is required to evaluate the stability of the MAIFAS system.

Conclusions

The removal of N and P from synthetic wastewater was investigated in a novel MAIFAS SBR over 150 days. Microalgae photosynthesis was able to provide sufficient oxygen for advanced wastewater treatment (>99% ammonia and 51% P removal in the MAIFAS reactor). A microelectrode investigation revealed localized aeration in the MAIFAS biofilms. It was found that both growth rate of algae and the Chl. *a* to biomass ratio both were important parameters pertaining to nutrient removal, predominantly in suspended microalgal-bacteria wastewater systems. The addition of microalgae to the IFAS system promoted significant changes in the bacterial community structure and the metabolic activity of several bacterial groups. In particular, *Candidatus Accumulibacter* contributed to 55% of the rRNA in the MAIFAS biofilm but less than 1% of the IFAS biofilms. Overall, this research represents a novel strategy for reducing energy costs while meeting stringent effluent standards using a hybrid symbiotic microalgae-based IFAS technology.

References

- APHA, AWWA, and WEF. (1995) Standard methods for the examination of water and wastewater, American Public Health Association.
- Camejo, P.Y., Owen, B.R., Martirano, J., Ma, J., Kapoor, V., Santo Domingo, J., McMahon, K.D. and Noguera, D.R. (2016) Candidatus *Accumulibacter phosphatis* clades enriched under cyclic anaerobic and microaerobic conditions simultaneously use different electron acceptors. *Water research* 102, 125-137.
- Caporaso, J.G., Lauber, C.L., Walters, W.A., Berg-Lyons, D., Lozupone, C.A., Turnbaugh, P.J., Fierer, N. and Knight, R. (2011) Global patterns of 16S rRNA diversity at a depth of millions of sequences per sample. *Proceedings of the National Academy of Sciences* 108(Supplement 1), 4516-4522.
- Chisti, Y. (2007) Biodiesel from microalgae. *Biotechnology advances* 25(3), 294-306.
- Church, J., Hwang, J.-H., Kim, K.-T., McLean, R., Oh, Y.-K., Nam, B., Joo, J.C. and Lee, W.H. (2017) Effect of salt type and concentration on the growth and lipid content of *Chlorella vulgaris* in synthetic saline wastewater for biofuel production. *Bioresource technology* 243, 147-153.
- De-Bashan, L.E., Moreno, M., Hernandez, J.-P. and Bashan, Y. (2002) Removal of ammonium and phosphorus ions from synthetic wastewater by the microalgae *Chlorella vulgaris* coimmobilized in alginate beads with the microalgae growth-promoting bacterium *Azospirillum brasilense*. *Water Research* 36(12), 2941-2948.
- EPA. (2006) Office of Water, Wastewater Management Fact Sheet, Energy Conservation, EPA 832-F-06-024, U.S. Environmental Protection Agency, Washington DC.
- Flowers, J.J., Cadkin, T.A. and McMahon, K.D. (2013) Seasonal bacterial community dynamics in a full-scale enhanced biological phosphorus removal plant. *Water research* 47(19), 7019-7031.
- Fredy, D., Lens, P. and van der Steen, P. (2013) Nitrification and denitrification by algal-bacterial biomass in a sequential batch photo-bioreactor: effect of SRT, Unesco-IHE.
- González, C., Marciniak, J., Villaverde, S., García-Encina, P.A. and Muñoz, R. (2008a) Microalgae-based processes for the biodegradation of pretreated piggery wastewaters. *Applied microbiology and biotechnology* 80(5), 891-898.
- He, P., Mao, B., Lü, F., Shao, L., Lee, D. and Chang, J. (2013) The combined effect of bacteria and *Chlorella vulgaris* on the treatment of municipal wastewaters. *Bioresource technology* 146, 562-568.
- Hwang, J.-H., Church, J., Lee, S.-J., Park, J. and Lee, W.H. (2016) Use of microalgae for advanced wastewater treatment and sustainable bioenergy generation. *Environmental Engineering Science* 33(11), 882-897.
- Jabari, P., Munz, G. and Oleszkiewicz, J.A. (2014) Selection of denitrifying phosphorous accumulating organisms in IFAS systems: comparison of nitrite with nitrate as an electron acceptor. *Chemosphere* 109, 20-27.
- Kaplan, D., Wilhelm, R. and Abeliovich, A. (2000) Interdependent environmental factors controlling nitrification in waters. *Water Science and Technology* 42(1-2), 167-172.

Kapoor, V., Elk, M., Li, X., Impellitteri, C.A. and Santo Domingo, J.W. (2016) Effects of Cr (III) and Cr (VI) on nitrification inhibition as determined by SOUR, function-specific gene expression and 16S rRNA sequence analysis of wastewater nitrifying enrichments. *Chemosphere* 147, 361-367.

Kapoor, V., Li, X., Elk, M., Chandran, K., Impellitteri, C.A. and Santo Domingo, J.W. (2015a) Impact of heavy metals on transcriptional and physiological activity of nitrifying bacteria. *Environmental science & technology* 49(22), 13454-13462.

Kapoor, V., Pitkänen, T., Ryu, H., Elk, M., Wendell, D. and Santo Domingo, J.W. (2015b) Distribution of human-specific bacteroidales and fecal indicator bacteria in an urban watershed impacted by sewage pollution, determined using RNA- and DNA-based quantitative PCR assays. *Applied and environmental microbiology* 81(1), 91-99.

Karya, N., van der Steen, N. and Lens, P. (2013) Photo-oxygenation to support nitrification in an algal-bacterial consortium treating artificial wastewater. *Bioresource technology* 134, 244-250.

Kim, H.S., Gellner, J.W., Boltz, J.P., Freudenberg, R.G., Gunsch, C.K. and Schuler, A.J. (2010) Effects of integrated fixed film activated sludge media on activated sludge settling in biological nutrient removal systems. *Water research* 44(5), 1553-1561.

Kublanov, I.V., Sigalova, O.M., Gavrilov, S.N., Lebedinsky, A.V., Rinke, C., Kovaleva, O., Chernyh, N.A., Ivanova, N., Daum, C. and Reddy, T. (2017) Genomic analysis of *Caldithrix abyssi*, the thermophilic anaerobic bacterium of the novel bacterial phylum Calditrarchaeota. *Frontiers in microbiology* 8.

Lee, W.H., and Bishop, P.L. (2009). *In situ* microscale analyses of activated sludge flocs in the enhanced biological phosphate removal process by the use of microelectrodes and fluorescent in situ hybridization. *Journal of Environmental Engineering* 136(6), 561-567.

Lewandowski, Z., and Beyenal, H. (2013). *Fundamentals of biofilm research*. CRC press
Medina, M. and Neis, U. (2007) Symbiotic algal bacterial wastewater treatment: effect of food to microorganism ratio and hydraulic retention time on the process performance. *Water science and technology* 55(11), 165-171.

Miroshnichenko, M.L., Kostrikina, N.A., Chernyh, N.A., Pimenov, N.V., Tourova, T.P., Antipov, A.N., Spring, S., Stackebrandt, E. and Bonch-Osmolovskaya, E.A. (2003) *Caldithrix abyssi* gen. nov., sp. nov., a nitrate-reducing, thermophilic, anaerobic bacterium isolated from a Mid-Atlantic Ridge hydrothermal vent, represents a novel bacterial lineage. *International journal of systematic and evolutionary microbiology* 53(1), 323-329.

Onnis-Hayden, A., Majed, N., Schramm, A. and Gu, A.Z. (2011) Process optimization by decoupled control of key microbial populations: Distribution of activity and abundance of polyphosphate-accumulating organisms and nitrifying populations in a full-scale IFAS-EBPR plant. *Water research* 45(13), 3845-3854.

Pate, R., Klise, G. and Wu, B. (2011) Resource demand implications for US algae biofuels production scale-up. *Applied Energy* 88(10), 3377-3388.

Pitkänen, T., Ryu, H., Elk, M., Hokajärvi, A.-M., Siponen, S., Vepsäläinen, A., Räsänen, P. and Santo Domingo, J.W. (2013) Detection of fecal bacteria and source tracking identifiers in environmental waters

using rRNA-based RT-qPCR and rDNA-based qPCR assays. *Environmental science & technology* 47(23), 13611-13620.

Posadas, E., García-Encina, P.-A., Soltau, A., Domínguez, A., Díaz, I. and Muñoz, R. (2013) Carbon and nutrient removal from centrates and domestic wastewater using algal–bacterial biofilm bioreactors. *Bioresource technology* 139, 50-58.

Quast, C., Pruesse, E., Yilmaz, P., Gerken, J., Schweer, T., Yarza, P., Peplies, J. and Glöckner, F.O. (2012) The SILVA ribosomal RNA gene database project: improved data processing and web-based tools. *Nucleic acids research* 41(D1), D590-D596.

Revetta, R.P., Matlib, R.S. and Santo Domingo, J.W. (2011) 16S rRNA gene sequence analysis of drinking water using RNA and DNA extracts as targets for clone library development. *Current microbiology* 63(1), 50-59.

Rosso, D., Stenstrom, M. and Larson, L. (2008) Aeration of large-scale municipal wastewater treatment plants: state of the art.

Schloss, P.D., Westcott, S.L., Ryabin, T., Hall, J.R., Hartmann, M., Hollister, E.B., Lesniewski, R.A., Oakley, B.B., Parks, D.H. and Robinson, C.J. (2009) Introducing mothur: open-source, platform-independent, community-supported software for describing and comparing microbial communities. *Applied and environmental microbiology* 75(23), 7537-7541.

Sriwiriyarat, T. and Randall, C. (2005) Performance of IFAS wastewater treatment processes for biological phosphorus removal. *Water Research* 39(16), 3873-3884.

Su, Y., Mennerich, A. and Urban, B. (2012) Synergistic cooperation between wastewater-born algae and activated sludge for wastewater treatment: Influence of algae and sludge inoculation ratios. *Bioresource technology* 105, 67-73.

Wang, L., Min, M., Li, Y., Chen, P., Chen, Y., Liu, Y., Wang, Y. and Ruan, R. (2010) Cultivation of green algae *Chlorella* sp. in different wastewaters from municipal wastewater treatment plant. *Applied biochemistry and biotechnology* 162(4), 1174-1186.

Wang, M., Yang, H., Ergas, S.J. and van der Steen, P. (2015) A novel shortcut nitrogen removal process using an algal-bacterial consortium in a photo-sequencing batch reactor (PSBR). *Water research* 87, 38-48.

Wang, Q., Garrity, G.M., Tiedje, J.M. and Cole, J.R. (2007) Naive Bayesian classifier for rapid assignment of rRNA sequences into the new bacterial taxonomy. *Applied and environmental microbiology* 73(16), 5261-5267.

Zhao, X., Zhou, Y., Huang, S., Qiu, D., Schideman, L., Chai, X. and Zhao, Y. (2014) Characterization of microalgae-bacteria consortium cultured in landfill leachate for carbon fixation and lipid production. *Bioresource technology* 156, 322-328.

CHAPTER FOUR: APPLICATION OF MICROSENSORS TO BILGE WATER EMULSIONS FOR *IN SITU* CHARACTERIZATION

This paper has been previously published as: Church, J., Paynter, D.M., and Lee, W.H. (2016) In Situ Characterization of Oil-in-Water Emulsions Stabilized by Surfactant and Salt Using Microsensor, *Langmuir*, 7, 338-348.

Abstract

Chemically stabilized emulsions are difficult to break because of micelle stability. Many physical and chemical processes have been used for emulsion breaking/separation; however, most operational parameters are based on empirical data and bulk analysis. A multi-scale understanding of emulsions is required before these processes can advance further. This study utilized needle-type microsensors and confocal laser scanning microscopy (CLSM) for characterizing simulated bilgewater emulsions with different type of surfactants (Triton X-100 and sodium dodecyl sulfate [SDS]) under various NaCl concentrations at micro-scale. Using microsensors, a diffusion process was clearly visualized across the oil/water interface which appears to be related to emulsion formation kinetics and mass transfer. While emulsion stability decreased with NaCl concentrations, SDS (anionic surfactant) is more likely to form emulsion as salinity increases, requiring more salinity to coalesce SDS emulsions than Triton X-100 (nonionic surfactant) emulsions. Triton X-100 emulsions showed the potential to exhibit particle stabilized emulsions with NaCl concentration below $10^{-2.5}$ M. The research demonstrated that the use of nonionic surfactant allows better oil-in-water separation than anionic surfactant. Significant pH changes of emulsions from unknown additives have implications when operating pH sensitive emulsion breaking/separation processes (e.g. electrocoagulation).

Introduction

Bilgewater is a regulated mixture of seawater and any water contaminated with oils, solvents, surfactants, and particulate matter that accumulates in the lowest part of a ship (Copeland 2007, Kajitvichyanukul et al. 2006). Free or suspended oils (i.e. mechanical emulsions) can be readily separated from the water phase by simple physical processes (e.g. skimming); however, chemically stabilized oil-in-water emulsions formed in bilgewater (i.e. chemical emulsions) are notoriously difficult to break which may result in non-compliance with existing ocean discharge regulations (< 15 ppm of oil concentration)(IMO 1973, Smookler et al. 1977). Therefore, it is critical to develop innovative methods for breaking emulsions and thus separating oil from water to ensure proper on-board bilgewater treatment. Unlike mechanical emulsions, chemical emulsions are capable of remaining in a stable homogeneous state for an indefinite period of time (Ibanez et al. 1995, Wilde 2000). Many oil/water separators and pre- or post-unit processes have been developed and used for shipboard treatment of bilgewater emulsions. Among them, gravity based oil-water separators (OWS) have been used for decades to treat unstable mechanical emulsions, while newer post-treatment technologies like membrane filtration have been implemented for emulsion removal (Karakulski et al. 1995, Koss 1996). Pretreatment processes like electrocoagulation (EC) have also attracted attention as a method for emulsion breaking through *in situ* coagulant production as opposed to the addition of chemical agents used in traditional coagulation, which requires a large volume of chemical storage (Bensadok et al. 2008, Canizares et al. 2008, Mollah et al. 2004, Mollah et al. 2001, Mouedhen et al. 2008). These technologies are effective, but still rely on empirically determined design parameters. A better understanding of oil/water emulsion formation, stability, and breaking in shipboard environment will assist the development of technologies that can mitigate the

formation and undesired consequences of shipboard emulsions. However, our understanding of oil-in-water emulsion stability and chemical properties is still incomplete and *in situ* characterization of interface of oil/water emulsion has been challenging due to lack of experimental tools.

The objective of this study was to evaluate effects of surfactant and salinity on the chemically formed oil-water-emulsion stability of simulated bilgewater using microprofiling characterization, confocal laser scanning microscopy (CLSM) analysis, and traditional characterization methods such as contact angle and interfacial surface tension. In particular, a needle-type microsensor as a novel and unique tool for *in situ* emulsion characterization was applied to investigate the relationship between the transports of chemical compounds across oil/water interfaces and the stability of emulsions, which has not been applied in traditional methods. The adaption of needle-type electrochemical microsensors to environmental systems has transformed how we study biofilms, mats, and sediments (Lee et al. 2011a, Lee et al. 2011b). With such small tip diameters (3–20 μm), they can be used to perform measurements at the microscale which can provide mechanistic information that cannot be obtained from bulk-scale measurements.

Here, we present a systemic evaluation of simulated bilgewater to find relationships between microprofiling characterization, CLSM analysis and traditional characterization methods (contact angle and interfacial surface tension) for better understanding of emulsions stability. Two different types of surfactant (Triton X-100 as non-ionic surfactant and sodium dodecyl sulfate [SDS] as anionic surfactant) were tested for emulsion stability with various NaCl concentrations. The pH, oxidation-reduction potentials (ORP), and dissolved oxygen (DO) microprofiling characterization using microsensors provided information on the transport of

chemical compounds across the oil water interface while contact angle, interfacial tension, and CLSM evaluation gave information on physical properties and morphology. Overall, this multiscale (macro- and micro-) study provided meaningful information on bilgewater micelle formation and associated emulsion stability which may lead to developing improved solutions for effective emulsion treatment.

Materials and Methods

Preparation of Emulsions.

Emulsion samples were prepared using Navy Standard Bilge Mix (NSBM) #4 which was provided by the Naval Surface Warfare Center Carderock Division (NSWCCD) (West Bethesda, MD, USA). Two different surfactants were selected as representative anionic and ionic surfactants with well-studied properties (Triton X-100 as a nonionic surfactant and SDS as an anionic surfactant). While Triton X-100 is not typically used in consumer cleaning products, SDS and Triton X-100 have similar molecular and chemical properties to surfactants found shipboard. Emulsion samples with various salinities (10^{-4} –1M NaCl at $10^{0.5}$ intervals) were also tested to represent a range of bilgewater conditions. Two different types of emulsions were prepared: microemulsion and macroemulsion. Microemulsions were prepared by mixing 1,000 ppm (0.1%) NSBM #4 and 100 ppm Triton X-100 or SDS in 40 mL of Mili-Q water for 2 minutes at 35,000 rpm using a homogenizer (Omni Tissue Master, Model 125, 10 mm generator probe) followed by 10 minutes of sonication (40 kHz, Branson Branson Cleaner, Model B200) and a filtration step using a 0.22 μ m membrane (Millex GP PES, SLGP033RS). Macroemulsion samples were prepared using the same procedures, but with 10,000 ppm (1%) NSBM #4 and without filtration. Microemulsion samples were homogenous, not containing an oil layer as shown in Supporting Information (SI) Figure S1. As microemulsion does not represent

bilgewater emulsion, macroemulsion samples were mainly prepared and evaluated in this study.

Characterization of Bulk Properties.

Contact Angle and Interfacial Surface Tension.

Contact angles of various surfactant solutions in NSBM #4 were measured using a goniometer (Model 100-00, Rame-hart Instrument Co. Succasunna, NJ, USA). The liquid phase varied in surfactant type (100 ppm SDS and 100 ppm Triton X-100) and salinity (10^{-4} , $10^{-3.5}$, 10^{-3} , $10^{-2.5}$, 10^{-2} , $10^{-1.5}$, 10^{-1} , $10^{-0.5}$, and 1M NaCl). The solid surface was a flat quartz substrate which was cleaned using soapy water, soaked with 2M NaOH for 30 minutes and rinsed with deionized (DI) water between each measurement. A 5 μ L drop of prepared surfactant solution sample was immersed in NSBM #4, placed on the quartz solid substrate and illuminated from one side, while a camera recorded the image on the opposite side. The image was then analyzed by software (DROPimage Advanced, Rame-hart instrument Co., Succasunna, NJ, USA) to determine contact angle. The interfacial tension was measured the pendant drop method (Pichot 2010). For this method, a 5 μ L liquid drop (i.e. a mixture of surfactant and NaCl solution) was suspended in NSBM #4 at hydromechanical equilibrium (a balance between gravity, buoyant, and surface forces) and interfacial tension was calculated by a drop shape analysis program (DROPimage Advanced, Rame-hart instrument Co., Succasunna, NJ, USA). The interfacial tensions of oil-in-water samples (i.e. an oil drop [NSBM #4] in a surfactant solution) were also measured for reference purpose. Since NSBM #4 is less dense than the surfactant solutions tested, in this case, a “U” shaped needle (Cat. No. 100-10-13, Rame-Hart instrument co., Succasunna, NJ, USA) was used for oil-in-water tests.

CLSM Analysis of Simulated Bilgewater Emulsions.

CLSM analysis was performed using Leica TCS SP8 (Leica Microsystems, Buffalo Grove, IL, USA) with an argon laser operating at 488 nm excitation wavelength and emission was detected between 507 and 574 nm. The samples were prepared using 1% NSBM #4 dyed with 1 mg/L Nile red (Cat. No.72485, Sigma Aldrich, Milwaukee, WI, USA) and 100 ppm SDS or Triton X-100 surfactants. Fluorescence of oil (NSBM #4) without the use of Nile Red was also observed under UV light (Figure S2, SI) and with an excitation wavelength of 488 nm using CLSM; however, the Nile red was still used to improve the intensity of the emission spectrum which helped develop high quality images of the fast-moving emulsions (Schuster 1987). Furthermore, we found that the Triton X-100 fluoresces with an excitation wavelength of 512 nm and an emission filter from 494 to 591 nm. This was used to visualize the aqueous layer. To ensure that CLSM microscopic images represent the morphology of emulsion samples in a selected different location along the column depth, the outer rim of the pipette tip at every collection was cleaned with a Kimwipes[®] and 50 μ L of the sample was expelled through the pipette tip before applying the sample to a microscope slide for analysis. The changes in emulsion size were also quantitatively analyzed using the CLSM processing software (LAS AF lite, Leica).

In Situ Emulsion Characterization Using Microsensors.

pH, ORP, and DO microprofiles were measured using microsensors (10 μ m tip size, UNISENSE A/S, Denmark). For the calibration of ORP microsensors, the phosphate buffer solution (5 mM) saturated with quinhydrone at pH 7 and pH 4 was used which equates to redox potentials of 462 mV and 285 mV, respectively (Lee et al. 2011a). pH microsensors were calibrated using pH 4, 7, and 10 standard buffer solutions (Fisher Scientific). DO microsensors

were calibrated in respective oxygen saturated (21% DO, 8.6 mg O₂/L at 23°C) surfactant solution (100 ppm Triton X-100 or SDS) and the same solution under nitrogen bubbling (0% DO). The microsensors were calibrated before and after each profile for validating the measured microprofiles (Figure S3, SI). The performance evaluation of pH, ORP, and DO microsensors is well described elsewhere (Lewandowski and Beyenal 2013).

For microprofiling, emulsion samples were placed in a microprofile chamber (50 ml self-standing tube, EW-06344-25, Cole Parmer) which was held in place using a clamp (Figure S4, SI). Positioning and movement of the microsensor tip in the sample was accomplished using a three-dimension (3D) micromanipulator (UNISENSE A/S, Denmark) and observed using a stereomicroscope with a CCD camera (World Precision Instruments, Sarasota, FL, USA). The Ag/AgCl reference electrode (MI-401, Microelectrodes Inc., Bedford, NH, USA) was positioned in the emulsion layer. Microsensor electrode signal was measured with a multimeter (UNISENSE A/S, Denmark) and the experiments were performed in a Faraday cage (81-334-04, Technical Manufacturing Co. Peabody, MA) to minimize electrical interference. Microprofile measurements were taken every 100 µm with 5, 60, and 90 seconds of wait time between each measurement for DO, pH, and ORP respectively, for signal stabilization depending on emulsion samples. Four replicate profiles were taken for each parameter; two in the direction of top to bottom and two from bottom to top. The microprofiles shown in this paper are the averaged values of these replicates. Microprofiles were taken from the point at which the sensor picks up a stable electrical signal (mV or pA) by contact with the oil to the bottom direction perpendicularly.

Results and Discussion

Visual Observations

Visual observation under different surfactant and salinity levels showed that both NaCl and surfactant type had a significant effect on oil-in-water emulsion stability. After preparation of various emulsion samples with different surfactants and NaCl concentrations, the stability of emulsion samples was observed over 10 days (Figure 4-1). Emulsion samples appeared homogeneous immediately after preparation; however, the sample with Triton X-100 and 0.1 M NaCl showed evidence of coalescence after only a few minutes (Day 1). After 24 hrs (Day 2), samples with 0.1 M NaCl exhibited a clear oil layer for both emulsion samples while the samples without NaCl showed only limited coalescence of oil. Similar trends were observed on Days 5 and 10 when emulsion samples with NaCl displaying more coalescence compared to samples without NaCl. The results clearly showed that emulsion stability decreases with NaCl concentrations over time. In addition, SDS (i.e. charged surfactant) stabilized emulsions seemed more susceptible to changes in salinity. In general, increased NaCl concentrations led to more rapid coalescence and these visual observations were in agreement with previous studies (AHMED et al. 1999, Bourrel et al. 1980).

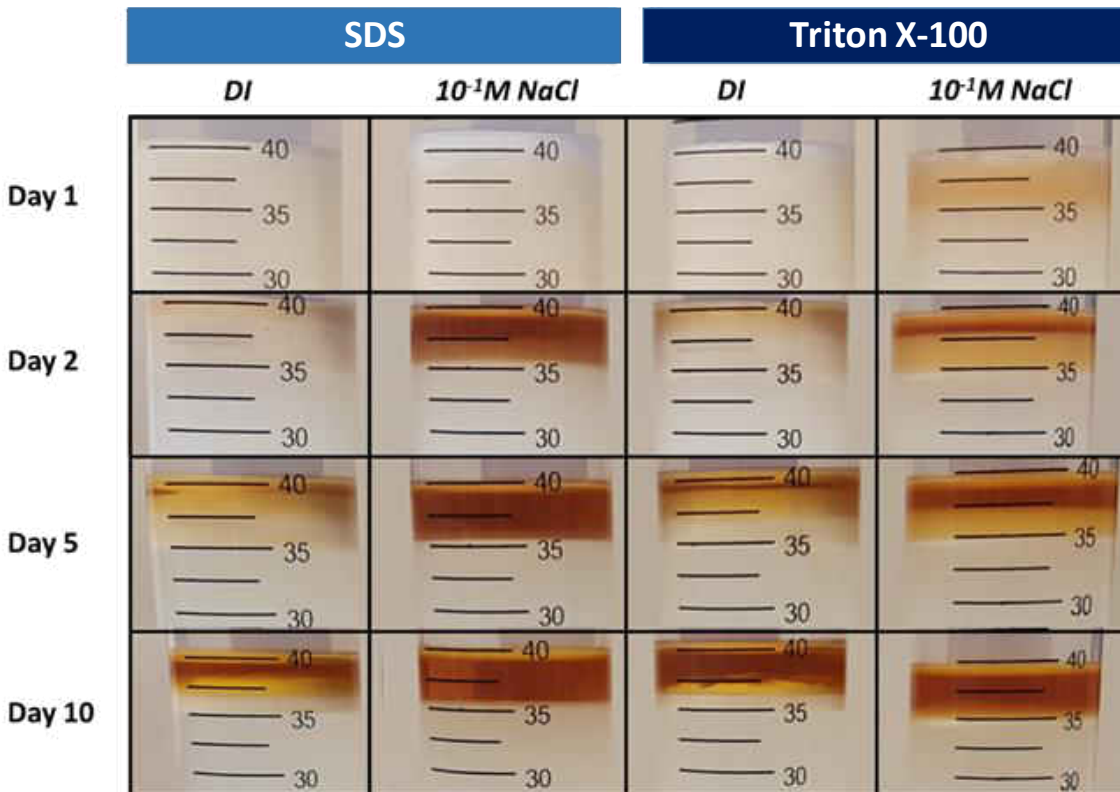


Figure 4- 1. Visual observation of various oil-in-water emulsion samples over time. The surfactant concentration of 100 ppm was used to prepare the macroemulsion samples.

Contact Angle

Contact angles of other samples (100 ppm SDS and DI water only) were relatively constant with time. The contact angle of the control (DI water without surfactant) was in the range between 162 ° and 172 ° with different NaCl concentrations (10⁻⁴–1 M) (Fig. 4-2(a)). Details on contact angle measurement of surfactant water are provided in the Supporting Information (Fig. B5 and B6). Contact angles of the SDS samples were in the range between 166 ° and 155 ° which are similar with DI + NaCl solution only (no surfactant) and were not affected by salinity. However, the Triton X-100 solution had the lowest contact angles, particularly at low NaCl concentrations. The contact angle for Triton X-100 samples increases from 95.9 ° to 120 ° with increased NaCl concentrations from 10⁻⁴ to 10^{-1.5} M probably due to increased ion strength. Further increases of the NaCl concentration do not modify the contact angle, remaining constant

around 120° from 10^{-1.5}–1 M NaCl. The changes of contact angle depending on salinity may be due to modification of the wettability of the glass by the increase of NaCl concentrations.

The balance of forces of a wet droplet (DI + surfactant + NaCl) can be described by the Young equation.(Kwok and Neumann 1999) For water-oil-glass systems, the equation can be written as follows:

$$\gamma_{ws} + \gamma_{ow}\cos\theta - \gamma_{os} = 0 \quad (4-1)$$

where γ_{ws} is the water-solid (W/S) interfacial tension, γ_{ow} is the oil-water (O/W) interfacial tension and γ_{os} is the oil-solid (O/S) interfacial tension. Since the contact angles of Triton X-100 samples were approximately 90° at NaCl concentrations below 10^{-2.5} M, $\gamma_{ow}\cos\theta$ is negligible (≈ 0), indicating that W/S and O/S interfacial tensions are similar. As NaCl concentration increases, W/S interfacial tension also increases which can be shown by rearranging Young's equation:

$$\theta = \cos^{-1}\left(\frac{\gamma_{os}-\gamma_{ws}}{\gamma_{ow}}\right) = \arccos\left(\frac{\gamma_{os}-\gamma_{ws}}{\gamma_{ow}}\right) \quad (4-2)$$

where $-1 \leq \left(\frac{\gamma_{os}-\gamma_{ws}}{\gamma_{ow}}\right) \leq 0$. The numerator should be negative ($\gamma_{os} < \gamma_{ws}$) given that contact angle is higher than 90° for all tested samples (Fig. 4-2(a)) and differences in O/W interfacial tension (γ_{ow}) were relatively small with changes in NaCl concentration (Fig. 4-2(b)). Because measured contact angles are not close to 90° where oil-particle interfacial tension (γ_{os}) and water-particle interfacial tension (γ_{ws}) are equal, these sample are unlikely form particle stabilized emulsions.(Pichot 2010) However, the contact angles for Triton X-100 samples, ranged 95.9 to 120° and has the potential to exhibit particle stabilized emulsions with NaCl concentration below 10^{-2.5} M. The wetting of particles by water and oil is a key parameter for determining the potential of particle stabilized emulsions.(Levine et al. 1989, Pichot 2010, Velev and Lenhoff 2000) The particle stabilized emulsions, also called Pickering emulsions, tends to more stable than emulsions stabilized with surfactants or silica (quartz in this test) stabilized

emulsions.(Levine et al. 1989, Velev and Lenhoff 2000) Therefore, the addition of NaCl is expected to decrease the emulsion stability in bilge water containing nonionic surfactants (i.e. Triton X-100).

Interfacial Surface Tension

The primary role of a surfactant is to reduce interfacial surface tension to facilitate the droplet break-up and prevent re-coalescence (Walstra 1993). Interfacial surface tension is directly related to the energy needed for emulsion formation (Gopal 1968, McClements 2015, Walstra 1993). Thus, lower surface tension means less energy is required for emulsion formation and results in smaller droplets and more stable emulsions (Lucassen-Reynders and Kuijpers 1992). The results for water-in-oil interfacial tension measurements are shown in Fig. 4-2(b). The interfacial surface tension of the control (no surfactant) was $27.4 \text{ mN}\cdot\text{m}^{-1}$ at 10^{-4} M NaCl and the values were relatively constant in the range from 23.3 to $32.3 \text{ mN}\cdot\text{m}^{-1}$ regardless of NaCl concentrations, confirming that without surfactants considerable energy is needed to produce an emulsion.

In the presence of surfactant, interfacial tensions at 10^{-4} M NaCl reduced to 6.5 and $2.1 \text{ mN}\cdot\text{m}^{-1}$ for SDS and Triton X-100, respectively (Fig. 4-2(b)). The interfacial tension of aqueous SDS micelles showed a decrease with NaCl concentration from initial 6.8 to below $1.6 \text{ mN}\cdot\text{m}^{-1}$ after NaCl concentration exceeded $10^{-1.5} \text{ M}$, showing that water containing SDS is more likely to form emulsion as salinity increases. For Triton X-100, the surface tension also decreased but not significantly with NaCl concentration from 3.3 to $2.1 \text{ mN}\cdot\text{m}^{-1}$. The results showed more potential for emulsion formation in high salinity bilgewater. However, the visual observation also demonstrated that emulsion with high concentrations of NaCl tend to be less stable (Fig. 4-1). This could be the result of “salting-out” where increased salinity causes the interactions of the

emulsion stabilizing surfactants with water to decrease and reduce emulsion stability (Martínez-Palou et al. 2013, Zolfaghari et al. 2016).

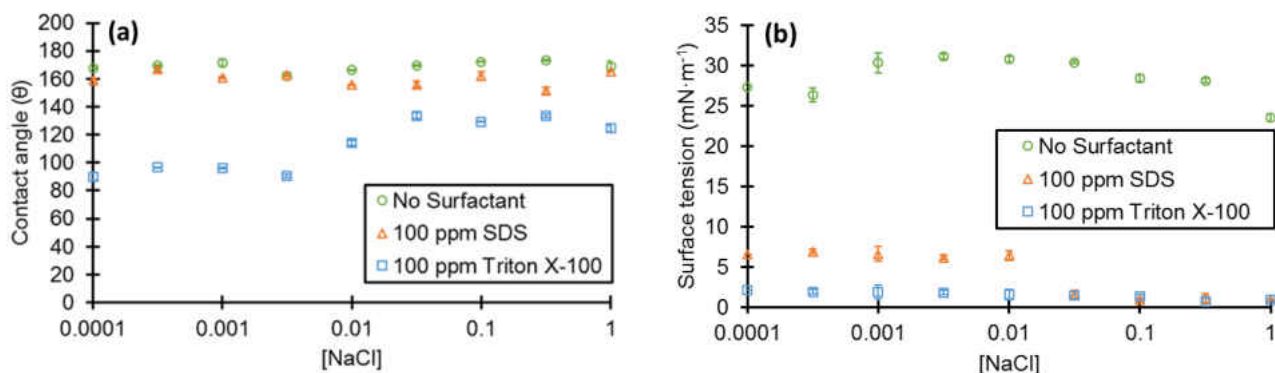


Figure 4- 2. The effects of NaCl concentrations on (a) the static contact angle of water (DI water only, 100 ppm SDS, or Triton X-100) in oil (NSBM #4) and (b) the surface tension of water-in-oil pendant drops. Temp. was constant at 24°C. Quartz was used as a substrate for contact angle measurements. Waiting time was 60 s for each reading. Interfacial tension of either water-in-oil or oil-in-water showed similar trends.

CLSM Analysis

CLSM micrographs for various emulsion samples are shown in Fig. 4-3. The emulsion sizes increased with NaCl concentration in SDS emulsions (8.6 μm at 10⁻⁴ M to 18.1 μm at 1 M), indicating emulsions tend to coalesce with increasing NaCl, while Triton X-100 emulsions decreased in size with increased NaCl concentrations (13.0 μm at 10⁻⁴ M to 7.5 μm at 1 M) (Fig. B7). However, fewer emulsion droplets were observed compared to SDS even at the same depth, indicating that Triton X-100 emulsions are less stable and coalesce faster than SDS emulsions with NaCl concentrations. It appears that more NaCl amounts were required to coalesce SDS emulsions than Triton X-100 emulsions when compared with similar emulsion sizes (e.g. 12.2 μm at 10⁻¹ M NaCl for SDS and 13.2 μm at 10⁻³ M NaCl for Triton X-100) (Fig. 4-3). After 24 hours, changes in emulsion size decreased significantly and the emulsion size was in the similar range between 1.6–3.9 μm for both SDS and Triton X-100 regardless of NaCl concentrations

(Fig. B7). However, CLSM images clearly showed that Triton X-100 emulsion droplets were almost removed in the presence of high NaCl concentrations (e.g. 0.1–1 M NaCl) and only small number of droplets were found after 24 hours of hydraulic retention time (HRT) (Fig 4-3). In general, less individual droplets, due to coalescence, are expected with time, (KATSUKI et al. 2015, Leal-Calderon et al. 2007, MITA et al. 1973) however, due to differences in density between oil and water, oil droplets tend to float to the top of the samples and form a layer of emulsion droplets in a process known as creaming (Fig. B8).(2013)

The CLSM investigation implies that 1) NaCl facilitates emulsion coalescence with time, 2) the use of non-ionic surfactant allows better oil-in-water emulsion separation than anionic surfactant in the presence of NaCl (>0.1 M NaCl), and 3) emulsion size only does not provide information on the oil stability and it should be correlated with the density of emulsion droplets. For example, the small droplet sizes for Triton X-100 emulsions in 0.1 M NaCl would typically be expected to result in stable emulsions; however, the sample ended up being the most unstable at initial time 0 hr (Day 1) (Fig 4-1).

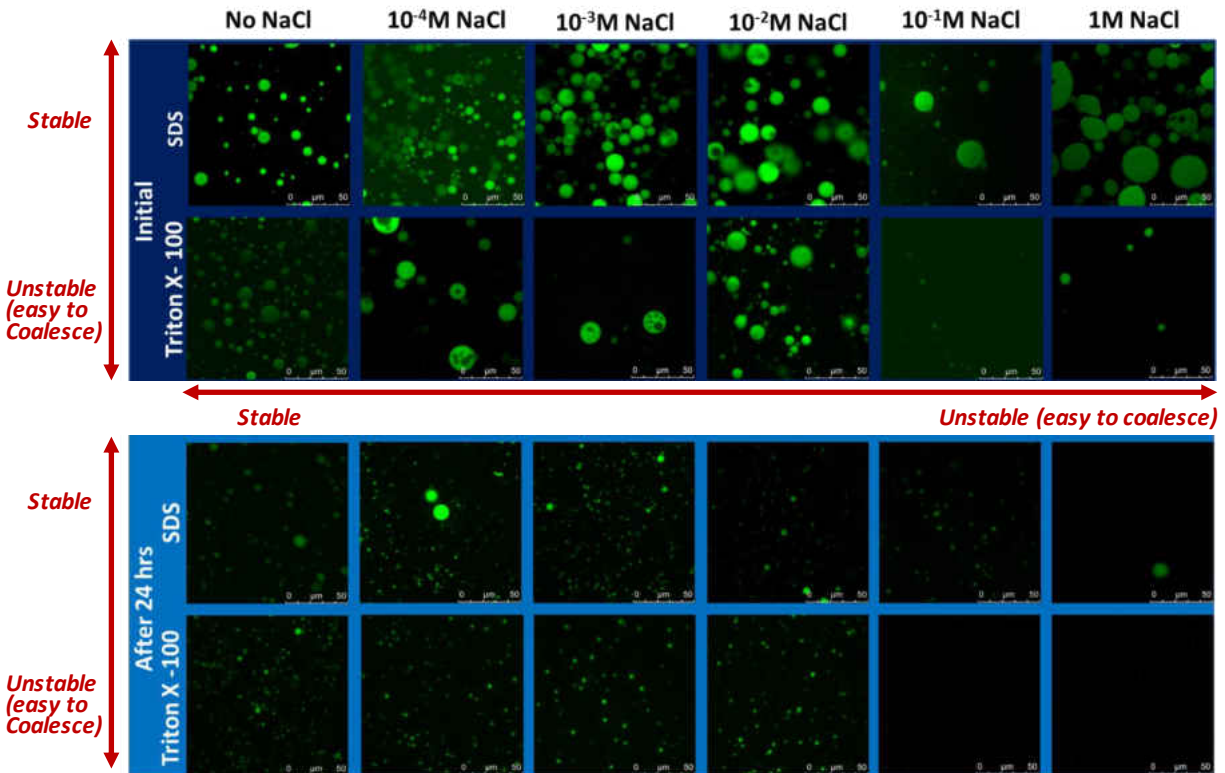


Figure 4- 3. CLSM images of emulsions prepared with 100 ppm SDS or 100 ppm Triton X-100 at various salinities at the initial and 24-hour interval. All samples were taken at the middle of the emulsion layer.

Chemical Microprofiles of Oil Water Interfaces

Microsensor performance validation in oil-water mixture

With the exception of microemulsions, emulsions are thermodynamically unstable and will only remain as a dispersion for a finite period (Wilde 2000). Understanding the role of oil/water (or water/oil) interfaces on the formation and stability of emulsions have been well studied in recent years (Beattie and Djerdjev 2004, Binks et al. 2000, Friberg et al. 1976, Walstra 1993); however, component interactions across the interface has yet to be explored. In this study, a needle-type microsensor was used to characterize *in situ* interfacial reactions between oil and water under various simulated bilgewater emulsions. As this is the first to apply electrochemical sensor to oil-water mixtures, a well-known DO microsensor (Lee et al. 2011a, Lewandowski and

Beyenal 2013) was tested to validate the electrochemical microsensor performance in oil-water mixtures under various DO conditions and DO profiles clearly showed a diffusion of DO from the oil phase (21%) to the water phase (0%) with the oxygen scavenger. Details on microsensor performance validation are provided in Appendix B (Fig. B9).

The effect of unknown oil additives on the pH of the surfactant solutions

During the microsensor profiling, unexpected pH changes across the interface between oil and water were observed. Fig. 4-4 shows the pH gradient across the interface separating the dispersed and continuous phases. pH was measured at 1 minute after adding NSBM #4 or mineral oil. There was a clear increase of pH from 7.3 (bulk) to 8.3 (interface) when 100 ppm SDS solution is the continuous phase (Fig 4-4(a)). For Triton X-100 as a continuous phase, a pH increase from 7.7 (bulk) to 8.3 (interface) was observed (Fig. 4-4(a)). The increase in pH for both surfactant solution at the interface is hypothesized to be the result of an unknown oil additive that may be partially miscible in water and be diffusing into the continuous phase. To prove this hypothesis, pH microprofiles were measured across an interface where mineral oil was used as a control of the dispersed phase. Because mineral oil is a pure oil which has no additive, there should be no pH changes throughout the surfactant solutions including the interfacial surface (Fig. 4-4(b)). The initial pH in Triton X-100 and SDS (100 ppm) was 6.7 and 6.5, respectively. With the addition of NSBM #4, the bulk pH was increased 7.7 and 7.3, respectively, indicating that the unknown additive is a high pH alkaline chemical. Fig 4-4(a) shows that the oil additive would have trouble diffusing through the negatively charged SDS surfactant layer with a larger pH gradient, while it could easily pass through the nonionic surfactant layer (i.e. Triton X-100). The finding here implies that oil additives and surfactant type can affect the oil-in-water emulsion pH which would consequently affect the micelle stability and the performance of

emulsion breaking/separation processes such as electrocoagulation.

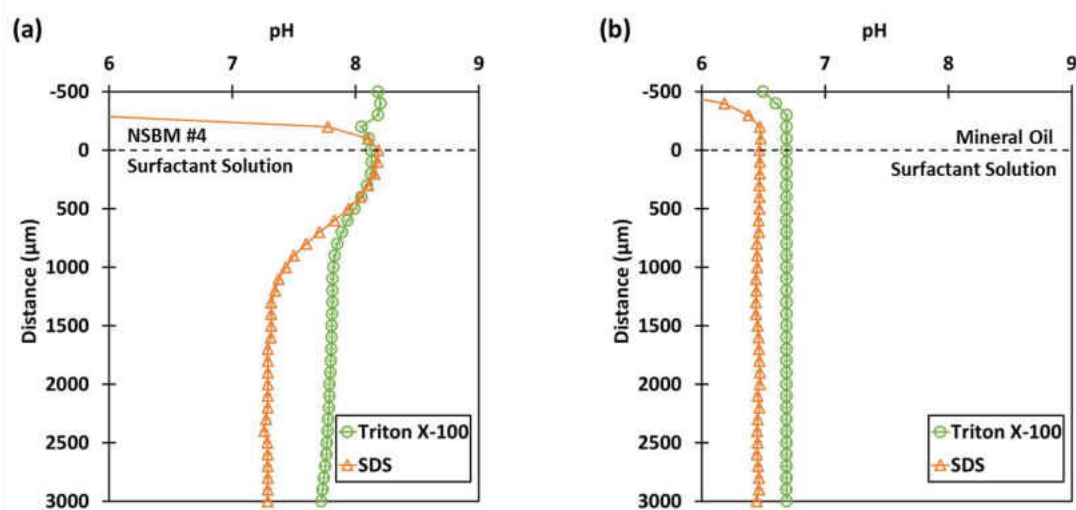


Figure 4- 4. Spatial pH changes in (a) a NSBM #4 and surfactant sample (100 ppm Triton X-100 vs. SDS) and (b) a mineral oil and surfactant sample. 0 μm represents the oil-water interface. DI water only was used to prepare surfactant solution.

Microsensor oil-in-water emulsion characterization

The chemical microprofiles including DO, pH, and ORP profiles were successfully measured using microsensors for *in situ* characterization of emulsion stability and chemical properties at the micro-scale. All measured microprofiles were reproducible with several consecutive measurements in oil-water emulsion mixtures. Microprofiling emulsion samples exhibited changes with salinity and surfactant type. Fig. 4-5(a) and (b) and Fig. 4-6(a) and (b) show the spatio-temporal pH changes of the emulsion samples with Triton X-100 and SDS surfactants in the absence (DI water only) and presence of NaCl (0.1 M), respectively. For all conditions without NaCl, pH increased over time probably due to the diffusion of an unknown oil additive over time; however, this pH increase was more apparent in SDS emulsions. It seems that the presence of salinity increased the mass transfer of the oil additive; however, the rate of pH increase in the bulk slowed with increasing salinity. This is due to the increased diameter and decreased surface area of SDS emulsions with increasing salinity (Fig. 4-3). pHs in the bulk of

SDS samples were 8.0 with no salinity and 7.3 with 0.1 M NaCl at time 0 hr, respectively, while pHs in the bulk of Triton X-100 samples were 8.5 with no salinity and 9.0 with 0.1 M NaCl at time 0 hr. Emulsions which were stabilized with a nonionic surfactant (i.e. Triton X-100) showed higher pH compared to the emulsions with an anionic surfactant (i.e. SDS). Given that the original pH of Triton X-100 solution (100 ppm) is 6.7, this indicates that Triton X-100 would be susceptible to the less stable emulsion formation with evenly well-distributed pHs with time and according to the depth (Fig. 4-6(a) and (b)) compared to SDS (Fig. 4-5(a) and (b)). The pH difference in the bulk depending on surfactant and salinity implies that the performance of pH sensitive emulsion breaking processes like electrocoagulation may be affected by surfactant, salinity, and unknown oil additives in the bilgewater to be treated. pH microprofiles with SDS (Fig. 4-5(a) and (b)) showed that pH gradient at oil-emulsion interface of SDS + DI only emulsions was smaller than SDS + DI + 0.1M NaCl solution where larger pH gradients were observed. It appears that the addition of NaCl developed larger pH gradients at the interface, indicating less stable emulsion.

DO concentration microprofiles also implies decreased stability with the addition of NaCl (Fig. 4-5(c) and (d) and Fig. 4-6(c) and (d)). While there was little change in DO concentration along with depth (~ 1 cm), there was variability in DO concentration with time. The initial DO concentration of SDS emulsions with 10^{-1} M NaCl was 13.5 mg O₂/L, while the DO concentration without NaCl was 12.3 mg O₂/L at time 0 hr. This is because emulsions prepared using NaCl had more tendencies to foam in SDS samples which would result in higher DO concentrations, leading to cloudier layer and more unstable emulsions. After 24 hrs, DO concentration decreased by only 0.6 mg O₂/L in the emulsion sample without NaCl, while the DO decreased by 2.7 mg O₂/L in the presence of NaCl. The rate of DO decrease is faster with

NaCl (approx. $3 \text{ mg L}^{-1} \text{ day}^{-1}$ with NaCl vs. $1 \text{ mg L}^{-1} \text{ day}^{-1}$ with no salinity), showing that NaCl decreases the emulsion stability. Triton X-100 emulsions also showed a similar trend with SDS emulsions and the NaCl addition decreased the emulsions stability which was shown by DO concentration decreases over time. Variability in DO concentration with depth was less in emulsions with NaCl. The visual stability of SDS emulsions (Fig. 4-1) agreed with the DO concentration profiles. More stable emulsions (e.g. SDS + DI) appeared to retain high DO concentrations longer than less stable emulsions (e.g. SDS + 0.1 M NaCl).

Another interesting observation from DO concentration microprofiles was the effect of NaCl on the DO concentration gradient changes at the oil-emulsion interface over time. Regardless of surfactant type, preparation of emulsion (mixing in open air) resulted in supersaturated oxygen concentration in emulsion layer ($12\text{--}13.5 \text{ mg O}_2/\text{L}$ regardless of NaCl addition). However, it seems that NaCl plays an important role in trapping and transferring oxygen between emulsion and oil layer. Without NaCl, the oxygen was trapped in emulsion with slow diffusion to oil layer (Fig 4-5(c) and 4-6(c)). This generated diffusion boundary layer (DBL) of $2,000 \text{ }\mu\text{m}$ thickness and the DBL thickness was decreased along with decrease of DO concentration in emulsion layer with time, indicating that oxygen in emulsion is slowly moving out from the system. However, the presence of NaCl increased oxygen transfer from emulsion to oil layer, resulting in no DBL even at initial time (Fig 4-5(d) and 4-6(d)). The DO profiles provide better scientific fundamentals behind the visual observation in Fig. 4-1.

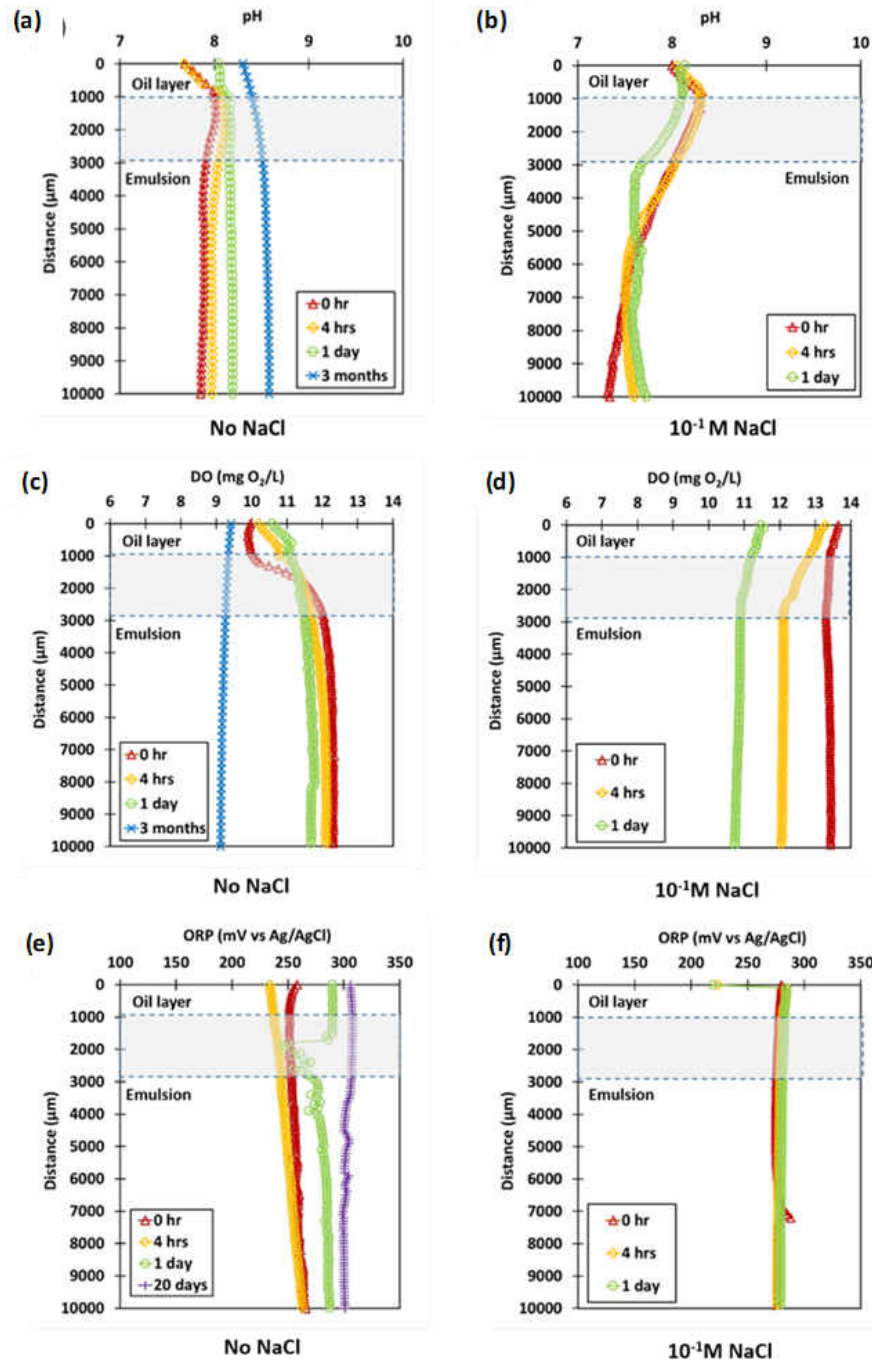


Figure 4- 5. The effects of anionic surfactant and salinity on the spatial and temporal pH, DO, and ORP changes in oil-in-water emulsion (1% NSBM #4 + SDS). (a) pH profiles without NaCl, (b) pH profiles with 0.1M NaCl, (c) DO profiles without NaCl, (d) DO profiles with 0.1M NaCl, (e) ORP profiles without NaCl, and (f) pH profiles with 0.1M NaCl. 0 μm represents the point at which the sensor signal was obtained by contact with the oil. The interface between oil and emulsion was changed over time within the grey area in each profile.

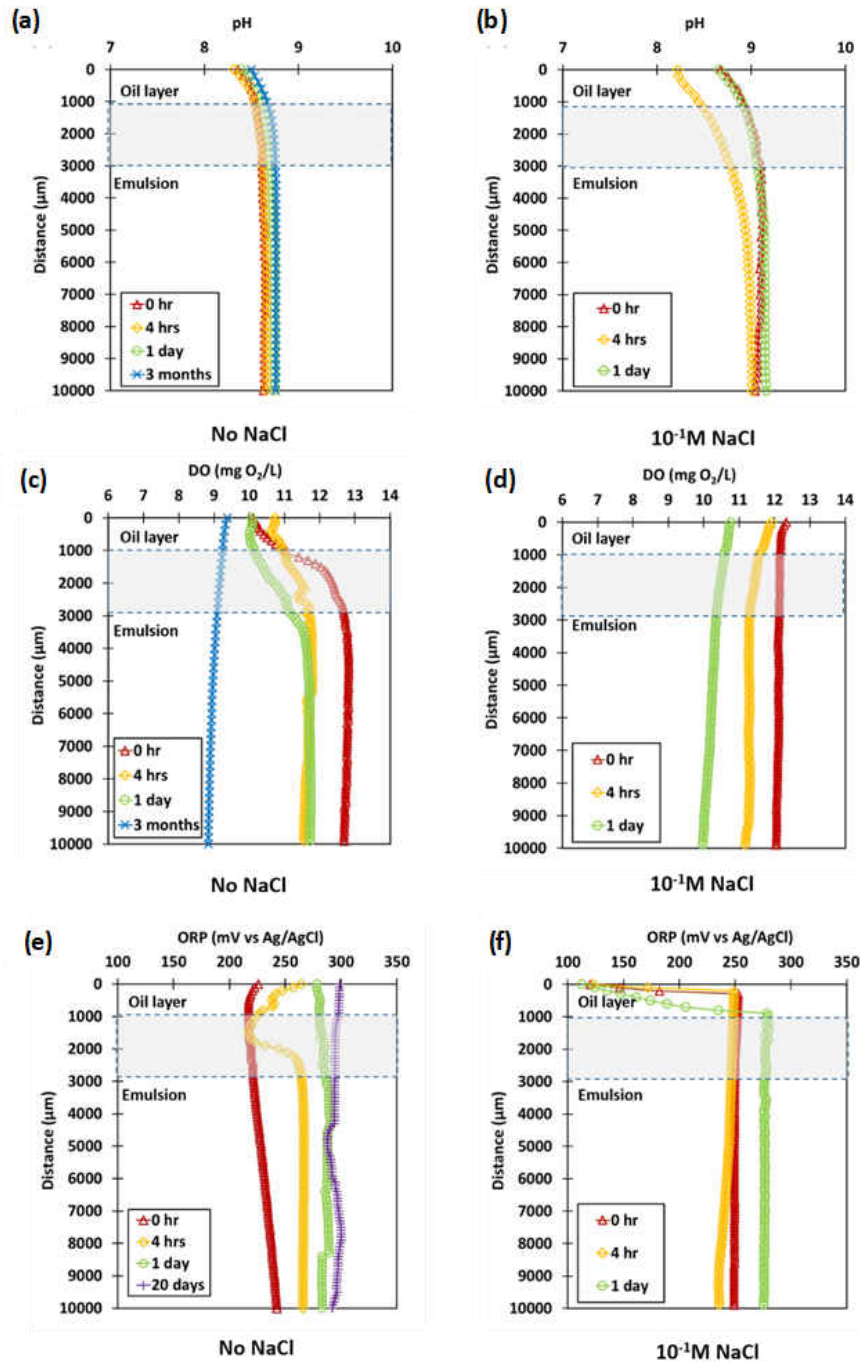


Figure 4- 6. The effects of non-ionic surfactant and salinity on the spatial and temporal pH, DO, and ORP changes in oil-in-water emulsion (1% NSBM #4 + Triton X-100). (a) pH profiles without NaCl, (b) pH profiles with 0.1M NaCl, (c) DO profiles without NaCl, (d) DO profiles with 0.1M NaCl, (e) ORP profiles without NaCl, and (f) pH profiles with 0.1M NaCl. 0 μm represents the point at which the sensor signal was obtained by contact with the oil. The interface between oil and emulsion was changed over time within the grey area in each profile.

ORP microprofiles of the emulsions samples are shown in Fig. 4-5(e) and (f) for SDS emulsions and Fig. 4-6(e) and (f) for Triton X-100. ORP showed less variability regardless of surfactants with depth in emulsions prepared with NaCl. This is likely the result of increased conductivity from NaCl addition. ORP microprofiles of emulsions stabilized with SDS showed no increase in ORP over time or depth with the addition of NaCl (Fig. 4-5(f)). The ORP microprofiles of SDS emulsion samples without NaCl (Fig. 4-5(e)) were continuously changed with longer sensor detection time, while ORP microprofiles with the addition of NaCl showed rapid electric response and thus a more stable signal. In Triton X-100 emulsions without NaCl, a much greater variability with depth and time was observed (Fig. 4-6(e)) than the emulsions with NaCl. An unknown sharp decrease in ORP within the oil layer was observed in emulsions stabilized with both types of surfactants (SDS and Triton X-100) with NaCl.

Effect of Mass Transport on the Stability of Simulated Bilge water Emulsions

The effect of solute transport across oil/water interface has been shown to affect emulsion stability. A theoretical study by Sternling and Scriven (1959) recognized Marangoni-Gibbs instabilities, where the mass transfer occurs along an interface between two different liquid phases, as one of the major causes of spontaneous emulsification and that the direction of solute transfer can stabilize or destabilize an emulsion. Further works by Ivanov (1987) and Dimitrova (1988) concluded that the presence of a solute (acetic acid) in the drop phase (oil) decreased the life time of emulsion films while solute dissolved in the continuous phase (bulk water) produced more stable films. While these studies laid the theoretical groundwork on effect of mass transport on emulsion stability; more elaborate analyses are needed for a decisive test of the theory. The use of microsensors in this study allows for a direct quantitative analysis on the effect of mass transport on emulsion stability.

The pH gradient across the oil/water interface in Figures 4-4, 4-5, and 4-6 represents the transport of an additive (unknown) from the oil phase to the continuous phase. Here, it is observed that increased mass transport across the oil/water interface leads to decreased emulsions stability. For example, pH microprofiles of SDS stabilized emulsions with and without 0.1M NaCl show that higher salinity increases the flux of the additive, from 0.06 pH units/mm to 0.23 pH units/mm (Fig. 4-5), which in turn decreases stability due to Marangoni instabilities (Fig. 4-1). Evidence of Marangoni instability in SDS emulsions is also found in the surface tension experiments where decreased surface tension (Fig. 4-2) was expected to increased mass transfer (Fig. 4-5) and decrease emulsion stability. Nonionic surfactant (Triton X-100) stabilized emulsions did not display a flux of solute across the oil water interface and therefore does not appear to be affected by Marangoni instabilities. This is because mass transfer of the additive occurred during the mechanical emulsifying process. Fig. 4-6 shows there is no additive flux across the interface of Triton X-100 emulsions.

Overall, microsensor characterization of emulsions proved to be a useful tool for monitoring mass transfer across and oil water interface and thus act as an excellent predictor of Marangoni stabilities when combined with surface tension and particle size analyses.

Conclusions

This study thoroughly investigated the effects of surfactant and salinity on the emulsion stability of simulated bilgewater using microprofiling characterization, CLSM analysis, and traditional characterization methods (contact angle and interfacial surface tension). The study showed that emulsions stabilized with nonionic surfactants were, in general, more unstable than SDS stabilized emulsions. However, SDS emulsions were more susceptible to salinity than Triton X-100 emulsions. Furthermore, mass transfer in SDS emulsions were more affected by

salinity than Triton X-100 emulsions. This lead us to believe that Marangoni instabilities had a more pronounced effect on SDS emulsions in bilgewater compared the Triton X-100 emulsions. This study was the first to investigate *in situ* chemical interactions across an emulsion-oil interface using microsensors at a microscale, which provided *in situ* chemical concentration gradients with high spatial and temporal resolution not observed through conventional means. From the measured chemical microprofiles, the effect of mass transport on emulsion stability was investigated and it was found that emulsions stabilized with anionic surfactants (SDS) have faster mass transfer kinetics with increased salinity which correlated to decreased emulsion stability, indicating that mass transfer has an important role in emulsion stability across the oil emulsion interface. Although the contact angle and interfacial tension provide intrinsic properties before emulsion formation, characterization parameters need to be cross-evaluated to accurately determine the stability of an emulsion and multi-scale approach of emulsion characterization would be beneficial for better understanding the emulsion stability. By combining with the innovative emulsion characterizing methods (e.g. CLSM and microsensors), the results here provided better understanding of the effect of surfactant types and salinity in emulsion formation and stability for better management of bilgewater in shipboard applications.

References

- Ahmed, N.S., Nassar, A.M., Zaki, N.N. and Gharieb, H.K. (1999) Stability and rheology of heavy Crude oil-in-water emulsion stabilized by an anionic-nonionic surfactant mixture. *Petroleum Science and Technology* 17(5-6), 553-576.
- Beattie, J.K. and Djerdjev, A.M. (2004) The pristine oil/water interface: Surfactant-free hydroxide-charged emulsions. *Angewandte Chemie International Edition* 43(27), 3568-3571.
- Bensadok, K., Benammar, S., Lapicque, F. and Nezzal, G. (2008) Electrocoagulation of cutting oil emulsions using aluminium plate electrodes. *Journal of hazardous materials* 152(1), 423-430.
- Binks, B., Cho, W., Fletcher, P. and Petsev, D. (2000) Stability of oil-in-water emulsions in a low interfacial tension system. *Langmuir* 16(3), 1025-1034.
- Bourrel, M., Salager, J., Schechter, R. and Wade, W. (1980) A correlation for phase behavior of nonionic surfactants. *Journal of Colloid and Interface Science* 75(2), 451-461.
- Canizares, P., Martínez, F., Jiménez, C., Sáez, C. and Rodrigo, M.A. (2008) Coagulation and electrocoagulation of oil-in-water emulsions. *Journal of Hazardous materials* 151(1), 44-51.
- Copeland, C. (2007) Cruise ship pollution: Background, laws and regulations, and key issues, Congressional Research Service, Library of Congress.
- Dimitrova, B., Ivanov, I. and Nakache, E. (1988) Mass transport effects on the stability of emulsion: emulsion films with acetic acid and acetone diffusing across the interface. *Journal of Dispersion Science and Technology* 9(4), 321-341.
- Friberg, S., Jansson, P.O. and Cederberg, E. (1976) Surfactant association structure and emulsion stability. *Journal of Colloid and Interface Science* 55(3), 614-623.
- Gopal, E. (1968) Principles of emulsion formation, p. 1, Academic Press: London.
- Ibanez, J.G., Takimoto, M.M., Vasquez, R.C., Basak, S., Myung, N. and Rajeshwar, K. (1995) Laboratory experiments on electrochemical remediation of the environment: electrocoagulation of oily wastewater. *Journal of Chemical Education* 72(11), 1050-1052.
- IMO (1973) International Convention for the Prevention of Pollution from Ships, as Modified by the Protocol of 1978, (MARPOL 73/78), International Maritime Organization (IMO).
- Ivanov, I., Chakarova, S.K. and Dimitrova, B. (1987) Instability of emulsion liquid films induced by the transfer of acetic acid. *Colloids and surfaces* 22(2), 301-309.
- Kajitvichyanukul, P., Hung, Y.-T. and Wang, L.K. (2006) Advanced Physicochemical Treatment Processes. Wang, L.K., Hung, Y.-T. and Shammas, N.K. (eds), pp. 521-548, Humana Press, Totowa, NJ.
- Karakulski, K., Kozlowski, A. and Morawski, A. (1995) Purification of oily wastewater by ultrafiltration. *Separations Technology* 5(4), 197-205.
- Katsuki, K., Miyagawa, Y., Matsuno, R. and Adachi, S. (2015) Evolution of the Size Distribution of Oil-droplets Over Time in Oil-in-water Emulsions. 16(3), 231-234.

- Koss, L. (1996) Technology development for environmentally sound ships of the 21st century: an international perspective. *Journal of Marine Science and Technology* 1(3), 127-137.
- Kwok, D.Y. and Neumann, A.W. (1999) Contact angle measurement and contact angle interpretation. *Advances in Colloid and Interface Science* 81(3), 167-249.
- Leal-Calderon, F., Bibette, J. and Schmitt, V. (2007) *Emulsion Science: Basic Principles*, pp. 143-172, Springer New York, New York, NY.
- Lee, W.H., Lee, J.H., Choi, W.H., Hosni, A.A., Papautsky, I. and Bishop, P.L. (2011a) Needle-type environmental microsensors: design, construction and uses of microelectrodes and multi-analyte MEMS sensor arrays. *Measurement Science and Technology* 22, 042001.
- Lee, W.H., Wahman, D.G., Bishop, P.L. and Pressman, J.G. (2011b) Free chlorine and monochloramine application to nitrifying biofilm: comparison of biofilm penetration, activity, and viability. *Environmental Science and Technology* 45, 1412-1419.
- Levine, S., Bowen, B.D. and Partridge, S.J. (1989) Stabilization of emulsions by fine particles I. Partitioning of particles between continuous phase and oil/water interface. *Colloids and Surfaces* 38(2), 325-343.
- Lewandowski, Z. and Beyenal, H. (2013) *Fundamentals of biofilm research*, CRC press.
- Lucassen-Reynders, E. and Kuipers, K. (1992) The role of interfacial properties in emulsification. *Colloids and surfaces* 65(2), 175-184.
- Martínez-Palou, R., Cerón-Camacho, R., Chávez, B., Vallejo, A.A., Villanueva-Negrete, D., Castellanos, J., Karamath, J., Reyes, J. and Aburto, J. (2013) Demulsification of heavy crude oil-in-water emulsions: A comparative study between microwave and thermal heating. *Fuel* 113, 407-414.
- McClements, D.J. (2015) *Food emulsions: principles, practices, and techniques*, CRC press.
- Mita, T., Yamada, K., Matsumoto, S. and Yonezawa, D. (1973) Dispersion State of Protein-Stabilized Emulsions: Dependence of Globule Size and Size Distribution upon pH in Concentrated Oil-in-Water Systems. *Journal of Texture Studies* 4(1), 41-52.
- Mollah, M.Y., Morkovsky, P., Gomes, J.A., Kesmez, M., Parga, J. and Cocke, D.L. (2004) Fundamentals, present and future perspectives of electrocoagulation. *Journal of Hazardous Materials* 114(1), 199-210.
- Mollah, M.Y.A., Schennach, R., Parga, J.R. and Cocke, D.L. (2001) Electrocoagulation (EC)—science and applications. *Journal of hazardous materials* 84(1), 29-41.
- Mouedhen, G., Feki, M., Wery, M.D.P. and Ayedi, H.F. (2008) Behavior of aluminum electrodes in electrocoagulation process. *Journal of Hazardous Materials* 150(1), 124-135.
- Pichot, R. (2010) *Stability and characterisation of emulsions in the presence of colloidal particles and surfactants*, The University of Birmingham.
- Schuster, D. (1987) *Encyclopedia of Emulsion Technology: Basic theory, measurement, applications*, CRC Press.

Smookler, A., Harden Jr, J. and Conroy, P. (1977) Navy development of suitable shipboard bilge oil/water separators, pp. 423-428, American Petroleum Institute.

Sterling, C.a. and Scriven, L. (1959) Interfacial turbulence: hydrodynamic instability and the Marangoni effect. *AIChE Journal* 5(4), 514-523.

Velev, O.D. and Lenhoff, A.M. (2000) Colloidal crystals as templates for porous materials. *Current Opinion in Colloid & Interface Science* 5(1-2), 56-63.

Walstra, P. (1993) Principles of emulsion formation. *Chemical Engineering Science* 48(2), 333-349.

Wilde, P.J. (2000) Interfaces: their role in foam and emulsion behaviour. *Current Opinion in Colloid & Interface Science* 5(3-4), 176-181.

Zolfaghari, R., Fakhru'l-Razi, A., Abdullah, L.C., Elnashaie, S.S.E.H. and Pendashteh, A. (2016) Demulsification techniques of water-in-oil and oil-in-water emulsions in petroleum industry. *Separation and Purification Technology* 170, 377-407.

CHAPTER FIVE: APPLICATION OF MICROSENSORS FOR CHARACTERIZATION OF A NOVEL NOBLE METAL-COATED MoS₂ NANOFILM PHOTOCATALYST FOR DEGRADATION OF EMERGING WATER CONTAMINANTS

This paper has been previously published as: Islam, A*., Church, J.*, Han, C., Chung, H.S., Ji, E., Kim, J.H., Lee, G.H., Lee, W.H. and Jung, Y. (2017) Noble metal-coated MoS₂ nanofilms with vertically-aligned 2D layers for visible light-driven photocatalytic degradation of emerging water contaminants, *Scientific Reports*, 7, 14944. *Equally contributing authors. Islam, A., Chung, H.S., Ji, E., Kim, J.H. and Jung, Y were responsible for developing the noble metal-coated MoS₂ and Han, C. was responsible for microcystin-LR quantification.

Abstract

Two-dimensional molybdenum disulfide (2D MoS₂) presents extraordinary optical, electrical, and chemical properties which are highly tunable by engineering the orientation of constituent 2D layers. 2D MoS₂ films with vertically-aligned layers exhibit numerous 2D edge sites which are predicted to offer superior chemical reactivity owing to their enriched dangling bonds. This enhanced chemical reactivity coupled with their tunable band gap energy can render the vertical 2D MoS₂ unique opportunities for environmental applications that go beyond the conventional applications of horizontal 2D MoS₂ in electronics/opto-electronics. Herein, we report that MoS₂ films with vertically-aligned 2D layers exhibit excellent visible light responsive photocatalytic activities for efficiently degrading organic compounds in contaminated water such as harmful algal blooms. We demonstrate the visible light-driven rapid degradation of microcystin-LR, one of the most toxic compounds produced by the algal blooms, and reveal that the degradation efficiency can be significantly improved by incorporating noble metals. This study suggests a high promise of these emerging 2D materials for water treatment, significantly broadening their versatility for a wide range of energy and environmental applications.

Introduction

Viable solutions for efficiently degrading emerging organic contaminants in drinking water supplies have urgently been demanded with their increasing threats to environment and human health. For instance, harmful algal blooms (HABs), a rapid increase and/or accumulation in the population of algae which can severely damage aquatic ecosystems, have recently gained substantial public attention (Heisler et al. 2008, Paerl et al. 2016, Paerl et al. 2011). The primary concern over HABs is that they release harmful cyanotoxins (Kaushik and Balasubramanian 2013, Moreira et al. 2014), which can be fatal if ingested and/or inhaled (Carmichael et al. 2001, Codd 2000). However, traditional water purification methods are designed to primarily remove suspended solids and/or individual elements of carbon, nitrogen, and phosphorus in contaminated water, which are not well suited to directly degrade algal toxins. Photocatalysis, an alternative approach based on a solar energy-driven oxidation process, has drawn substantial interest for its intrinsic simplicity and efficient operation (Antoniou et al. 2009, Feitz et al. 1999, Liu et al. 2005, Robertson et al. 2011). In this approach, photoactive catalytic materials in contact with contaminated water generate electron-hole (e^-h^+) pairs upon absorbing the solar energy. The photo-generated charge carriers dissociate dissolved oxygen (DO) in water, generating reactive oxygen species (ROS) such as hydroxyl groups and superoxide anions, which in turn disinfect pathogens (Liu et al. 2016). Photocatalytic materials (usually, oxide semiconductors) accelerate the rate of the associated chemical reactions (oxidation/reduction) in the microorganisms. However, conventional photocatalytic methods have relied on the use of ultraviolet (UV) light for e^-h^+ generation, which is limited to harness a very small portion of the available solar energy (McGuigan et al. 2012). This is because photocatalytic semiconductors possess large band gap (E_g) energies which match the UV spectrum corresponding to only ~4–

5% of the entire solar spectrum, thus, inevitably resulting in prolonged exposure and slow reaction rates. For instance, titanium dioxide (TiO_2), one of the most sought-after photocatalytic semiconductors presents $E_g > 3.0$ eV (Antoniou et al. 2009, Feitz et al. 1999, Liu et al. 2005, Robertson et al. 2011) and only harvests UV light while neglecting the broad range of the visible light which corresponds to >40% of the entire solar spectrum (Chen and Mao 2007).

Molybdenum disulphide (MoS_2), a recently rediscovered semiconductor classified as two-dimensional (2D) transition metal dichalcogenides (TMDs), presents a rich set of optical and structural properties uniquely suitable for photocatalytic reactions. In terms of optical properties; (1) It presents a band gap energy ($\sim 1.2\text{--}1.8$ eV) matching the spectral range of the visible light. Moreover, the band gap energy is highly tunable by varying the number of 2D atomic layers (Wang et al. 2012). (2) It exhibits exceptionally large sunlight absorption; for example, over an order of magnitude higher than conventional semiconductors such as silicon (Si) or gallium arsenide (GaAs) for similar thicknesses (Bernardi et al. 2013). In terms of structural advantages; (1) It can be grown vertically standing on growth substrates (e.g. silicon dioxide (SiO_2)) exposing the edges of individual 2D layers (Heydari-Bafrooei and Shamszadeh 2016, Jung et al. 2014, Kong et al. 2013). In this vertical orientation, atomically unsaturated 2D edge sites full of molybdenum (Mo) and sulfur (S) dangling bonds are maximally exposed on the surface. Consequently, the surface is highly reactive, offering large chemical/physical adsorption capacity for capturing molecules (Caslake et al. 2004, Chen et al. 2015, Heydari-Bafrooei and Shamszadeh 2016). (2) It presents suitable energy band structure with respect to the redox potentials for hydrogen- or oxygen evolution reactions (HER or OER) as its conduction (valence) band edge lies above (below) the electrostatic potential of H_2 (O_2) evolution, respectively (Caslake et al. 2004, Rasmussen and Thygesen 2015, Sakthivel et al. 2004, Singh et

al. 2015, Tong et al. 2012). A proof-of-concept demonstration of its application to microbial inactivation in contaminated water has recently been reported (Liu et al. 2005), which studies the disinfection of *Escherichia (E.) coli* for drinking water purification *via ex-situ* photocatalytic measurements.

In this work, we demonstrate rapid and efficient photocatalytic degradation of algal toxins using MoS₂ films with vertically-aligned 2D layers under visible light illumination. Particularly, we study the degradation of one of the most toxic organic compounds generated from harmful algal blooms, microcystin-LR (MC-LR), which is recognized as an emerging threat to a wide range of water sources, including seawater, river, and lakes. We investigate its photocatalytic reaction kinetics by *in situ* characterization of ROS generation using microsensors. Moreover, we identify that the coating of thin noble metal layers on top of pristine MoS₂ films significantly improves the photocatalytic efficiency, enabling the rapid and complete removal of MC-LR. The underlying mechanisms for the observed photocatalytic reactions as well as their governing parameters are also discussed. The study suggests the promise and versatility of MoS₂ films with vertically-aligned 2D layers for a broad range of water purification and environmental applications.

Materials and Methods

Synthesis and validation of MoS₂ films with vertically aligned layers

MoS₂ films with vertically aligned layers were grown *via* the sulfurization of Mo-deposited SiO₂/Si substrates in a chemical vapor deposition (CVD) furnace. High-quality Mo films were deposited on Si/SiO₂ wafers using an e-beam evaporation system (Thermionics VE-100) with the deposition rate of 0.15 Å/s. The Mo/Si/SiO₂ substrates were placed at the center of a CVD furnace (Lindberg/Blue M Mini-Mite) while an alumina boat containing S powder is

located at the upstream side. Following the evacuation down to the base pressure of ~1 mTorr and Ar purging, the CVD furnace was heated to the reaction temperature 650 °C in 15 min and was held for 10 minute under the continuous supply of Ar gas (100 SCCM). After the reaction, the furnace was naturally cooled down to room temperature. The deposition of various metals on MoS₂ films with vertically-aligned layers was achieved *via* e-beam evaporation with the deposition rate of 0.15 Å/s.

The crystalline structure and the chemical composition of 2D MoS₂films with vertically-aligned layers were characterized using a JEOL ARM200F FEG-TEM/STEM with a Cs-corrector. TEM samples were prepared by transferring the 2D MoS₂ films from SiO₂/Si substrates to holey carbon TEM grids by using diluted hydrogen fluoride which etches away the SiO₂. All TEM/ADF-STEM operations were performed at an accelerating voltage of 200 kV.

Raman and PL characterizations were performed with a Raman spectroscopy (Renishaw) with a diode-pumped solid state laser of 532 nm wavelength and a spot size of 1 μm. Raman shifts and PL peaks were obtained under illumination for 10 seconds with power of 156 μW and 2 mW, respectively.

XPS measurements were performed using PHI-5700 spectrometer with monochromatic Al Kα x-ray (1486.6 eV) below 4×10^{-9} Torr. The Shirley-type background was removed from the measured XPS spectra. For UPS and absorbance measurements, as-prepared MoS₂ films on SiO₂/Si growth substrates were first spin-coated with polymethyl methacrylate (PMMA). The samples were subsequently transferred onto transparent sapphire substrates followed by the etching of SiO₂ and removal of PMMA.

The UV-Vis absorption spectra were obtained using a UV-Vis spectrophotometer (Cary5000, Agilent). The absorption coefficient and the optical

energy gap have been determined by characterizing the transmission $T(\lambda)$ and reflection $R(\lambda)$ spectra of the samples in the spectral wavelength range of 170~3300 nm. For electrical characterizations, the metal contacts of aluminum/chrome/gold (Al/Cr/Au) (20/5/20 nm) electrodes are fabricated on top of as-prepared MoS₂ films on SiO₂/Si substrates using e-beam lithography. Electrical transport properties were measured by a Keithley 4200 semiconductor parameter analyzer.

Photocatalytic degradation of MC-LR using microsensors

Dissolved oxygen (DO) and hydrogen peroxide (H₂O₂) concentration microprofiles were measured using a commercial DO microsensor (10 μm tip size, UNISENSE A/S, Denmark) and a platinum (Pt)-based H₂O₂ microsensor fabricated with a 50 μm tip diameter. A 3% hydrogen peroxide solution (H324-500, Fisher) was used to calibrate the H₂O₂ microsensor. The DO microsensor was calibrated in oxygen saturated (21% DO, 8.6 mg O₂ L⁻¹ at 23 °C) and deionized (DI) water under nitrogen bubbling (0% DO). The microsensors were calibrated before and after each measurement. For microprofiling, MoS₂ samples were placed in a microprofile chamber with a 2 mL min⁻¹ continuous flow of DI water. Positioning and movement of the microsensor tip towards the sample was accomplished using a three-dimension (3D) micromanipulator (UNISENSE A/S, Denmark) and observed using a stereomicroscope with a CCD camera (World Precision Instruments, Sarasota, FL, USA). A silver/silver chloride (Ag/AgCl) reference electrode (MI-401, Microelectrodes Inc., Bedford, NH, USA) was positioned using a helping hand (VTHH, Veleman Inc., Forth Worth, TX, USA) and a lab jack (Swiss Boy Model 110, Fisher Scientific) was used to position the MoS₂ samples in view of the microscope. Microsensor electrical signal (mV or pA) was measured using a multimeter (UNISENSE A/S, Denmark) and

the experiments were performed in a Faraday cage (81-334-04, Technical Manufacturing Co. Peabody, MA) to minimize electrical interference. Microprofile measurements were conducted at 50–100 μm intervals with 5 seconds of wait time between each measurement. Three replicate profiles were obtained for each parameter and the microprofiles shown in Fig. 4 are the averaged values of these replicates. Microprofiles were taken from 2,000 μm above the MoS_2 film surface to the solution surface.

XTT reduction assay for monitoring ROS production

2-methoxy-4-nitro-5-sulfo-phenyl-2H-tetrazolium-5-carboxanilide inner salt (XTT) assay (X4626, Sigma Aldrich, St. Louis, MO) was used to investigate ROS production. XTT reduced by superoxide radical anions ($\text{O}_2^{\cdot-}$) generates water-soluble XTT-formazan with a maximum absorption at 470 nm, and the formazan produced by the reaction can be used to determine the relative amount of produced ROS (Yang et al. 2014). Metal-coated MoS_2 films of identical size (3 cm^2) were tested. 40 mL of XTT (0.4 mM) dissolved in phosphate buffered saline was used to submerge the samples while being exposed to 16,000 Lux ($4.47 \times 10^{-3} \text{ W cm}^{-2}$) continuous cool-white fluorescent light illumination. A shaker table was used at 90 RPM to keep the samples well mixed. Absorbance at 470 nm was taken using a spectrophotometer (DR 900, HACH Co., Loveland, CO) for two days to determine the rate of ROS generation.

Degradation of MC-LR

The photocatalytic removal of MC-LR in pristine MoS_2 and metal-coated MoS_2 films was investigated under an illumination with a fluorescent lamp. As reactors, PYREX™ reusable borosilicate petri-dishes (diameter: 60 mm and depth: 15 mm, Fisher Scientific) were used to contain MC-LR solutions (total volume of 10 mL in each reactor). A stock solution of MC-LR (475815, Calbiochem) of 500 mg L^{-1} was first prepared using SQ water (18 mega ohm of a

resistivity) and then diluted to $250 \mu\text{g L}^{-1}$ or $500 \mu\text{g L}^{-1}$ with $\text{pH} = 5.8$. Subsequently, MoS_2 samples were loaded in the reactors covered with aluminum foils and were kept for 3 hours to reach the adsorption equilibrium before illumination (light intensity of $4.75 \times 10^{-4} \text{ W cm}^{-2}$ measured with Newport broadband radiant power meter (Newport Corporation)). After illumination, the concentration of the MC-LR taken out of the reactors was determined by Agilent series 1100 high-performance liquid chromatograph (HPLC) with a C18 reversed-phase column (Supelco C18 Discover HS column, $150 \text{ mm} \times 2 \text{ mm}$, $5 \mu\text{m}$ particle size, Supelco, USA). Liquid with a unit volume of $20 \mu\text{L}$ was constantly injected under the flow rate of 0.2 mL min^{-2} , following the previously reported method (Antoniou et al. 2008, Han et al. 2011, Pelaez et al. 2009).

Results and Discussion

Figure 5-1(a) is the schematic illustration demonstrating the concept of photocatalytic degradation of emerging water contaminants using semiconducting 2D MoS_2 photocatalysts. MoS_2 films with vertically aligned 2D layers grown on SiO_2/Si substrates are immersed in a water bath containing algal toxins (MC-LR in this case) absorbing photons from the visible light, which readily generates e^-h^+ . These charge carriers migrate to the semiconducting surface where they react with hydroxyl ions and oxygen compounds to generate highly reactive species (i.e. O_2^- , $\cdot\text{OH}$, and H_2O_2) that can degrade the algal toxins. Figure 5-1(b) is an image of a MoS_2 film with vertically aligned 2D layers grown on a SiO_2/Si wafer of $>2 \text{ cm}^2$ in size. The growth of the MoS_2 film with vertically aligned 2D layers was achieved by the sulfurization of Mo-deposited wafers following the previously reported method (Kong et al. 2013). Figure 5-1(c) is a representative high-resolution transmission electron microscopy (HRTEM) image of a MoS_2 film with vertically-aligned 2D layers. It is apparent that the MoS_2 film predominantly exposes the

edge sites of vertically-aligned 2D layers perpendicular to the substrate surface. The film presents continuously connected vertically-aligned 2D MoS₂ layers, uniformly covering the entire surface.

The annular dark field (ADF) scanning TEM (STEM) image in Fig. 5-1(d) allows for a near atomic-scale investigation of a single MoS₂ grain with vertically-aligned 2D layers. The image clearly identifies the individual atomic planes of molybdenum (Mo) and sulfur (S) organized in an S-Mo-S sequence with heavier Mo atoms appearing brighter than S atoms. The projected atomic structure of MoS₂ is superimposed on the image, indicating an interlayer spacing of ~0.62 nm. The presented structural model matches the image of the projected MoS₂ atomic structure, indicating that the MoS₂ film predominantly expose the semiconducting 2H hexagonal phases (Deokar et al. 2017, Li et al. 2016). For the purpose of photocatalytic performance tests, some MoS₂ films with vertically-aligned 2D layers were coated with thin layers of noble metals. Figure 5-1(e) shows a HRTEM image of a platinum (Pt; ~3 nm thick)-deposited MoS₂ film with vertically-aligned 2D layers. The image reveals that individual Pt nanoparticles are uniformly and discontinuously distributed, while the vertical 2D layer edges are well maintained even with the Pt coating (Fig. 5-1(f)).

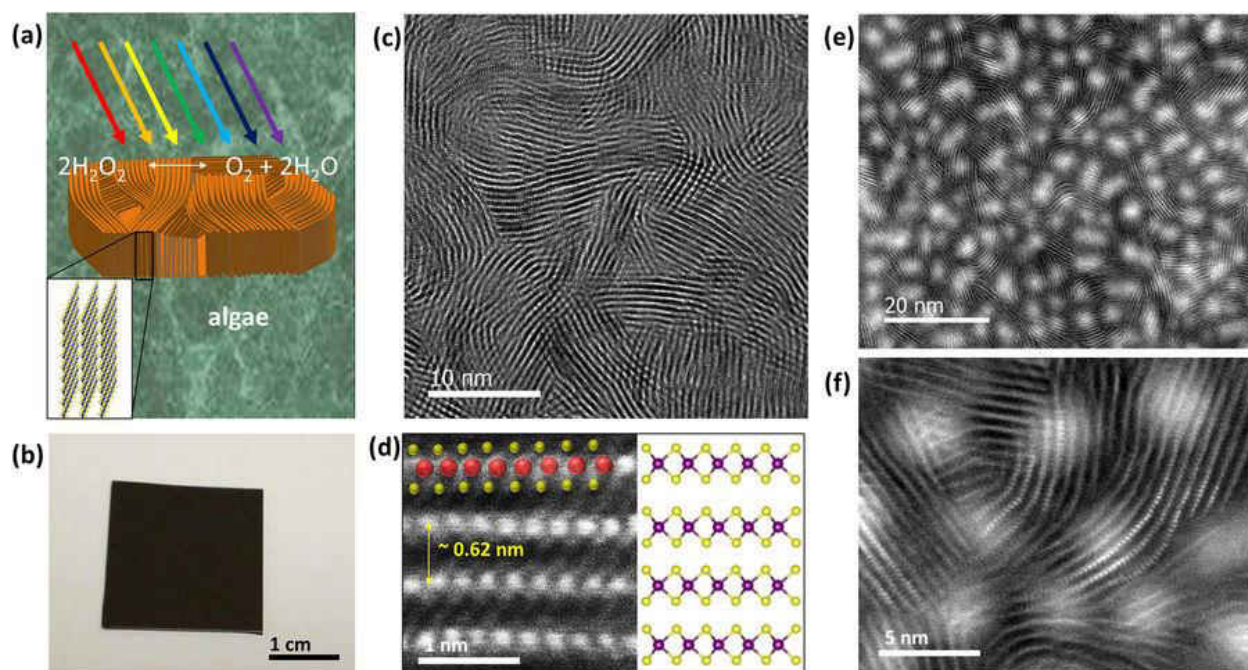


Figure 5- 1. Concept for photocatalytic degradation of MC-LR and TEM characterizations of MoS₂ films with vertically-aligned layers. (a) Schematic illustration for photocatalytic degradation using MoS₂ films. (b) Image of an as-grown MoS₂ film. (c) HRTEM image to show vertically-aligned 2D MoS₂ layers. (d) ADF-STEM image and atomic structure comparison of vertically-aligned 2D layers. (e) HRTEM image to show the uniform distribution of Pt nanoparticles on the vertically-aligned 2D layer edges. (f) Close-up image to show that vertical 2D layer edges are well maintained even after Pt incorporation.

Detailed structural and chemical characterizations were further performed. In Fig. 5-2(a), Raman spectra obtained from the MoS₂ films grown with Mo seeds of various thicknesses are presented. For all film thicknesses, the Raman spectra show strong signatures of both the in-plane (E_{2g}) and out-of-plane (A_{1g}) phonon modes of MoS₂. The intensity ratio of A_{1g} mode to $E_{1/2g}$ mode (A_{1g}/E_{2g}) increases with increasing Mo thickness, which indicates the pronounced exposure of 2D edge sites and is consistent with previous studies (Kong et al. 2013). Figure 5-2(b) shows the change in the A_{1g}/E_{2g} intensity ratio as a function of Mo thickness (red), while there is no significant thickness-dependent change in the frequency difference of $A_{1g}-E_{1/2g}$ (blue). The thickness of the MoS₂ film with vertically-aligned 2D layers was identified by cross-section TEM characterizations. The thickness of initial Mo seeds increases by ~3 times after the

sulfurization, which was consistently observed for Mo thickness from 5 nm to 20 nm. Figure 5-2(c) is the photoluminescence (PL) spectra obtained from the same MoS₂ films with vertically-aligned 2D layers in Fig. 5-2 (a) and (b). We observe that MoS₂ films with a thickness of <10 nm exhibit two emission peaks centered around 1.81 eV and 1.96 eV, corresponding to the A and B excitons of MoS₂ (Deokar et al. 2017). The observation of such strong PL peaks is interesting as they are typically observed in mono-to-few layer horizontal 2D MoS₂ flakes of much smaller thickness (<a few nm) (Deokar et al. 2017). Similar observations of PL peaks in vertically-aligned 2D MoS₂ layers have previously been reported (Wang et al. 2013), while the exact mechanism for the PL emission remains unclear at present.

X-ray photoelectron spectroscopy (XPS) characterizations were performed to investigate the chemical composition and the atomic bonding characteristics of the MoS₂ film with vertically-aligned 2D layers. Figure 5-2(d) and (e) show the XPS spectra for the Mo3*d* and S2*p* core levels of the studied sample. The absence of a noticeable peak at 235.2 eV corresponding to Mo-O bonds indicates a negligible formation of molybdenum oxides. No noticeable peaks corresponding to the S-O formation in the S2*p* states are observed, which indicates the negligible oxidation of sulfur in the sample. The chemical compositions of the MoS₂ film was determined by analyzing the Mo3*d* and S2*p* peak areas with relative sensitivity factors of 9.5 and 1.67, respectively. The atomic ratio of Mo and S is identified to be ~1:1.85, indicating a small density of S vacancies, which is commonly observed chemically synthesized MoS₂ and is known to introduce n-type intrinsic doping (McDonnell et al. 2014).

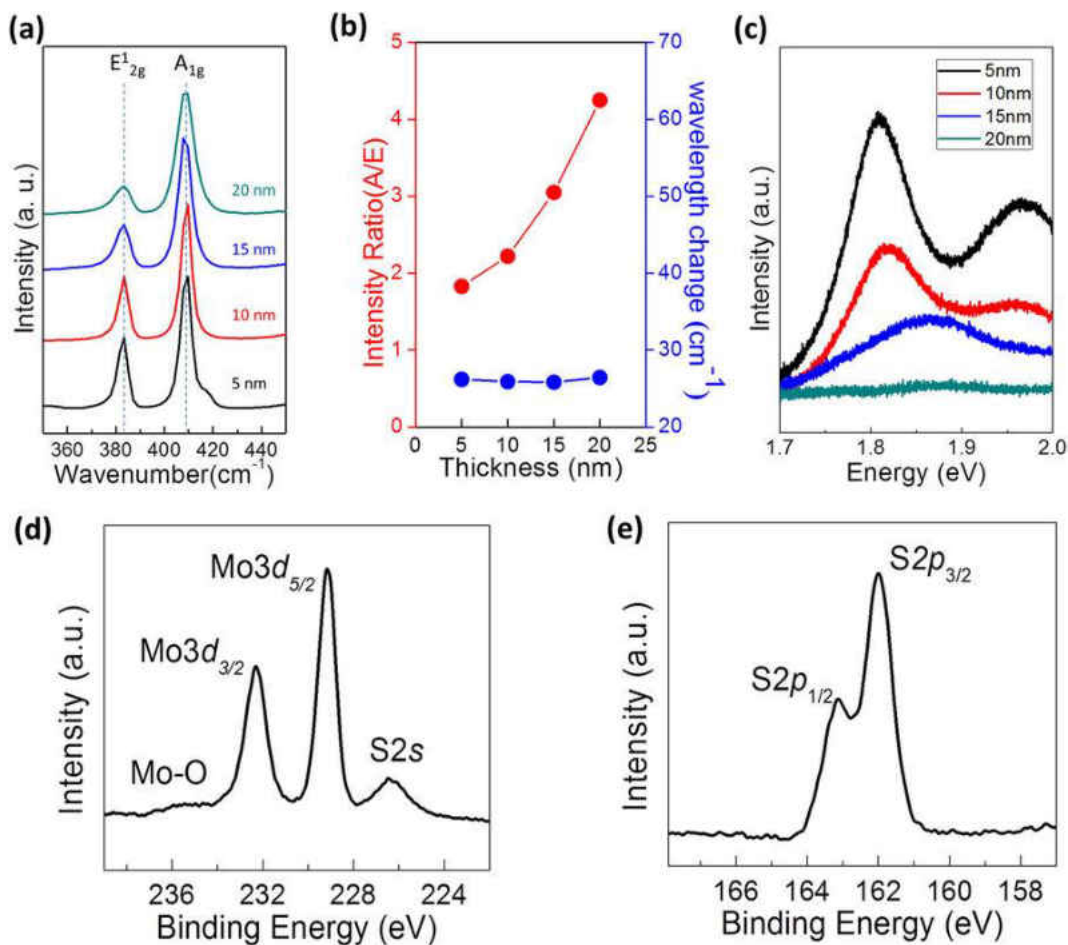


Figure 5- 2. Structural and chemical characterizations by Raman, PL, and XPS. (a) Raman spectra obtained from the MoS₂ films grown with Mo seed layers of various thicknesses. (b) A_{1g}/E_{1 2g} intensity ratio and frequency difference of A_{1g}–E_{1 2g} as a function of Mo thickness. (c) PL spectra obtained from the corresponding MoS₂ films. XPS spectra of a MoS₂ film for (d) Mo3d and (e) S2p core levels.

Electronic band structures of the MoS₂ films with vertically-aligned 2D layers were identified to assess their feasibility for visible light-driven photocatalytic reactions. Figure 5-3(a) shows the UV-vis spectra obtained from a MoS₂ film (thickness: ~20 nm) transferred on a transparent sapphire substrate. Two prominent exciton absorption peaks corresponding to A and B excitons at ~1.8 eV and ~2.0 eV were observed, which originates from the strong spin-orbit splitting of the valence band. The absorbance tail observed in the regime I at a

wavelength < 1.8 eV indicates the indirect band transition (Fig. 5-3(a) inset). The band gap (E_g) of the sample was estimated by using the Tauc's equation,

$$(\alpha(\nu) * h\nu)^{1/n} = A(h\nu - E_g) \quad (1)$$

where $\alpha(\nu)$, A , n are the absorption coefficient, proportionality constant, and gap-type depending exponent, respectively (Choi et al. 2012, Saha et al. 2015). In this case, $n = 2$ is assigned such that multi-layered MoS₂ presents indirect band gap originating from the maximum of valence band at Γ and the minimum of conduction band halfway between Γ and K (Mak et al. 2010). The inset of Fig. 3-5(a) presents the variations of $(\alpha h\nu)^{1/2}$ vs. $h\nu$ for the MoS₂ film with vertically-aligned 2D layers. The red straight dashed line indicates the indirectly allowed transition region in the sample, from which E_g of ~ 1.59 eV is extracted. This value of E_g belongs to the visible light regime of the solar spectrum, indicating that the MoS₂ film with vertically-aligned 2D layers can absorb sun light up to ~ 780 nm. This enhanced absorption corresponds to $\sim 50\%$ increase in energy compared to other oxide semiconductor photocatalysts which are sensitive to UV light only (i.e. 4–5% of the whole solar spectrum). The positions of the valence band (VB) and the work function of the MoS₂ film were determined by ultraviolet photoemission spectroscopy (UPS) and scanning kelvin probe microscopy (SKPM). The characterizations were performed on the MoS₂ films transferred onto conductive (e.g. gold (Au)-deposited) Si/SiO₂ substrates. The VB position is identified to be ~ -6.07 eV, which is ~ 1.5 eV lower than the Fermi level of Au as shown in Fig. 5-3(c). The work function of the MoS₂ film is extracted to be ~ -4.57 eV based on the surface potential difference of ~ 0.3 V in Fig. 5-3(c). Figure 5-3(d) presents the band structure of the MoS₂ film with respect to ROS reaction potentials. It is noted that the Fermi level of the MoS₂ film is close to the conduction band (CB) edge implying its n-type carrier transport, as also predicted from XPS analysis which indicates intrinsic n-doping

owing to S vacancies. The results indicate that MoS₂ films with vertically-aligned 2D layers possess electronic structures suitable for ROS generation and photocatalytic reactions (Liu et al. 2016). The carrier transport properties of the MoS₂ film with vertically-aligned 2D layers were also evaluated by measuring its sheet resistance (R_s). Two metal contacts were deposited on the either sides of the as-grown MoS₂ film channel defined by e-beam lithography (Fig. 5-3(e) insert). The current-voltage characteristic in Fig. 5-3(e) shows Ohmic transport with R_s of $\sim 2.63 \times 10^9 \Omega/\square$. The sheet resistance of the MoS₂ film is observed to be three orders of magnitude larger than that of monolayer horizontal MoS₂ flakes where the carrier transport occurs on the basal planes of 2D layers. This large in-plane R_s of the vertically-aligned 2D MoS₂ layers indicates the hopping-dominated carrier transports accompanied by significant carrier scattering across the van der Waals gaps in between vertical 2D layers (Li et al. 2014).

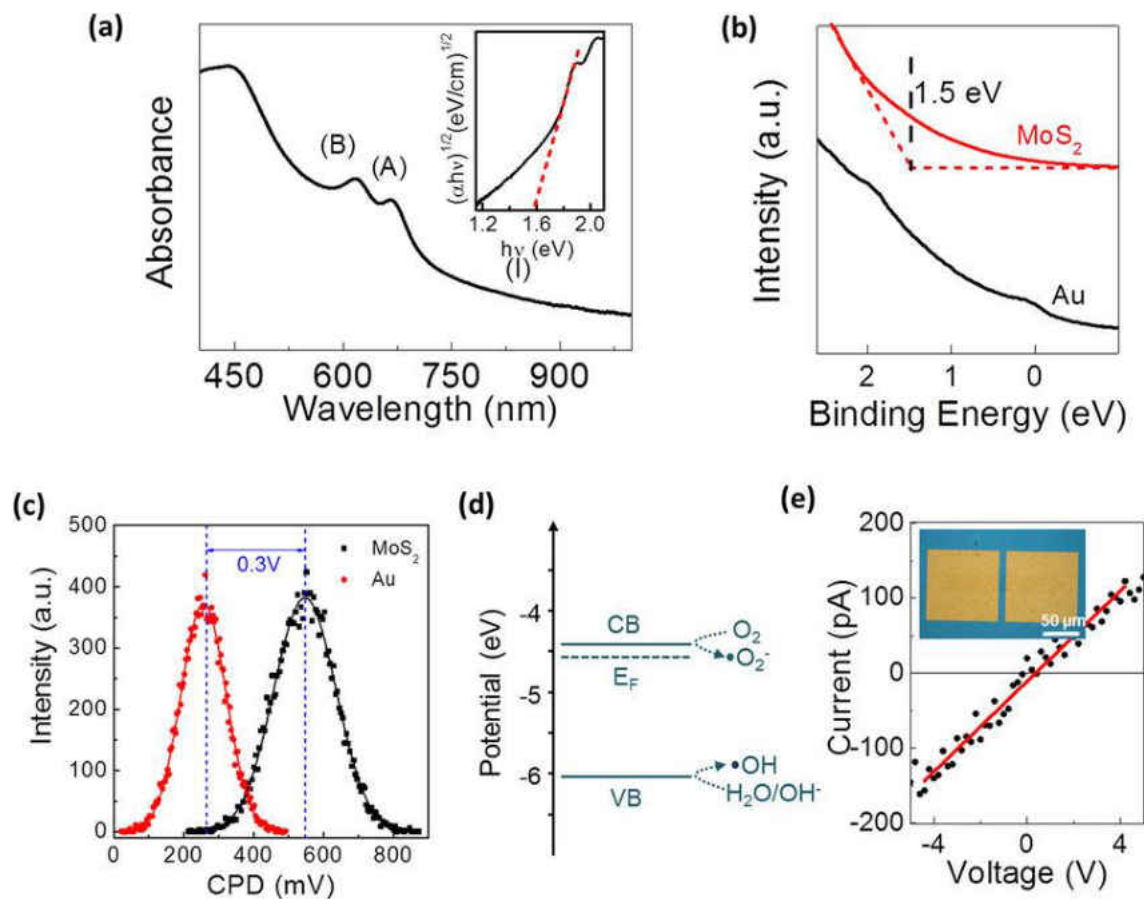


Figure 5- 3. Band structure determination by optical and electrical characterizations. (a) UV-vis spectrum from a MoS₂ film with thickness of 20 nm. The inset shows the extraction of band gap (E_g). **(b)** UPS measurement for the determination of VB position in the MoS₂ film. **(c)** Surface potentials of MoS₂ and reference Au measured by scanning kelvin probe microscopy. **(d)** Band structure of the MoS₂ film with respect to the redox potentials for hydrogen- or oxygen evolution reactions. **(e)** Current-voltage characteristics of a MoS₂ film on a SiO₂/Si substrate. Inset shows the optical image of the corresponding device.

Photocatalytic performances of various MoS₂ films were evaluated for the visible light-driven production of ROS and degradation of MC-LR. The tested samples include pristine MoS₂ and MoS₂ films coated with thin (5 nm) noble metals (platinum (Pt), copper (Cu), gold/palladium (Au/Pd)). The production of ROS was monitored using H₂O₂ detection microsensors and 2,3-bis (2-methoxy-4-nitro-5-sulfophenyl)-2H-tetrazolium-5-carboxanilide inner salt (XTT) essay. In photocatalysis, chemical reactions occur at the photo-reactive surfaces in aqueous solutions, thus *in situ* measurements of the mass transfer of reactants and products are

essential to understand the overall photocatalytic reactions. The concentration gradient microprofiles of O_2 and H_2O_2 , an indication of ROS production, were directly measured using a commercial DO microsensor and a home-built Pt-based H_2O_2 microsensor (Fig. 5-4(a)). For *in situ* microprofiling, MoS_2 samples were placed inside a microprofile chamber (Woo Hyung et al. 2011) with a 2 mLmin^{-1} continuous flow of deionized (DI) water and a silver/silver chloride (Ag/AgCl) was used as a reference electrode (Fig. 5-4(b)). The ROS production from various MoS_2 films immersed in MC-LR baths was quantified by the optical absorption of XTT at 470 nm wavelength. An increase in the optical density (OD) indicates an increase of ROS concentration (i.e. $O_2^{\cdot-}$) under illumination (Okay et al. 2015). Figure 5-4(c) shows the ROS production (denoted as OD_{470}) from MoS_2 films of various types as a function of illumination time. It is clear that all the tested films present noticeable ROS production, exhibiting a linear relationship in OD_{470} vs. time. Amongst them, the Pt-coated MoS_2 film exhibits the highest ROS production rate (determined from the slopes of the plots). DO concentration microprofiles of the corresponding samples are shown in Fig. 5-4(d), which indicates O_2 concentrations in solutions as a function of the distance from the photo-reactive surface. The Pt-coated MoS_2 exhibits the largest consumption of oxygen with a surface concentration of $5.8\text{ mg } O_2\text{ L}^{-1}$, which corresponds to $2.2\text{ mg } O_2\text{ L}^{-1}$ consumption in comparison to the bulk concentration ($8.02 \pm 0.2\text{ mg } O_2\text{ L}^{-1}$). The result suggests that Pt-coated MoS_2 films are highly photocatalytic under visible light illumination, and are consistent with the XTT characterizations (Fig. 5-4(c)). The detailed kinetics of ROS production in Pt-coated MoS_2 films were further revealed by quantifying the conversion ratio of O_2 to H_2O_2 using the H_2O_2 and DO microsensors (Fig. 5-4(e)). Details for the microsensor characterizations are in the methods. The microprofiles reveal that 60% of the O_2 consumed at the film surface is being stoichiometrically converted to H_2O_2 , following

$2\text{H}_2\text{O}_2 \leftrightarrow \text{O}_2 + 2\text{H}_2\text{O}$. The overall results obtained from XTT analysis and *in situ* microsensor characterizations confirm that Pt-coated MoS_2 films efficiently produce ROS under visible light.

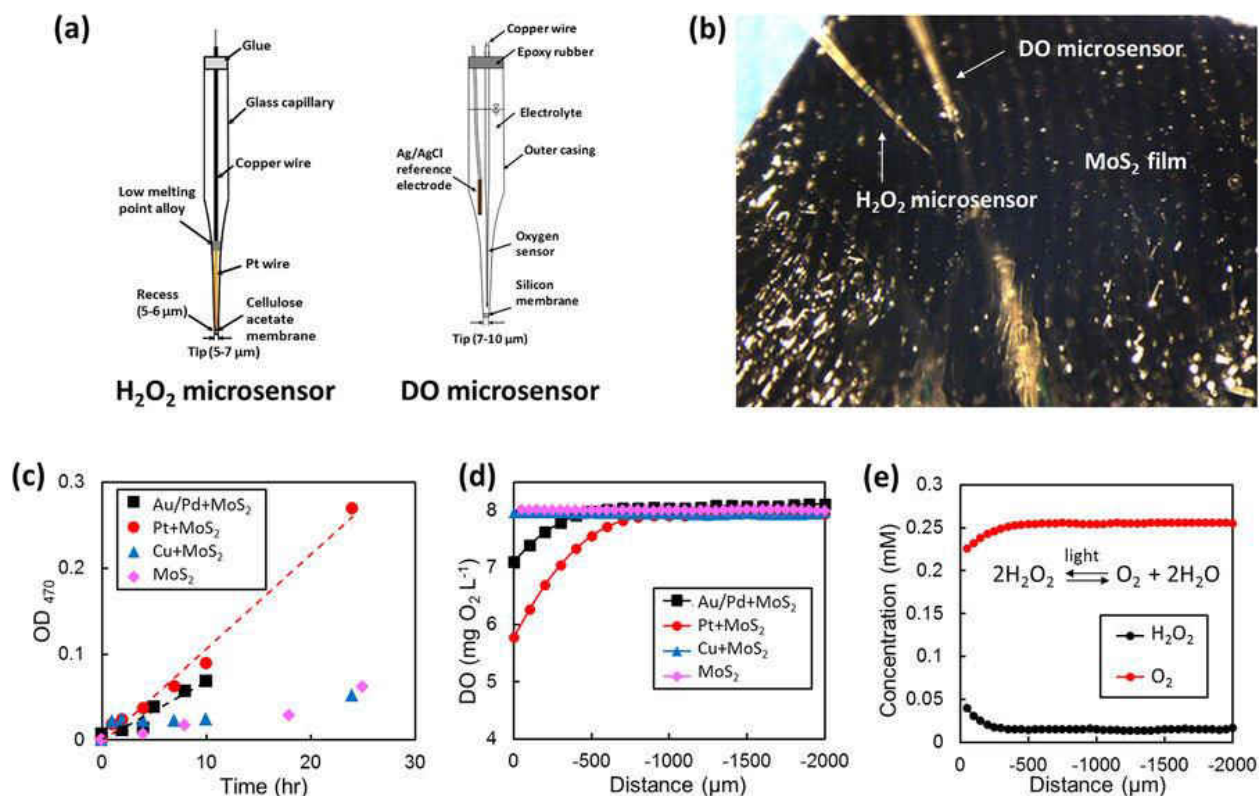


Figure 5- 4. *In situ* monitoring of ROS production. (a) H_2O_2 and dissolved oxygen (DO) microsensors for *in situ* characterizations of H_2O_2 production and O_2 consumption (b) Image of H_2O_2 and DO microsensors immersed in a water bath (c) ROS production from MoS_2 films of various types measured by absorbance of XTT-formazan at 470 nm (optical density [OD]₄₇₀). (d) DO concentration microprofiles of various MoS_2 films (e) H_2O_2 and DO concentration microprofiles at the surface of Pt-coated MoS_2 film. 0 μm represents the top surface of the film. All the microprofiles were obtained after ~ 30 min exposure to water.

The direct photocatalytic removal of MC-LR with various MoS_2 -based films using a visible light illuminating fluorescent lamp (Spectrum data is in Appendix D) was further investigated in Fig. 5-5. Figure 5-5(a) presents the relative concentration (normalized to initial concentration) of removed MC-LR as a function of time. Pt-coated MoS_2 films present the fastest removal of MC-LR under identical conditions (pH = 5.8 and initial MC-LR concentration = 250 $\mu\text{g L}^{-1}$), achieving a complete removal within 2 hours after the onset of

illumination. It is worth mentioning that pristine MoS₂ films also remove MC-LR slightly faster than Cu-only film, indicating the intrinsic photocatalytic activity of vertical MoS₂ with E_g tailored to visible light. Cu-coated MoS₂ films exhibit higher removal rate than both pristine MoS₂ and Cu-only, indicating that metal coatings noticeably improve the overall degradation efficiency. Moreover, it is interesting to note that the removal of MC-LR occurs even before illumination (in the dark), which is attributed to the adsorption of MC-LR to the samples.

Figure 5-5(b) compares the contribution of adsorption and photocatalytic activity that account for the total degradation of MC-LR. The plots reveal that pristine MoS₂ films do not exhibit a noticeable removal of MC-LR by adsorption-only, further indicating their intrinsic photocatalytic activity. Thus, the significantly improved removal efficiency achieved in Pt-coated MoS₂ films is likely the result of the synergetic effects of adsorption (mainly contributed by Pt) and photocatalytic reaction (contributed by both Pt and MoS₂).

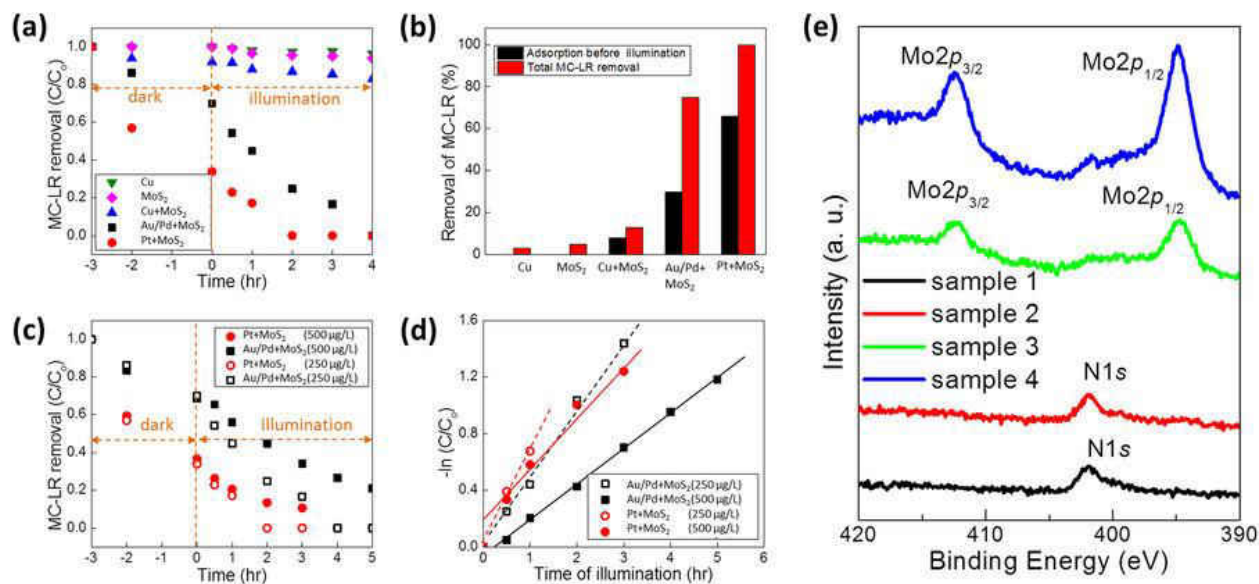


Figure 5- 5. Photocatalytic degradation of MC-LR at pH 5.8. (a) Removal of MC-LR as a function of illumination time (initial MC-LR concentration of 250 µg L⁻¹). (b) Comparison of adsorption with various samples after two hour illumination. (c) Comparison of MC-LR removal for Pt + MoS₂ and Au/Pd + MoS₂ at concentrations of 250 µg L⁻¹ and 500 µg L⁻¹. (d) Determination of rate constants for the photocatalytic degradation of MC-LR with Pt + MoS₂ and Au/Pd + MoS₂ based on the pseudo first-order kinetics. (e) XPS characterizations to show the appearance of N1s peaks in MC-LR tested samples (sample 1 and 2) in comparison to pristine samples (sample 3 and 4). Sample 1,3 and 2,4 were prepared from Mo films of 10 nm and 15 nm thickness, respectively.

Additional experiments were performed using Pt- and Au/Pd-coated MoS₂ samples using MC-LR with initial concentration of 500 µg L⁻¹ and were compared to the results obtained with 250 µg L⁻¹ (Fig. 5-5(a)). Figure 5-5(c) shows that both samples efficiently degrade MC-LR under illumination while the degradation rate decreases with increasing MC-LR concentrations. The detailed kinetics for the degradation of MC-LR were analyzed. Figure 5-5(d) presents the degradation kinetics for both Pt- and Au/Pd-coated MoS₂ in the logarithmic plots of MC-LR concentration as a function of illumination time. The plots indicate that MC-LR degradation follows pseudo first-order kinetics, yielding rate constants of 0.2451 and 0.4884 h⁻¹ for Au/Pd and 0.4084 and 0.6769 h⁻¹ for Pt, respectively, obtained from 500 µg L⁻¹ and 250 µg L⁻¹ of MC-LR. These results indicate that the incorporation of noble metals into photocatalytic MoS₂ films

significantly improve the efficiency of e^-h^+ separation resulting in enhanced photocatalytic activity. Similar results have previously been reported with other photocatalytic semiconductors which possess much larger E_g , thus, are sensitive to UV light-only (Han et al. 2014, Lee et al. 2008, Pulido Melián et al. 2012, Wang and Lim 2013). In order to clarify the adsorption-driven removal of MC-LR in the dark, we performed additional XPS characterizations (Fig. 5-5(e)). We focused on comparing the characteristics of N1s signals for MoS₂ samples exposed to MC-LR in the dark and pristine MoS₂. Figure 5-5(e) shows the XPS spectra from the MC-LR tested (sample 1 and 2) and pristine (sample 3 and 4) samples for the binding energies between 390 eV–420 eV. The results reveal that the MC-LR tested samples present pronounced N1s peaks which are absent in pristine MoS₂ films, indicating the significant adsorption of MC-LR in the dark. We further investigated the exclusive contribution of MC-LR adsorption in the dark on its overall degradation (Fig. 5-5(b)) by fitting a type II pseudo second order adsorption model to the MC-LR degradation kinetics obtained under dark/illumination conditions (Appendix D). The analysis successfully decouples the adsorption and photocatalytic effects, and further verifies that the observed MC-LR degradation under illumination is a combine result of both the effects.

The effect of noble metals on enhancing photocatalytic activity can be understood considering the following factors; (a) Noble metals of high work functions in contact with n-type MoS₂ form low-barrier Schottky junctions which facilitate the separation of e^-h^+ , promoting their migration and participation in ROS generation (Ismail 2012, Subramanian et al. 2004, Tanabe and Ozaki 2014, Yoon et al. 2015). We identify that our n-type MoS₂ with vertically-aligned layers (Fig. 5-3(d)) in contact with Pt form low-barrier Schottky junctions with the Fermi level pinning of MoS₂ close to its conduction band (Appendix D). Significantly enhanced photocatalytic activities have also been reported in oxide semiconductor photocatalysts of large

E_g after incorporating metals (Han et al. 2014), consistent with our studies. (b) Nanoscale noble metals introduce localized surface plasmon resonances (SPR) which significantly increases optical absorption in the visible light spectrum (Zhou et al. 2014), leading to further enhancement in photocatalytic activity. (c) 2D MoS₂ with vertically-aligned layers present ~five orders of magnitude greater chemical/physical absorbance compared to horizontal 2D MoS₂ layers owing to their highly reactive 2D edge sites (Cho et al. 2015). It is anticipated that an optimal mass loading of noble metals exists for optimized photocatalytic reactions (Han et al. 2014, Pulido Melián et al. 2012), which is to be determined by a balance between enhanced optical absorption and increased electrical conductivity (e^-h^+ separation efficiency).

Conclusion

In summary, we report the visible-light driven photocatalytic degradation of MC-LR using 2D MoS₂ films with vertically-aligned layers. We reveal that coating thin noble metal layers on top of pristine MoS₂ films significantly improves the degradation efficiency, resulting in a rapid ROS production and consequent MC-LR removal. The efficient degradation of MC-LR in metal-coated MoS₂ is attributed to the combined result of the intrinsic photocatalytic activity of MoS₂ with band gap energy tailored to visible light and enhanced adsorption enabled by noble metals. This study suggests the high potential of 2D MoS₂ films with vertically-aligned layers for photocatalysts, thus have great implications for a wide range of environmental applications for sustainable emerging contaminants degradation and water purification.

References

- Antoniou, M.G., Nicolaou, P.A., Shoemaker, J.A., Armah, A. and Dionysiou, D.D. (2009) Impact of the morphological properties of thin TiO₂ photocatalytic films on the detoxification of water contaminated with the cyanotoxin, microcystin-LR. *Applied Catalysis B: Environmental* 91(1-2), 165-173.
- Antoniou, M.G., Shoemaker, J.A., de la Cruz, A.A. and Dionysiou, D.D. (2008) LC/MS/MS structure elucidation of reaction intermediates formed during the TiO₂ photocatalysis of microcystin-LR. *Toxicon* 51(6), 1103-1118.
- Bernardi, M., Palummo, M. and Grossman, J.C. (2013) Extraordinary sunlight absorption and one nanometer thick photovoltaics using two-dimensional monolayer materials. *Nano letters* 13(8), 3664-3670.
- Carmichael, W.W., Azevedo, S., An, J.S., Molica, R., Jochimsen, E.M., Lau, S., Rinehart, K.L., Shaw, G.R. and Eaglesham, G.K. (2001) Human fatalities from cyanobacteria: chemical and biological evidence for cyanotoxins. *Environmental health perspectives* 109(7), 663.
- Caslake, L.F., Connolly, D.J., Menon, V., Duncanson, C.M., Rojas, R. and Tavakoli, J. (2004) Disinfection of contaminated water by using solar irradiation. *Applied and environmental microbiology* 70(2), 1145-1151.
- Chen, J., Wu, X.J., Yin, L., Li, B., Hong, X., Fan, Z., Chen, B., Xue, C. and Zhang, H. (2015) One-pot Synthesis of CdS Nanocrystals Hybridized with Single-Layer Transition-Metal Dichalcogenide Nanosheets for Efficient Photocatalytic Hydrogen Evolution. *Angewandte Chemie International Edition* 54(4), 1210-1214.
- Chen, X. and Mao, S.S. (2007) Titanium dioxide nanomaterials: synthesis, properties, modifications, and applications. *Chemical reviews* 107(7), 2891-2959.
- Cho, S.-Y., Kim, S.J., Lee, Y., Kim, J.-S., Jung, W.-B., Yoo, H.-W., Kim, J. and Jung, H.-T. (2015) Highly Enhanced Gas Adsorption Properties in Vertically Aligned MoS₂ Layers. *ACS Nano* 9(9), 9314-9321.
- Choi, W., Cho, M.Y., Konar, A., Lee, J.H., Cha, G.B., Hong, S.C., Kim, S., Kim, J., Jena, D., Joo, J. and Kim, S. (2012) High-Detectivity Multilayer MoS₂ Phototransistors with Spectral Response from Ultraviolet to Infrared. *Advanced Materials* 24(43), 5832-5836.
- Codd, G.A. (2000) Cyanobacterial toxins, the perception of water quality, and the prioritisation of eutrophication control. *Ecological engineering* 16(1), 51-60.
- Deokar, G., Rajput, N., Vancsó, P., Ravaux, F., Jouiad, M., Vignaud, D., Cecchet, F. and Colomer, J.-F. (2017) Large area growth of vertically aligned luminescent MoS₂ nanosheets. *Nanoscale* 9(1), 277-287.
- Feitz, A.J., Waite, T.D., Jones, G.J., Boyden, B.H. and Orr, P.T. (1999) Photocatalytic degradation of the blue green algal toxin microcystin-LR in a natural organic-aqueous matrix. *Environmental science & technology* 33(2), 243-249.
- Han, C., Likodimos, V., Khan, J.A., Nadagouda, M.N., Andersen, J., Falaras, P., Rosales-Lombardi, P. and Dionysiou, D.D. (2014) UV-visible light-activated Ag-decorated, monodisperse TiO₂ aggregates for

treatment of the pharmaceutical oxytetracycline. *Environmental Science and Pollution Research* 21(20), 11781-11793.

Han, C., Pelaez, M., Likodimos, V., Kontos, A.G., Falaras, P., O'Shea, K. and Dionysiou, D.D. (2011) Innovative visible light-activated sulfur doped TiO₂ films for water treatment. *Applied Catalysis B: Environmental* 107(1), 77-87.

Heisler, J., Glibert, P.M., Burkholder, J.M., Anderson, D.M., Cochlan, W., Dennison, W.C., Dortch, Q., Gobler, C.J., Heil, C.A. and Humphries, E. (2008) Eutrophication and harmful algal blooms: a scientific consensus. *Harmful algae* 8(1), 3-13.

Heydari-Bafrooei, E. and Shamszadeh, N.S. (2016) Synergetic effect of CoNPs and graphene as cocatalysts for enhanced electrocatalytic hydrogen evolution activity of MoS₂. *RSC Advances* 6(98), 95979-95986.

Ismail, A.A. (2012) Mesoporous PdO–TiO₂ nanocomposites with enhanced photocatalytic activity. *Applied Catalysis B: Environmental* 117-118, 67-72.

Jung, Y., Shen, J., Sun, Y. and Cha, J.J. (2014) Chemically synthesized heterostructures of two-dimensional molybdenum/tungsten-based dichalcogenides with vertically aligned layers. *ACS nano* 8(9), 9550-9557.

Kaushik, R. and Balasubramanian, R. (2013) Methods and approaches used for detection of cyanotoxins in environmental samples: a review. *Critical reviews in environmental science and technology* 43(13), 1349-1383.

Kong, D., Wang, H., Cha, J.J., Pasta, M., Koski, K.J., Yao, J. and Cui, Y. (2013) Synthesis of MoS₂ and MoSe₂ films with vertically aligned layers. *Nano letters* 13(3), 1341-1347.

Lee, M.-K., Kim, T.G., Kim, W. and Sung, Y.-M. (2008) Surface Plasmon Resonance (SPR) Electron and Energy Transfer in Noble Metal–Zinc Oxide Composite Nanocrystals. *The Journal of Physical Chemistry C* 112(27), 10079-10082.

Li, H., Wu, H., Yuan, S. and Qian, H. (2016) Synthesis and characterization of vertically standing MoS₂ nanosheets. *Scientific Reports* 6, 21171.

Li, S.-L., Komatsu, K., Nakaharai, S., Lin, Y.-F., Yamamoto, M., Duan, X. and Tsukagoshi, K. (2014) Thickness Scaling Effect on Interfacial Barrier and Electrical Contact to Two-Dimensional MoS₂ Layers. *ACS Nano* 8(12), 12836-12842.

Liu, C., Kong, D., Hsu, P.-C., Yuan, H., Lee, H.-W., Liu, Y., Wang, H., Wang, S., Yan, K. and Lin, D. (2016) Rapid water disinfection using vertically aligned MoS₂ nanofilms and visible light. *Nature nanotechnology* 11(12), 1098.

Liu, I., Lawton, L.A., Bahnemann, D.W. and Robertson, P.K. (2005) The photocatalytic destruction of the cyanotoxin, nodularin using TiO₂. *Applied Catalysis B: Environmental* 60(3-4), 245-252.

Mak, K.F., Lee, C., Hone, J., Shan, J. and Heinz, T.F. (2010) Atomically Thin MoS₂: A New Direct-Gap Semiconductor. *Physical Review Letters* 105(13), 136805.

- McDonnell, S., Addou, R., Buie, C., Wallace, R.M. and Hinkle, C.L. (2014) Defect-Dominated Doping and Contact Resistance in MoS₂. *ACS Nano* 8(3), 2880-2888.
- McGuigan, K.G., Conroy, R.M., Mosler, H.-J., du Preez, M., Ubomba-Jaswa, E. and Fernandez-Ibanez, P. (2012) Solar water disinfection (SODIS): a review from bench-top to roof-top. *Journal of hazardous materials* 235, 29-46.
- Moreira, C., Ramos, V., Azevedo, J. and Vasconcelos, V. (2014) Methods to detect cyanobacteria and their toxins in the environment. *Applied microbiology and biotechnology* 98(19), 8073-8082.
- Okuy, T.O., Bala, R.K., Nguyen, H.N., Atalay, R., Bayam, Y. and Rodrigues, D.F. (2015) Antibacterial properties and mechanisms of toxicity of sonochemically grown ZnO nanorods. *RSC Advances* 5(4), 2568-2575.
- Paerl, H.W., Gardner, W.S., Havens, K.E., Joyner, A.R., McCarthy, M.J., Newell, S.E., Qin, B. and Scott, J.T. (2016) Mitigating cyanobacterial harmful algal blooms in aquatic ecosystems impacted by climate change and anthropogenic nutrients. *Harmful Algae* 54, 213-222.
- Paerl, H.W., Hall, N.S. and Calandrino, E.S. (2011) Controlling harmful cyanobacterial blooms in a world experiencing anthropogenic and climatic-induced change. *Science of the Total Environment* 409(10), 1739-1745.
- Pelaez, M., de la Cruz, A.A., Stathatos, E., Falaras, P. and Dionysiou, D.D. (2009) Visible light-activated N-F-codoped TiO₂ nanoparticles for the photocatalytic degradation of microcystin-LR in water. *Catalysis Today* 144(1), 19-25.
- Pulido Melián, E., González Díaz, O., Doña Rodríguez, J.M., Colón, G., Navío, J.A., Macías, M. and Pérez Peña, J. (2012) Effect of deposition of silver on structural characteristics and photoactivity of TiO₂-based photocatalysts. *Applied Catalysis B: Environmental* 127, 112-120.
- Rasmussen, F.A. and Thygesen, K.S. (2015) Computational 2D materials database: electronic structure of transition-metal dichalcogenides and oxides. *The Journal of Physical Chemistry C* 119(23), 13169-13183.
- Robertson, P.K., Bahnemann, D.W., Lawton, L.A. and Bellu, E. (2011) A study of the kinetic solvent isotope effect on the destruction of microcystin-LR and geosmin using TiO₂ photocatalysis. *Applied Catalysis B: Environmental* 108, 1-5.
- Saha, N., Sarkar, A., Ghosh, A.B., Dutta, A.K., Bhadu, G.R., Paul, P. and Adhikary, B. (2015) Highly active spherical amorphous MoS₂: facile synthesis and application in photocatalytic degradation of rose bengal dye and hydrogenation of nitroarenes. *RSC Advances* 5(108), 88848-88856.
- Sakthivel, S., Shankar, M., Palanichamy, M., Arabindoo, B., Bahnemann, D. and Murugesan, V. (2004) Enhancement of photocatalytic activity by metal deposition: characterisation and photonic efficiency of Pt, Au and Pd deposited on TiO₂ catalyst. *Water research* 38(13), 3001-3008.
- Singh, A.K., Mathew, K., Zhuang, H.L. and Hennig, R.G. (2015) Computational screening of 2D materials for photocatalysis. *The journal of physical chemistry letters* 6(6), 1087-1098.
- Subramanian, V., Wolf, E.E. and Kamat, P.V. (2004) Catalysis with TiO₂/Gold Nanocomposites. Effect of Metal Particle Size on the Fermi Level Equilibration. *Journal of the American Chemical Society* 126(15), 4943-4950.

- Tanabe, I. and Ozaki, Y. (2014) Consistent changes in electronic states and photocatalytic activities of metal (Au, Pd, Pt)-modified TiO₂ studied by far-ultraviolet spectroscopy. *Chemical Communications* 50(17), 2117-2119.
- Tong, H., Ouyang, S., Bi, Y., Umezawa, N., Oshikiri, M. and Ye, J. (2012) Nano-photocatalytic materials: possibilities and challenges. *Advanced materials* 24(2), 229-251.
- Wang, H., Lu, Z., Xu, S., Kong, D., Cha, J.J., Zheng, G., Hsu, P.-C., Yan, K., Bradshaw, D., Prinz, F.B. and Cui, Y. (2013) Electrochemical tuning of vertically aligned MoS₂ nanofilms and its application in improving hydrogen evolution reaction. *Proceedings of the National Academy of Sciences* 110(49), 19701-19706.
- Wang, Q.H., Kalantar-Zadeh, K., Kis, A., Coleman, J.N. and Strano, M.S. (2012) Electronics and optoelectronics of two-dimensional transition metal dichalcogenides. *Nature nanotechnology* 7(11), 699.
- Wang, X. and Lim, T.-T. (2013) Highly efficient and stable Ag–AgBr/TiO₂ composites for destruction of *Escherichia coli* under visible light irradiation. *Water Research* 47(12), 4148-4158.
- Woo Hyung, L., Jin-Hwan, L., Woo-Hyuck, C., Ahmed, A.H., Ian, P. and Paul, L.B. (2011) Needle-type environmental microsensors: design, construction and uses of microelectrodes and multi-analyte MEMS sensor arrays. *Measurement Science and Technology* 22(4), 042001.
- Yang, X., Li, J., Liang, T., Ma, C., Zhang, Y., Chen, H., Hanagata, N., Su, H. and Xu, M. (2014) Antibacterial activity of two-dimensional MoS₂ sheets. *Nanoscale* 6(17), 10126-10133.
- Yoon, H.S., Joe, H.-E., Jun Kim, S., Lee, H.S., Im, S., Min, B.-K. and Jun, S.C. (2015) Layer dependence and gas molecule absorption property in MoS₂ Schottky diode with asymmetric metal contacts. *Scientific Reports* 5, 10440.
- Zhou, G., Xu, X., Yu, J., Feng, B., Zhang, Y., Hu, J. and Zhou, Y. (2014) Vertically aligned MoS₂/MoO_x heterojunction nanosheets for enhanced visible-light photocatalytic activity and photostability. *CrystEngComm* 16(38), 9025-9032.

CHAPTER SIX: APPLICATION OF MICROSENSORS TO CITRUS PLANTS FOR DETERMINING THE FOLIAR UPTAKE OF Zn²⁺ IN HLB TREATMENTS

This paper has been previously published as: Church, J., Armas, S.M., Patel P.K., Chumbimuni-Torres, K., and Lee, W.H., Development and characterization of needle-type ion-selective microsensors for *in situ* determination of foliar uptake of Zn²⁺ in citrus plants, *Electroanalysis*. DOI:10.1002/elan.201700697. Armas, S.M. was an equally contributing author and was responsible for providing and characterizing the Zn²⁺ ionophore.

Abstract

For over a decade, the incidence of Huanglongbing (HLB) has grown at an alarming rate, affecting citrus crops worldwide. Current methods of nutrient therapy have little to no effect in alleviating symptoms of HLB, and scarce research has been put forth towards non-destructive tools for monitoring zinc transport in citrus plants. Here, we have developed and characterized a solid contact micro-ion-selective electrode (SC- μ -ISE) for the determination of zinc transport in sour orange seedlings using a non-invasive microelectrode ion flux estimation (MIFE) technique. The SC- μ -ISE displayed a 26.05 ± 0.13 mV decade⁻¹ Nernstian response and a LOD of $(3.96 \pm 2.09) \times 10^{-7}$ M. Results showed a significant Zn²⁺ uptake in the leaves and roots of sour orange seedlings when bulk concentrations were higher than 5.99 mM. Above this concentration, a linear relationship between flux and bulk Zn²⁺ concentration was observed. This relationship suggests passive diffusion may be a key mechanism for Zn transport into plants. Overall, this study is the first to use a Zn²⁺ SC- μ -ISE for the determination of ion transport processes in plants. This novel tool can be used to further knowledge the effect of nutrient therapy and disease progression on HLB infected citrus plants.

Introduction

In the span of 10 years, Huanglongbing (HLB) has devastated Florida's 10.7-billion-dollar citrus industry. HLB has now spread into commercial groves and growers are struggling to maintain profits. Citrus HLB, or citrus greening, is caused by three species of Alphaproteobacteria: 1) *Candidatus Liberibacter asiaticus* (Ca. L. asiaticus (Las)), 2) Ca. L. africanus (Laf), and 3) Ca. L. americanus (Lam), which are limited to growth in the phloem (Bové 2006, Gottwald 2010). The disease plugs the sieve pores of the phloem which ultimately inhibits the flow of nutrients throughout the tree (Etxeberria et al. 2009, Kim et al. 2009). Therefore, HLB symptoms hallmarks nutrient deficiency; blotchy mottle leaves, yellow shoots and fruits that are underdeveloped and lopsided (Graca 1991).

Citrus trees infected with HLB have been shown to exhibit depleted levels of zinc when compared to healthy citrus trees (Nwugo et al. 2013). A study have shown that zinc concentrations could be ten times greater in healthy trees (Tian et al. 2014). Therefore, it has been common practice to supplement HLB infected trees with nutrients like zinc to alleviate the nutrient imbalance (Xia et al. 2011). Nevertheless, it is still unclear on whether nutritional therapy can alleviate the symptoms of HLB. Additionally, there is limited research connecting nutritional management to improved productivity of HLB infected citrus trees and recent reports have shown that nutritional therapy is not effective at suppressing Las or alleviating HLB symptoms (Gottwald et al. 2012). The lack of information is likely due to current methodology employed to monitor zinc content in citrus plants. Currently, zinc is detected primarily using inductively coupled plasma atomic emission spectroscopy (ICP-AES) or atomic absorption spectroscopy (AAS) for which samples need to be dried, grounded, and digested before analysis (1998). This process is time consuming, expensive, destructive, non-portable and does not give

the temporal or spatial resolution needed to truly understand the movement of zinc through the phloem of citrus plants. Therefore, there is an urgent need to develop a reliable, non-invasive, non-destructive tool capable of tracking zinc's systemic activity directly in plants.

Polymer-based micro ion-selective electrodes (μ -ISE) can meet the desired qualities of a non-invasive tool for *in situ* analysis of citrus plants. These μ -ISEs provide the needed selectivity via the use of an ionophore, which forms a stable complex with the analyte of interest; an ion-exchanger, which provides electroneutrality and ensures permselectivity; and a polymer matrix which yields high support and mechanical functionality to the membrane. Non-invasive microelectrode ion flux estimation (MIFE) has been used to study the transport of ions in plant physiology due to the non-destructiveness and high spatial and temporal resolution of the method in almost natural conditions. Works by Miller *et.al* (Miller et al. 2001, Miller and Smith 1996) and Newman (Newman 2001, Newman et al. 1987) have pioneered the practical and versatile use of microelectrodes and MIFE for plant studies. Ions including H^+ , Ca^{2+} , NO_3^- , NH_4^+ , Na^+ , Cl^- , Cd^{2+} and K^+ have been investigated using MIFE techniques (Henriksen et al. 1992, Kochian et al. 1992, Pineros et al. 1998, Shabala et al. 1997). Nonetheless, these studies did not perform foliar uptake of zinc via ion flux estimation due to the lack of appropriate analytical tools. Further, these previous studies have employed a liquid-contact (LC) based platform for μ -ISEs (Henriksen et al. 1992, Kochian et al. 1992, Miller et al. 2001, Newman et al. 1987, Pineros et al. 1998, Shabala et al. 1997). However, the optimization and insertion of the backfilling solution can be laborious and challenging to yield lower limits of detection (LOD) and good electrode reproducibility. As a result, this work employs a solid-contact (SC) based platform to overcome the challenges from LC based platform. SC- μ -ISEs allow for less cumbersome LOD optimization due to its simplistic design. In a SC based platform, the ionophore-doped polymeric

membrane is in direct contact with the metallic conductor (e.g., gold) coated with a hydrophobic conducting polymer (poly (3-octylthiophene- 2,5 diyl)), leading to an improved membrane/metal interface and a stable phase boundary potential, allowing trace level analysis (Chumbimuni-Torres et al. 2006, Guth et al. 2009).

The objective of the present work was to develop, characterize, and apply a zinc SC- μ -ISE for determining *in situ* foliar uptake of Zn^{2+} in citrus plants using MIFE techniques. Two microelectrodes configurations were constructed to evaluate the selectivity, LOD, reproducibility and lifetime. Overall, the zinc SC- μ -ISE exhibited good stability and durability to monitor Zn^{2+} concentrations in the vascular bundle of citrus leaves *in-situ*.

Materials and Methods

Zinc Ion-Selective Membrane Cocktail

The Zn^{2+} cocktail was prepared by following a previously investigated composition with some modifications (Kojima and Kamata 1994). Zinc cocktail was prepared on a 100 mg scale that consists of 80 mmol/kg of Zn (I), 10 mmol/kg of KTFPB, (66.6 w%) o-NPOE and (33.3 w%) PVC, was dissolved in 1mL of THF and vortexed for 1 h.

Preparation of Zn^{2+} SC- μ -ISEs

Two configurations of zinc SC- μ -ISE were prepared using the zinc ion selective membrane cocktail described above. The configurations of the Zn^{2+} SC- μ -ISE are shown in Figure 6-1. The first configuration will be denoted as SC- μ -ISE 1 and the second configuration will be denoted as SC- μ -ISE 2.

The SC- μ -ISE 1 was prepared by employing a commercially available micropipette tip (0.540 mm diameter), where a gold wire (0.20 mm diameter) coated with POT was introduced

and sealed from the top with a hot melt adhesive. The zinc cocktail was inserted through capillary action and a round-like membrane formed at the end of the tip.

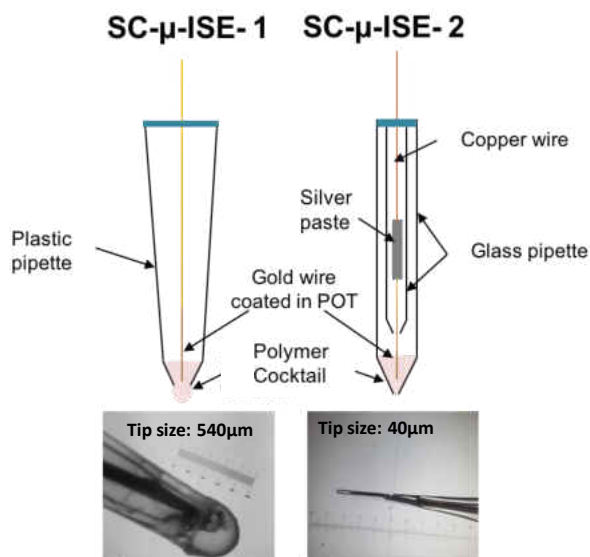


Figure 6- 1. Diagram and photograph of SC-μ-ISE 1 (left) and SC-μ-ISE 2 (right).

SC-μ-ISE 2 was prepared using borosilicate glass micropipettes (Sutter Instrument Company, BF120-69-15) (ID: 0.69 mm, OD: 1.2 mm, length: 15 cm), which were pulled horizontally using a Flame/Brown type micropipette puller (Sutter Instrument Company, Model P-100). The tip of the glass micropipette was broken with a fine tweezer to create a tip diameter between 30–100 μm and bevelled at a 45° angle using a beveller (BV-10, Sutter Instruments). The hydrophobic ion exchange membrane must adhere to the glass of the electrode to prevent the aqueous electrolyte solution from finding a pathway along the glass and short-circuiting the sensor (Beyenal 2013). Therefore, the glass inner surface was silanized to promote good adhesion with the hydrophobic membrane. Thus, the glass tip was dipped into TMSDMA for 15–30 sec. The micropipettes were then placed in a stainless steel mini-rack which was tightly closed by a glass container and placed in an oven at 180 °C for at least 24 hours. Then, the custom designed holder with the micropipette tips facing up was removed from the oven and a

small amount (0.25 ml) of dry TMSDMA was injected quickly into the small container using a syringe. The silanization reagent evaporated immediately and the vapor reached the inner surface of the micropipette tips. The glass container was then kept in the dark in a desiccator for 1.5–2 hours before applying the ion exchange membrane. The microelectrode tip was then dipped in the Zn^{2+} ion selective membrane cocktail for 10 sec and a 100 μm POT coated gold microelectrode was position within the membrane and held in place using hot melt adhesive before the membrane was allowed to dry. The POT coated gold microelectrode was prepared ahead of time by attaching a 100 μm gold wire to a copper wire using silver paste and encasing the gold wire in borosilicate glass using the micropipette puller.

The tip of the glass was broken to expose approx. 500 μm -length of gold wire which was coated with POT solution and allowed to dry for 2 hrs. After the SC- μ -ISE **2** was assembled and allowed to dry, the tip was observed under a microscope to insure the membrane had good contact with the POT coated gold electrode.

Characterization of Zn^{2+} SC- μ -ISEs

SC- μ -ISE **1** were conditioned in a 1×10^{-3} M $\text{Zn}(\text{NO}_3)_2$ solution for 5 hr. During measurement, the microelectrodes required a 20 min hydration time in DI water, followed by 8 min equilibration time upon analyte spiking. SC- μ -ISE **2** was conditioned in a more concentrated solution of 0.1M $\text{Zn}(\text{NO}_3)_2$ solution for 30 min to accelerate the condition time. SC- μ -ISE **2** was allowed to hydrate in DI water for 5 minutes, followed by 2 min equilibration time between analyte spiking.

Potentials for SC- μ -ISE **1** were monitored with a high-input impedance (1015 Ω) EMF-16 multichannel data acquisition system (Precision Electrochemistry EMF Interface, Lawson Laboratories, Malvern, PA) at room temperature (22° C), while stirring the solution.

All measurements were conducted in a Faraday cage to minimize electrical interference and measured against a double junction Ag/AgCl/3M KCl/1M LiOAc reference electrode (Metrohm AG). The SC- μ -ISE **1** was employed to determine pH stability and selectivity studies.

Determination of ion fluxes

Potentials for SC- μ -ISE **2** were monitored using a microsensor multimeter (Unisense A/S, Denmark) at room temperature under constant stirring. A Ag/AgCl reference electrode was used for all foliar uptake measurements. Net ion flux experiments were done after the leave/root had been exposed to Zn²⁺ solutions for 30 minutes. A custom flow cell (5 mL) was attached to the leaves of sour orange seedlings (Approx. 100 cm tall) as demonstrated in Figure 6-2. A 0.5 ml/min flow of Zn²⁺ solutions ranging from 0 to 15.3 mM was used to keep the system at equilibrium. The developed Zn²⁺ SC- μ -ISE **2** was positioned using a three-dimensional micromanipulator (UNISENSE A/S, Denmark) and observed using a stereomicroscope with a CCD camera (World Precision Instruments, Sarasota, FL). The Ag/AgCl reference electrode was fixed in the flow cell using a helping hand. Data acquisition software was used to control and record the microprofiles (Sensor Trace Pro, Unisense A/S, Denmark). The experiment took place in a Faraday cage to minimize electrical interference. The microelectrode tip was moved in a direction perpendicular to the leaf surface and microprofile measurements were taken at 50 μ m intervals from 1,000 to 50 μ m above the surface (to avoid breaking the sensor tip). A single profile was completed in 3 minutes (<10 s response time).

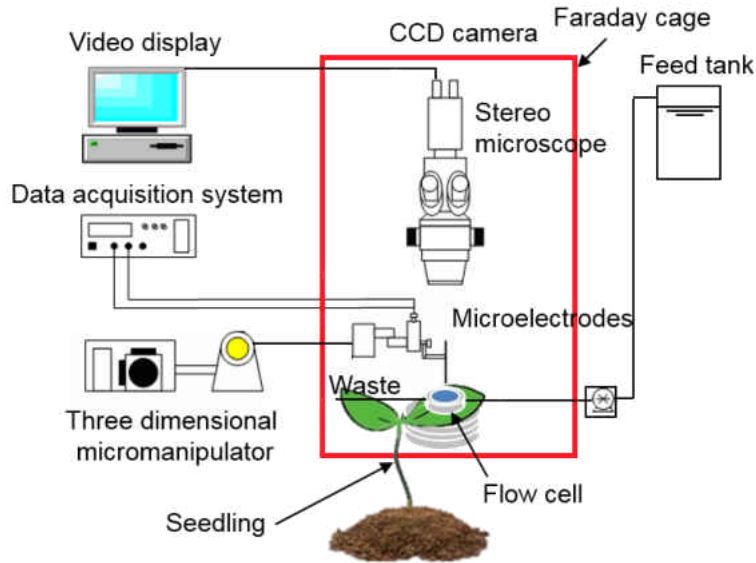


Figure 6- 2. Schematic diagram of microprofiling set-up for flux determination of zinc foliar/root uptake.

When ions are taken up by living cells, the concentration in the proximity of the cell's surface will be lower than that further away (Newman 2001). The conversion of concentration gradient data into flux estimate requires assumptions about the mechanisms of ion transport to the plant surface and the nature of the diffusion boundary layer (DBL) (Newman 2001). However, several studies have shown planar diffusion is mostly responsible for EMF gradients as a microelectrode approaches the surface of plant tissues (Henriksen et al. 1992, Shabala et al. 2000). Therefore, only planar diffusion will be considered in this study. If ordinary diffusion is the only driving force for ion movement toward a plant surface; Fick's First Law can be used to express the proportionality between flux and concentration gradient as shown in equation 6-1:

$$J_{Zn^{2+}} = \frac{D(C_1 - C_2)}{(X_1 - X_2)} \quad (6-1)$$

Where, J is the net Zn^{2+} flux (in picomoles per square centimeter per second), D is the diffusion constant for Zn^{2+} ($7.05 \times 10^{-6} \text{ cm}^2 \text{ s}^{-1}$) (Price et al. 1990), C_1 and C_2 are the measured Zn^{2+} concentrations at X_1 and X_2 , and X is the distance from the surface of the plant tissue. The minus sign is normally omitted for uptake measurements so that influx is defined as positive.

Results and Discussion

Sensor Characterization

The SC- μ -ISE **1** conditioning protocol was optimized to a minimum conditioning time of 5 hr in $1 \times 10^{-3} \text{ M Zn(NO}_3)_2$ yielding a Nernstian slope of $32.28 \pm 1.29 \text{ mV decade}^{-1}$ with a $(2.83 \pm 0.47) \times 10^{-7} \text{ M LOD}$ (Figure 6-3(a)), which resembles that of the macro-ion selective electrode platform previously investigated (Kojima and Kamata 1994). Thus size reduction did not hinder the electrodes ideal response. In a similar fashion, SC- μ -ISE **2** yielded a Nernstian response of $26.05 \pm 0.13 \text{ mV decade}^{-1}$ with an LOD of $(3.96 \pm 2.09) \times 10^{-7} \text{ M}$ (Figure 6-3(b)).

Given that the pH in phloem bundles in citrus plants is around 6.0 (Hijaz and Killiny 2014), the response of the sensor with fixed concentration of $Zn(NO_3)_2$ ($1 \times 10^{-3} \text{ M}$) at varied pH was investigated. The desired pH was achieved by adjusting with either HNO_3 or $NaOH$ (pH ranged from 2 to 9). The electrode exhibited a stable response between pH 4.00 to 7.00 as shown in Figure 6-4. Therefore, the proposed sensor is able to be used for MIFE analysis.

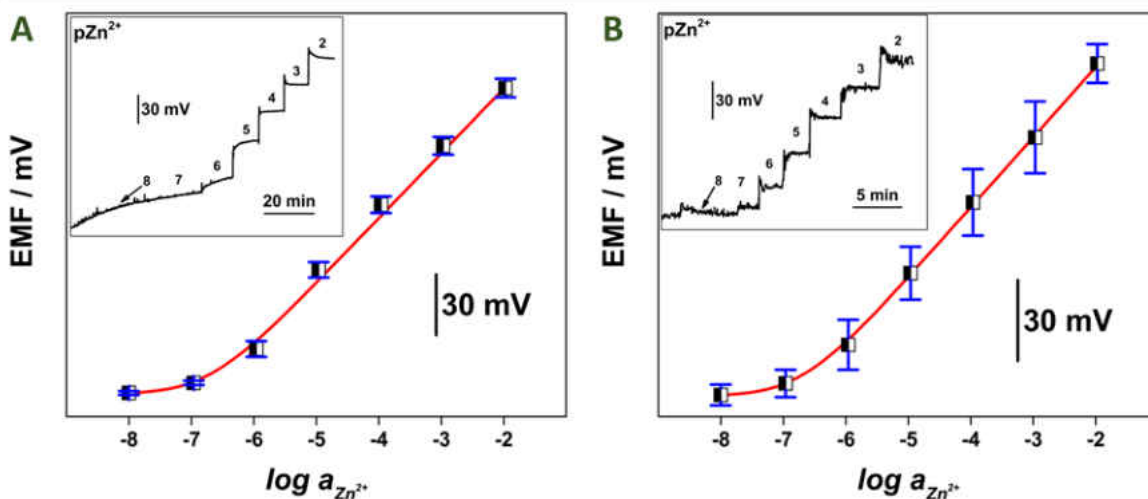


Figure 6- 3. Zn^{2+} calibration curves obtained with (A) SC- μ -ISE 1 and (B) SC- μ -ISE 2. (Inset: recorded potential time traces of respective SC- μ -ISEs). All measurements were done in triplicates

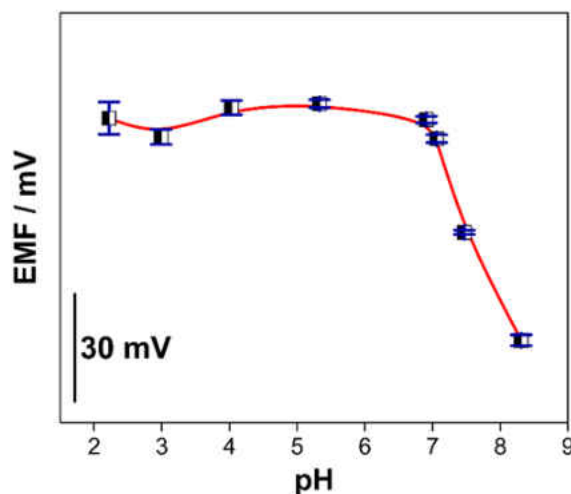


Figure 6- 4. pH stability study of Zn^{2+} SC- μ -ISE 1. Measurements were conducted in triplicates.

Selectivity measurements for Zn^{2+} ISEs were obtained using the unbiased separate solutions method as described by Bakker (Bakker 1997). Briefly, electrodes were conditioned in the least interfering ion to obtain Nernstian response, a requirement to use Nicolskii-Eisenman equation. The slopes and selectivity coefficients are displayed in Table 6-1. The selectivity coefficients reported in this work varies from previously reported literature [13], since unbiased

method was used. Nonetheless, the analysis of zinc foliar uptake is conducted through a surface profile and the inference caused by copper will be highly reduced. See Table 6-1.

Table 6- 1. Observed experimental selectivity coefficients for Zn²⁺ cocktail with corresponding slopes for interfering ions based on the unbiased separate solutions methods

Ion J ^(Z⁺) [a]	$\log K_{Zn,J}^{pot}$	Slope (mV decade ⁻¹)
Ca ²⁺	-3.15±0.07	27.10 ±0.53
K ⁺	2.13±0.17	52.58 ± 2.05
H ⁺	-0.52±0.13	51.39 ± 0.79
Cu ²⁺	10.82±0.61	38.95 ± 5.11
Zn ²⁺	0	27.78 ±1.23

Surface profiling

Foliar and Root Zn²⁺ uptake

The surface profiles of various Zn²⁺ concentrations on sour orange seedling leaves are shown in Figure 6-5(a). There was no detectable change in concentration from the bulk solution to the leaf surface when the bulk concentration was 0, 0.2, or 1.3 mM. This likely means that the concentration gradient between the internal leaf concentration and bulk concentration was not large enough to induce Zn²⁺ flux. When the concentration of the bulk solution was 6.0 mM, there was a decrease in concentration from the bulk to the surface of the leaf by 1.6 mM. This indicates the uptake of zinc by the leaves. This trend continues with higher bulk concentrations of Zn²⁺. When the measured bulk concentration was 15.2 mM, the surface concentration was reduced to 9.1 mM.

The surface profiles of Zn²⁺ uptake by the roots of a sour orange seedling are shown in Figure 6-5(b). It is clear that there is a significant difference between Zn²⁺ uptake by roots compared to leaves. Zn²⁺ concentrations averaging 6.3 mM and 12.6 mM in the bulk were both reduced to 0.2 mM at the surface of the leaves. The DBL was also significantly different between the surface profiles of the leave and the roots. For example, with a bulk concentration of 15.2

mM, the DBL of the leaf profile was 210 μm , yet with a similar bulk concentration (12.6 mM), the DBL of the root profile was increased to 274 μm . This may be due to the geometry of the roots. Unlike the leaves, the roots are round; therefore, a slight change in profiling location can lead to large changes hydrodynamics and mass transfer.

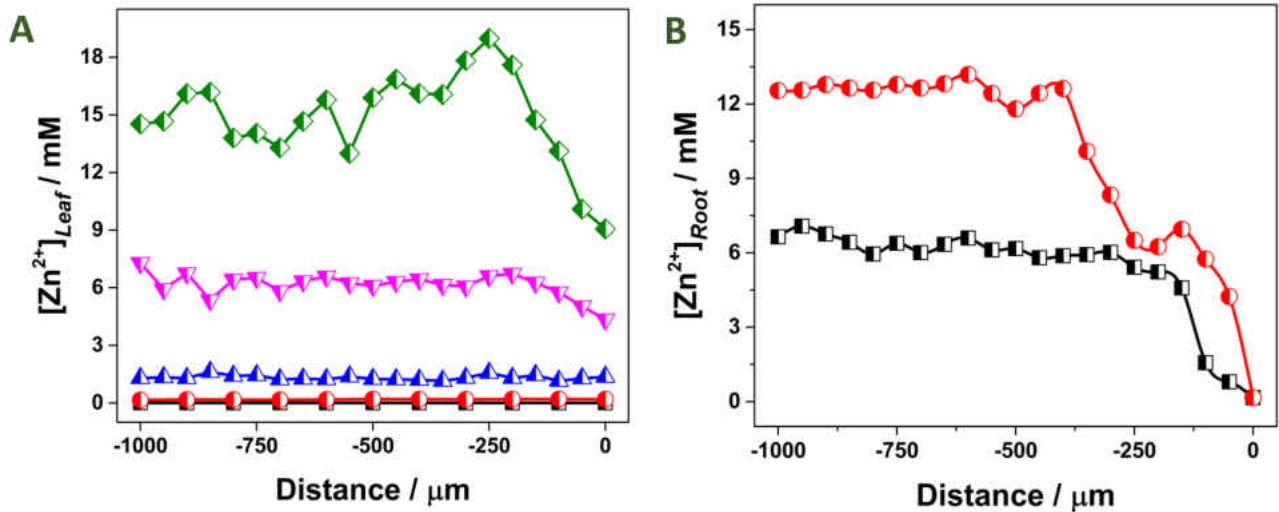


Figure 6- 5. Microprofiles of various Zn²⁺ bulk concentrations using SC- μ -ISE 2 on A) leaves and B) roots of sour orange seedlings. (On Figure 3A, black squares indicate 0 mM, red circles 0.20 mM, blue triangles 1.3 mM, pink triangles 6.0 mM, and green rhombus 15.2 mM Zn²⁺. On Figure 3B, black squares indicate 6.3 mM and red circles 13.0 mM Zn²⁺

Estimation of Zn²⁺ flux via MIFE

There is contradicting research on the uptake of Zn²⁺ in the leaves of plants. Some studies show that foliar uptake is possible in wheat plants (Haslett et al. 2001); while others report foliar uptake does not occur and can leave the roots starved of Zn²⁺ if not supplied in the root environment (Webb and Loneragan 1990). In this study, the flux of Zn²⁺ into the leaves and roots of a sour orange seedling was calculated from the surface profiles, as shown in Figure 6-6 and Table 6-2. There was no significant flux into the leaves when bulk concentrations were 0, 0.2, or 1.3 mM. This differs from a study by Haslett et al., where the foliar uptake of zinc (as ZnO and ZnEDTA) in wheat was observed at 1 μM concentrations of zinc. However, results in this study

demonstrate that when bulk concentrations increased to 6.0 and 15.2 mM, Zn^{2+} transport into the leaves was observed. The Zn^{2+} flux into the leaves ranged from $5.9 \times 10^2 \text{ nmol cm}^{-2} \text{ s}^{-1}$ to $1.7 \times 10^3 \text{ nmol cm}^{-2}$ for zinc concentrations of 6.0 and 15.2 mM, respectively. This shows that foliar zinc uptake is possible in sour orange leaves. Zn^{2+} flux of similar bulk concentrations was observed to be higher in the roots than compared to the leaves, indicating higher zinc uptake by the roots. The observed results were expected considering most nutrients are absorbed by the roots of plants (Gupta et al. 2016).

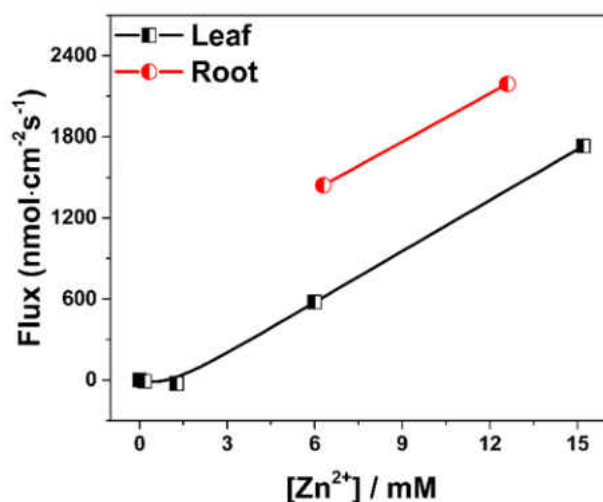


Figure 6- 6. Zn^{2+} flux as a function of bulk concentration in leaves and roots of sour orange citrus seedlings.

The flux of Zn^{2+} into the leaves had a linear relationship with bulk Zn^{2+} from 1.3 mM to 15.2 mM (Figure 6-6), suggesting passive diffusion. However, facilitated diffusion or active transport is also likely to be involved in Zn^{2+} uptake by plants (Jyung et al. 1965). In this case, we would expect to see a saturation point where all active sites are being consumed. Research by Zhang and Brown (Zhang and Brown 1999) looked at foliar Zn^{2+} uptake in Pistachio and Walnut leaves and found a saturation point at >7.5 mM and 15 mM in pistachio and walnut leaves,

respectively. Therefore, it is likely that there is a saturation point in citrus plants that is higher than 15.2 mM or that the initial uptake mechanism of Zn^{2+} is passive diffusion.

Table 6- 2. Estimated flux of Zn^{2+} into leaves of roots of sour orange seedlings using the developed SC- μ -ISE 2

Location	Zn^{2+} bulk concentration (mM)	Diffusion Boundary Layer (μm)	Flux ($\text{nmol cm}^{-2} \text{s}^{-1}$)
Leaf	0	N.D.	N.D.
Leaf	0.2	N.D.	N.D.
Leaf	1.3	N.D.	N.D.
Leaf	6.0	121	5.9×10^2
Leaf	15.2	210	1.7×10^3
Root	6.3	239	1.4×10^3
Root	12.6	274	2.2×10^3

Conclusion

A Zn^{2+} SC- μ -ISE was developed and characterized for the investigation of ion-transport processes in the foliage and roots of citrus plants. The sensor displayed a 26.05 ± 0.13 mV decade⁻¹ Nernstian response and a LOD of $(3.96 \pm 2.09) \times 10^{-7}$ M. Even though selectivity coefficients showed an interfering response to Cu^{2+} ($K_{Zn,J}^{pot} = 10.82 \pm 0.61$); Cu^{2+} concentrations were controlled in the flux estimation experiments. Therefore, Cu^{2+} interference was considered to be reduced. It was also found that the tip size, between 40 and 540 μm did not affect the response of the sensor.

Application of the developed Zn^{2+} SC- μ -ISE to the sour orange seedling revealed important information on zinc transport processes. It was found that Zn^{2+} flux is possible in citrus trees at bulk concentrations above 5.99 mM via MIFE. However, at low concentrations zero or negative flux was observed. Furthermore, the observed linear relationship between flux and bulk concentration, highlighting passive diffusion, may be a key mechanism for Zn^{2+} transport into plants.

Overall, this study is the first to develop a Zn^{2+} microelectrode for the determination of ion transport processes in plants. This novel tool can be used to further knowledge on the effect of nutrient therapy on HLB infected citrus plants.

References

- (1998) Handbook of Reference Methods for Plants Analysis, Taylor & Francis Group, Boca Raton, FL.
- Bakker, E. (1997) Determination of unbiased selectivity coefficients of neutral carrier-based cation-selective electrodes. *Analytical Chemistry* 69(6), 1061-1069.
- Beyenal, Z.L.H. (2013) Fundamentals of Biofilm Research, CRC Press Taylor & Francis Group.
- Bové, J.M. (2006) Huanglongbing: a destructive, newly-emerging, century-old disease of citrus. *Journal of Plant Pathology*, 7-37.
- Chumbimuni-Torres, K.Y., Rubinova, N., Radu, A., Kubota, L.T. and Bakker, E. (2006) Solid contact potentiometric sensors for trace level measurements. *Analytical Chemistry* 78(4), 1318-1322.
- Etxeberria, E., Gonzalez, P., Achor, D. and Albrigo, G. (2009) Anatomical distribution of abnormally high levels of starch in HLB-affected Valencia orange trees. *Physiological and Molecular Plant Pathology* 74(1), 76-83.
- Gottwald, T., Graham, J., Irej, M., McCollum, T. and Wood, B. (2012) Inconsequential effect of nutritional treatments on huanglongbing control, fruit quality, bacterial titer and disease progress. *Crop Protection* 36, 73-82.
- Gottwald, T.R. (2010) Current epidemiological understanding of citrus huanglongbing. *Annual Review of Phytopathology* 48, 119-139.
- Graca, J.d. (1991) Citrus greening disease. *Annual review of phytopathology* 29(1), 109-136.
- Gupta, N., Ram, H. and Kumar, B. (2016) Mechanism of Zinc absorption in plants: uptake, transport, translocation and accumulation. *Reviews in Environmental Science and Bio-Technology* 15(1), 89-109.
- Guth, U., Gerlach, F., Decker, M., Oelssner, W. and Vonau, W. (2009) Solid-state reference electrodes for potentiometric sensors. *Journal of Solid State Electrochemistry* 13(1), 27-39.
- Haslett, B.S., Reid, R.J. and Rengel, Z. (2001) Zinc mobility in wheat: Uptake and distribution of zinc applied to leaves or roots. *Annals of Botany* 87(3), 379-386.
- Henriksen, G.H., Raman, D.R., Walker, L.P. and Spanswick, R.M. (1992) Measurement of net fluxes of ammonium and nitrate at the surface of barley roots using ion-selective microelectrodes II. Patterns of uptake along the root axis and evaluation of the microelectrode flux estimation technique. *Plant Physiology* 99(2), 734-747.
- Hijaz, F. and Killiny, N. (2014) Collection and Chemical Composition of Phloem Sap from Citrus sinensis L. Osbeck (Sweet Orange). *PloS One* 9(7), 11.
- Jyung, W.H., Wittwer, S.H. and Bukovac, M.J. (1965) Role of Stomata in Foliar Absorption of Rb by Leaves of Tobacco Bean and Tomato. *Proceedings of the American Society for Horticultural Science* 86, 361
- Kim, J.-S., Sagaram, U.S., Burns, J.K., Li, J.-L. and Wang, N. (2009) Response of sweet orange (*Citrus sinensis*) to 'Candidatus Liberibacter asiaticus' infection: microscopy and microarray analyses. *Phytopathology* 99(1), 50-57.

- Kochian, L.V., Shaff, J.E., Kühtreiber, W.M., Jaffe, L.F. and Lucas, W.J. (1992) Use of an extracellular, ion-selective, vibrating microelectrode system for the quantification of K⁺, H⁺, and Ca²⁺ fluxes in maize roots and maize suspension cells. *Planta* 188(4), 601-610.
- Kojima, R. and Kamata, S. (1994) Zinc-Selective Membrane-Electrode Using Tetrabutyl Thiuram Disulfide Neutral Carrier. *Analytical Sciences* 10(3), 409-412.
- Miller, A.J., Cookson, S.J., Smith, S.J. and Wells, D.M. (2001) The use of microelectrodes to investigate compartmentation and the transport of metabolized inorganic ions in plants. *Journal of Experimental Botany* 52(356), 541-549.
- Miller, A.J. and Smith, S.J. (1996) Nitrate transport and compartmentation in cereal root cells. *Journal of Experimental Botany* 47(7), 843-854.
- Newman, I. (2001) Ion transport in roots: measurement of fluxes using ion-selective microelectrodes to characterize transporter function. *Plant, Cell & Environment* 24(1), 1-14.
- Newman, I.A., Kochian, L.V., Grusak, M.A. and Lucas, W.J. (1987) Fluxes of H⁺ and K⁺ in corn roots characterization and stoichiometries using ion-selective microelectrodes. *Plant Physiology* 84(4), 1177-1184.
- Nwugo, C.C., Lin, H., Duan, Y. and Civerolo, E.L. (2013) The effect of ‘Candidatus Liberibacter asiaticus’ infection on the proteomic profiles and nutritional status of pre-symptomatic and symptomatic grapefruit (*Citrus paradisi*) plants. *BMC Plant Biology* 13(1), 59.
- Pineros, M.A., Shaff, J.E. and Kochian, L.V. (1998) Development, characterization, and application of a cadmium-selective microelectrode for the measurement of cadmium fluxes in roots of *Thlaspi* species and wheat. *Plant Physiology* 116(4), 1393-1401.
- Price, W.E., Woolf, L.A. and Harris, K.R. (1990) Intradiffusion coefficients for zinc and water and shear viscosities in aqueous zinc (II) perchlorate solutions at 25. degree. *Journal of Physical Chemistry* 94(12), 5109-5114.
- Shabala, S., Babourina, O. and Newman, I. (2000) Ion-specific mechanisms of osmoregulation in bean mesophyll cells. *Journal of Experimental Botany* 51(348), 1243-1253.
- Shabala, S.N., Newman, I.A. and Morris, J. (1997) Oscillations in H⁺ and Ca²⁺ ion fluxes around the elongation region of corn roots and effects of external pH. *Plant Physiology* 113(1), 111-118.
- Tian, S., Lu, L., Labavitch, J.M., Webb, S.M., Yang, X., Brown, P.H. and He, Z. (2014) Spatial imaging of Zn and other elements in Huanglongbing-affected grapefruit by synchrotron-based micro X-ray fluorescence investigation. *Journal of experimental botany* 65(4), 953-964.
- Webb, M.J. and Loneragan, J.F. (1990) Zinc Translocation to Wheat Roots and Its Implications for a Phosphorus Zinc Interaction in Wheat Plants. *Journal of Plant Nutrition* 13(12), 1499-1512.
- Xia, Y., Ouyang, G., Sequeira, R.A., Takeuchi, Y., Baez, I. and Chen, J. (2011) A review of huanglongbing (citrus greening) management in citrus using nutritional approaches in China. *Plant Health Progress*.

Zhang, Q.L. and Brown, P.H. (1999) The mechanism of foliar zinc absorption in pistachio and walnut. *Journal of the American Society for Horticultural Science* 124(3), 312-317.

CHAPTER SEVEN: A NOVEL APPROACH FOR *IN SITU* MONITORING OF Zn²⁺ IN CITRUS PLANTS USING TWO-STEP SQUARE WAVE ANODIC STRIPPING VOLTAMMETRY

This paper has been previously published as: Church, J., and Lee, W.H. A Novel Approach for *In Situ* Monitoring of Zn²⁺ in Citrus Plants Using Two-Step Square Wave Anodic Stripping Voltammetry, MRS communications, 2018

Abstract

This study presents *in situ* detection of Zn²⁺ using a novel two-step square wave anodic stripping voltammetry (SWASV)-based needle-type microsensor for citrus plant applications. A double barrel bismuth/ platinum (Bi/Pt) microelectrode was fabricated with a solid metal tip (~110 μm) which was durable enough to penetrate the thick skin of the citrus leaves and sensitive enough to detect ppb changes in Zn²⁺ concentration using SWASV. The microelectrode tip size was also determined to reduce mass transport limitation and improve limit of detection (LOD). Overall, the developed Bi/Pt microelectrode successfully measured Zn²⁺ concentrations within the vascular bundle of citrus plants.

Introduction

In the span of 10 years, Huanglongbing (HLB) has devastated Florida's over 10-billion-dollar citrus industry (Hodges and Spreen 2006). Recent works on greenhouse canker infiltration assays showed local systemic activity of Zn-chelate (Commerford et al. 2016); however, there is no clear understanding of how the Zn-chelate moves in citrus trees. Although there are many analytical methods available for detecting Zn in aqueous solutions (e.g., inductively coupled plasma mass spectrometry [ICP-MS] and atomic absorption spectroscopy [AAS]), *in situ* monitoring of the movement of Zn-chelate in citrus trees has not been fully explored due to lack of experimental tools (Church et al.). There is an urgent need to develop a reliable Zn²⁺

monitoring tool, capable of tracking its systemic activity directly in plants. Successful *in situ* Zn^{2+} detection will lead to a better understanding of its potential fate in plants by estimating spatial and temporal phloem concentrations of Zn^{2+} between successive spray applications which will benefit the assessment of spray rate and timings for effective HLB management.

Microelectrodes are needle-type electrochemical microsensors that have been used for *in situ* monitoring of chemical compounds of interest in biofilm and corrosion processes in drinking water distribution systems (Lee et al. 2018, Lee et al. 2011b, Ma et al. 2018) and can be used to measure intracellular free ion activities by inserting their tip into plant tissues. Previous studies have shown the usefulness of applying ion selective microelectrodes to track the movement of H^+ , K^+ , NO_3^- and Na^+ in plants (Miller et al. 2001, Miller and Smith 1996, Newman 2001, Newman et al. 1987); however, it was found that Zn^{2+} ion selective electrodes show interference to Cu^{2+} (Church et al.), a common micronutrient found in plants. Furthermore, ion-selective microelectrodes are difficult to manufacture and can be easily broken when the glass tip comes in contact with hard surfaces. The microelectrode tip must be micro-scale to impale the phloem, but durable enough to penetrate the plant without breaking. Miller et al. (2001) reported only 9% of the originally prepared triple barreled electrodes working after plant impalement.

On the other hand, square wave anodic stripping voltammetry (SWASV) has been recognized as a powerful tool for measuring trace metals for decades (Wang et al. 2000) and can eliminate the need for fragile ion selective membranes used in ion selective electrodes. Metallic bismuth (Bi) electrodes have been used as a working electrode for the anodic stripping performance by forming amalgams with trace metals (Rehacek et al. 2014, Wang et al. 2000, Wang et al. 2001, Yi et al. 2012). SWASV using bismuth films have shown a limit of detection (LOD) of zinc reaching 12 ppb (Hwang et al. 2008). The enhanced sensitivity of SWASV,

associated with its pre-concentration step, makes it an ideal tool for measuring trace metals in biological matrices. However, conventional SWASV technique using a three-electrode system requires for stirring during the deposition step which is unsuitable for measurement of Zn^{2+} within the vascular bundle of citrus plants. In addition, the conventional three-electrode system needs to be miniaturized for plant applications. Here, we propose the use of a novel two-step SWASV technique where the pre-concentration step is conducted separately, *in situ*, using a combined Bi/Pt microelectrode electrode system before being transferred to a stripping solution and connected to a more sensitive three-electrode system. The use of microelectrodes in electroanalysis offers a number of advantages for *in situ* detection of Zn^{2+} in biological samples including low background current, low IR drop and enhanced mass transport rates (Bartlett et al. 2000). The last property is particularly important since it could alleviate the need for stirring during the pre-concentration step and allows *in situ* measurements in plants where the stirring condition is not possible. Even with the many advantages described previously, SWASV-based Zn^{2+} detection using microelectrodes has not yet been explored.

This study is the first to develop a novel technique for *in situ* detection of zinc in citrus plants by exploring a solid type of microelectrode for Zn^{2+} measurement using SWASV. Two innovative concepts were introduced to overcome challenges of *in situ* measurement of Zn^{2+} in plant. First, a low melting point bismuth alloy (Belmont Alloy 2451: 44.7% bismuth, 22.6% lead, 19.1% indium, 8.3% tin, and 5.3% cadmium, melting point 47°C) was tested as a way to eliminate the need for electrochemical co-deposition of bismuth traditionally used in SWASV detection of Zn^{2+} . Second, an *in vivo* pre-concentration step, before anodic stripping analysis was evaluated to minimize the invasiveness of the method by only using a two-electrode system for

pre-concentration before transferring to more sensitive three-electrode system for anodic stripping analysis.

Methods

Metallic bismuth microelectrode design and fabrication

Two different types of bismuth (Bi) microelectrodes were developed for Zn²⁺ detection using SWASV in this study. A single barrel bismuth microelectrode for testing the concept of two-step SWASV for detection of Zn²⁺ and a double barrel microelectrode consisting of bismuth (Bi) electrode as a working electrode and platinum (Pt) electrode as a reference electrode for real application to plant samples (Appendix E). The fabrication steps for a single barrel microelectrode can be found elsewhere (Lee et al. 2011a). Briefly, a micropipette (1B120-6, O.D. 1.2, I.D. 0.69, 150mm, WPI Inc. Sarasota, FL) was pulled using a Flaming/Brown type micropipette puller (Model P-1000, Sutter Instrument Co., Novato, CA). The tip of the micropipette was then broken using tweezers and tip diameter (6–85µm) was verified under a microscope. A piece (3 cm) of bismuth alloy wire (Belmont Alloy 2451: 44.7% bismuth, 22.6% lead, 19.1% indium, 8.3% tin, and 5.3% cadmium, melting point 47°C) was then inserted into the pulled micropipette and pushed toward the tip using a metal plunger. The alloy was heated using a nichrome heating filament (Cat. No. 66258-066, VWR, Radnor, PA). Pressure was applied using the plunger once the alloy began to melt to allow the alloy to pass through the tip of the micropipette. Any remnant of bismuth alloy at the tip of the microelectrode was removed by a gentle shake. A copper wire (12 cm, S4828C, 26GA, Fisher Scientific, Hampton, NH) was then fixed to the opposite end of the microelectrode by melting the alloy and inserting the wire. Next the tip of the micropipette was beveled at a 45° angle to expose the alloy wire using a micropipette beveller (BV-10, Sutter Instrument Co., Novato, CA). The tip was then rinsed with

deionized (DI) water and the finished microelectrode was preserved in a pipette storage box (BX20, Sutter Instrument Co., Novato, CA) until its use.

A double barrel microelectrode consisting of a Bi working electrode and a Pt reference microelectrode was fabricated using the same procedures described above but with a double barrel micropipette (2BF150-86-10, Sutter Instruments, Novato, CA). A Pt wire (99.99%) with a diameter of 100 μm (#100-896, California Fine Wire Co., Grover Beach, CA) was attached to a copper wire (12 cm, S4828C, 26GA, Fisher Scientific, Hampton, NH) using a silver conductive epoxy (8331-14G, MG chemicals, Ontario, Canada) and etched in 0.1M KCN with 1.2 V for 25–30 seconds to taper the tip. The Pt wire was then inserted into one barrel of the double barrel micropipette and the micropipette was pulled using the micropipette puller to seal the wire within the glass. The tip of the second barrel was broken and the bismuth alloy was formed at the tip of the microelectrode using the steps described for a single barrel microelectrode fabrication.

Microelectrode performance evaluation using SWASV

To apply the developed double barrel microelectrode to the plant system, the traditional SWASV was modified with two-step approach of *in situ* deposition and *ex situ* anodic stripping (Fig. 7-1). First, Zn^{2+} was deposited on the bismuth microelectrode in a solution of Tris buffer (pH ranged from 5.0 to 7.5) with varying concentrations of ZnCl_2 (0–300 ppm Zn^{2+}) to represent the plant environment. Using a two-electrode system, a deposition potential of -1.4V vs. platinum reference electrode was applied to the bismuth microelectrode for 180 seconds both under stirred and unstirred conditions. The microelectrodes were then removed, rinsed with DI water, and transferred to a stripping solution (unstirred) where a SWASV scan (Scan: -1.4V to -0.4V; Step: 10mV; Amplitude: 40mV; Frequency; 5 Hz) was applied using a potentiometer (Palmsens³, Palmsens BV, Netherlands) to determine Zn^{2+} concentration. During the square

wave scan, a platinum mesh was used as a counter electrode and an Ag/AgCl electrode (MI-401, Microelectrode Inc., Bedford, NH) was used as a reference electrode. After the scan, the microelectrode was cleaned in the same solution by applying -0.4V for 30 seconds.

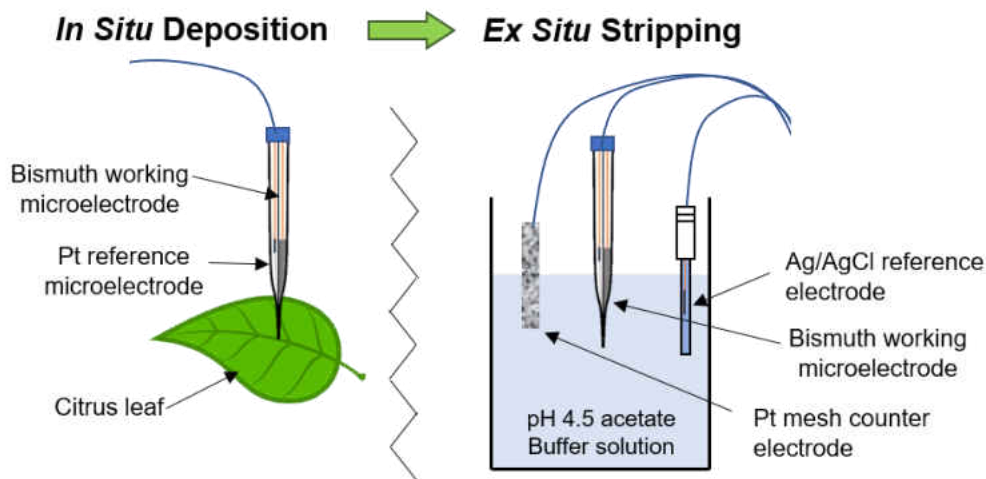


Figure 7- 1. A concept diagram of the two-step SWASV determination of Zn²⁺ in the vascular bundle of citrus plants.

In situ application to citrus leaves

Before applying the developed Bi/Pt microelectrode to citrus leaves, sample leaves were collected from a sour orange seedling and introduced to a 1 mM solution of ZnCl₂ by submerging the stem of the leaf into the solution for 6 hours. Control samples were exposed to DI water for 6 hours. The surfaces of all leaves were then rinsed with DI water and wiped dry with a Kimwipe. An automatic three-dimensional (3D) micromanipulator (UNISENSE A/S, Denmark) was used to position the tip of the combined Bi/Pt microelectrode 400 μm below the surface of the midrib for the *in situ* deposition of Zn²⁺. Preliminary results of pH microprofiles and cross-sectional images (Appendix E) suggested that approximate 300–400μm would be a typical depth for the phloem in citrus seedlings. Local *in situ* pH measurement were conducted using a pH microsensor (10 μm tip diameter, UNISENSE A/S, Denmark) and the 3D micromanipulator

(UNISENSE A/S, Denmark). After Zn^{2+} deposition on Bi side of the Bi/Pt microelectrode, the microelectrode was removed, rinsed with DI water, and transferred using the automatic 3D manipulator to the anodic stripping solution (0.1M acetate buffer at pH 4.5). A stereomicroscope with a CCD camera (World Precision Instruments, Sarasota, FL) was used to monitor the location of the microelectrode tip during the movement steps. SWASV scans were produced using a potentiometer (Palmsens³, Palmsens BV, Netherlands) with the same parameters used in the calibration. All experiments were performed in a Faraday cage (81-334-04, Technical Manufacturing Co., Peabody, MA) to avoid electrical interference. Pre- and post-calibration was conducted for ensuring the sensor performance.

Results and discussion

Zn^{2+} detection using two-step SWASV

The remarkable sensitivity of anodic stripping analysis is attributed to the coupling of an efficient pre-concentration step with a sensitive voltammetric stripping measurement of accumulated metals. For conventional SWASV measurements, the pre-concentration and stripping steps occur in the same solution; however, this is not suitable for *in situ* detection in citrus trees. To minimize the impact of continuous SWASV measurements within the vascular bundle of citrus plants, the pre-concentration step needs to be conducted separately, *in situ*, using a combined two-electrode system before being transferred to a stripping solution and connected to a more sensitive three-electrode system. This two-step process was evaluated using a Bi microelectrode and compared with traditional SWASV measurements. For the conventional measurements, both the deposition step and stripping steps took place in a pH 4.5 acetate buffer solution (0.1 M) using a Pt mesh counter electrode and an Ag/AgCl reference electrode. For the

modified two-step measurement used in this study, deposition was performed in a separate Zn^{2+} solution (Tris buffer+ $ZnCl_2$), simulating the plant system, before being transferred to a pH 4.5 acetate buffer where stripping occurred.

Figure 7-2 shows the difference in response between the two methods. For the conventional SWASV measurement, a Zn^{2+} peak height of 0.022 μA was observed for 200 ppm Zn^{2+} . This is significantly larger than the 0.009 μA peak height for the two-step SWASV method using the same Bi microelectrode. However, it was found that both methods were able to demonstrate a linear response between 1 and 200 ppm Zn^{2+} . While the conventional SWASV measurement showed higher sensitivity to Zn^{2+} (101 pA/ppm vs. 38 pA/ppm), the two-step method was also able to measure Zn^{2+} concentrations of interest with an excellent linear response ($R^2=0.990$). This result is the first to show that the two-step SWASV method can work in plants systems.

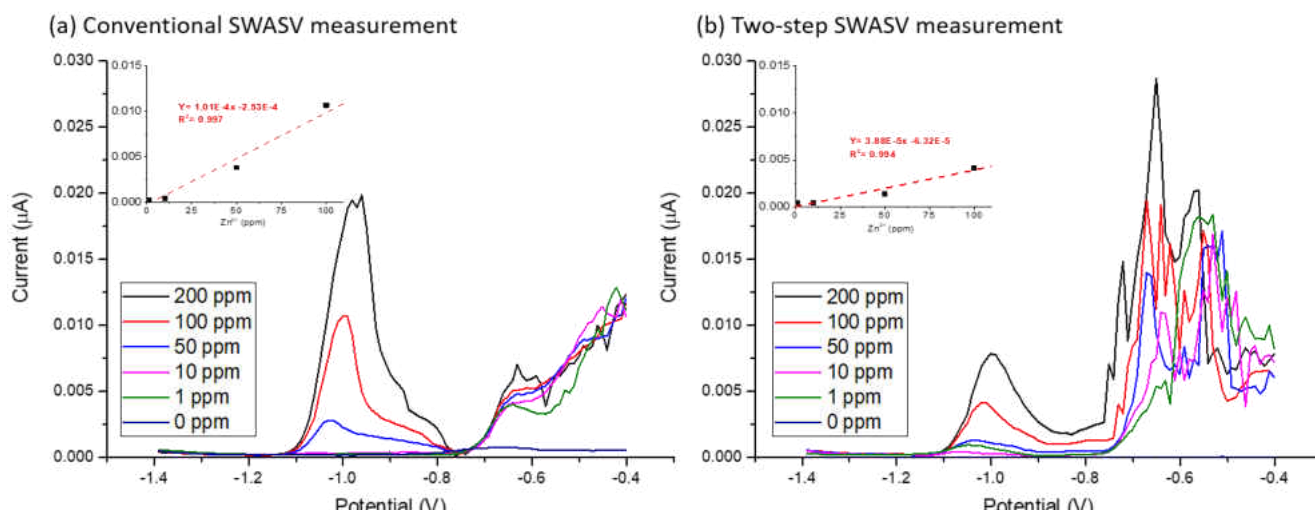


Figure 7- 2. SWASV responses of the developed Bi microelectrode (tip size: 6 μm in diameter) to various Zn^{2+} concentrations (1–200 ppm) between (a) a conventional method: deposition (stirred) and stripping (unstirred) in pH 4.5 acetate buffer and (b) a two-step SWASV method: deposition (unstirred) in $ZnCl_2$ solution and stripping (unstirred) in pH 4.5 acetate buffer at 23°C. Insets: Calibration curves from 1-100 ppm Zn^{2+} .

Effect of plant pH on microelectrode response

The effect of plant pH was investigated over the pH range of 5.0 to 7.5, under a fixed concentration of 200 ppm Zn^{2+} in DI water, using the two-step SWASV method (Fig. 7-3). pH was adjusted using HCl and NaOH. This pH range is typical for the vascular bundle of citrus plants (Hijaz and Killiny 2014) and was also determined using a pH microsensor in this study (Appendix E). The largest response was obtained at the lowest pH (5.0) with 1.78 μA ; however, the responses between pH 5 and 6.5 were comparable and ranged from 1.40 to 1.78 μA . At pH 7.0 the response to Zn^{2+} decreased significantly by 63% with a 0.66 μA peak and the response at pH 7.5 was < 1% of the electrode signal for pH 5.0. This decrease in response with increasing pH is accordance with the change of Zn^{2+} species depending on pH in aqueous solution. Using a water chemistry modelling software (MINEQL), it was confirmed that the solubility of Zn^{2+} decreases as pH increase above 7.2. Therefore, it is likely that the developed SWASV microelectrode is responding to the soluble concentration of Zn^{2+} across the tested pH range and that when pH was increased to 7.5 there was only a small amount of soluble Zn^{2+} to detect. Considering that the pH of the vascular bundle is expected to be below pH 7, it is likely that majority of the zinc would be detected by the developed two-step SWASV method using a Bi/Pt microelectrode.

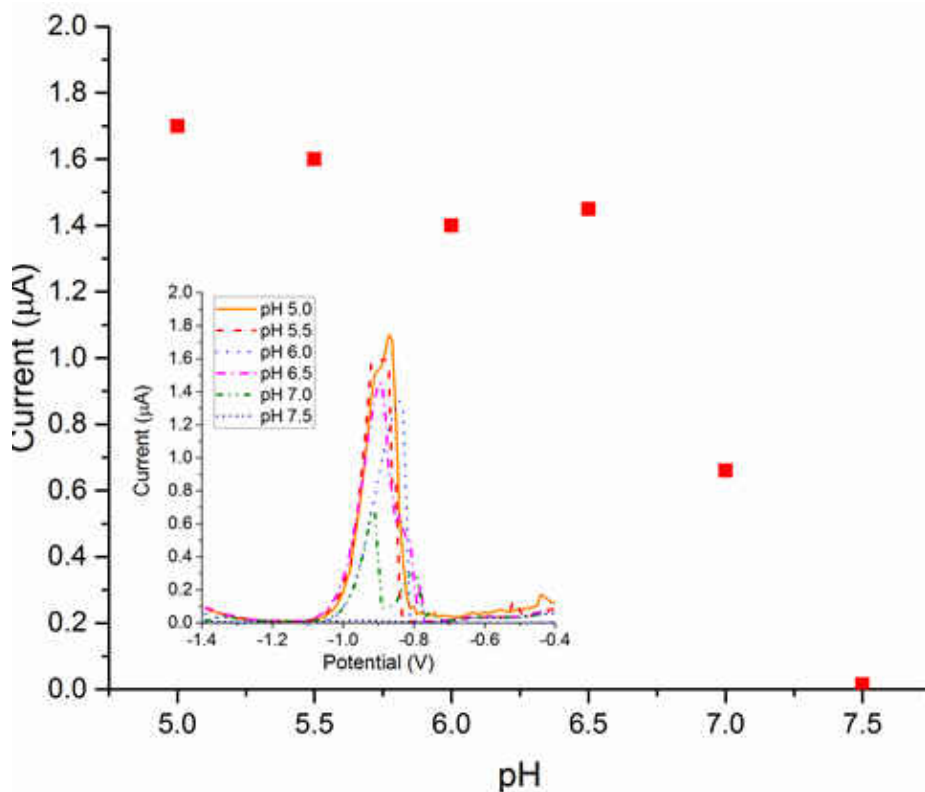


Figure 7- 3. pH effect on SWASV responses to Zn^{2+} concentrations during pre-concentration (inset: SWASV voltammogram of the Bi microelectrode with various pre-concentration pH values).

Effect of tip size and mass transfer on SWASV response

The response of SWASV to Zn^{2+} concentrations is partly related to the surface area of the working electrode. Therefore, the effect of microelectrode tip size was investigated to optimize the developed Bi microelectrode for application to citrus plants. The ideal tip size would be small enough to penetrate the phloem, but large enough to produce distinguishable SWASV responses to different Zn^{2+} concentrations. Figure 7-4(a) shows the calibration curves of the developed Bi microelectrode with different tip sizes ranging from 10 to 85 μm (Appendix E). As expected, larger tip sizes increase the sensitivity of the SWASV response. For example, the 85 μm tip size had an increased slope, 0.154 $\mu A/ppm Zn^{2+}$, compared to the 10 μm tip size which only had a slope of 0.0012 $\mu A/ppm Zn^{2+}$. The sensors displayed similar sensitivities per unit surface area

with an average normalized sensitivity of $1,246 \pm 285 \mu\text{A/ppm Zn}^{2+}$ per cm^2 . Under stirred conditions, the $85 \mu\text{m}$ tip displayed a LOD below 0.65 ppm Zn^{2+} , while the smaller tip size (e.g., $10 \mu\text{m}$) had a higher LOD (e.g., $\sim 11 \text{ ppm Zn}^{2+}$). The recess of the microelectrode shows no significant effect on the electrode response under stirred conditions (Table 7-1).

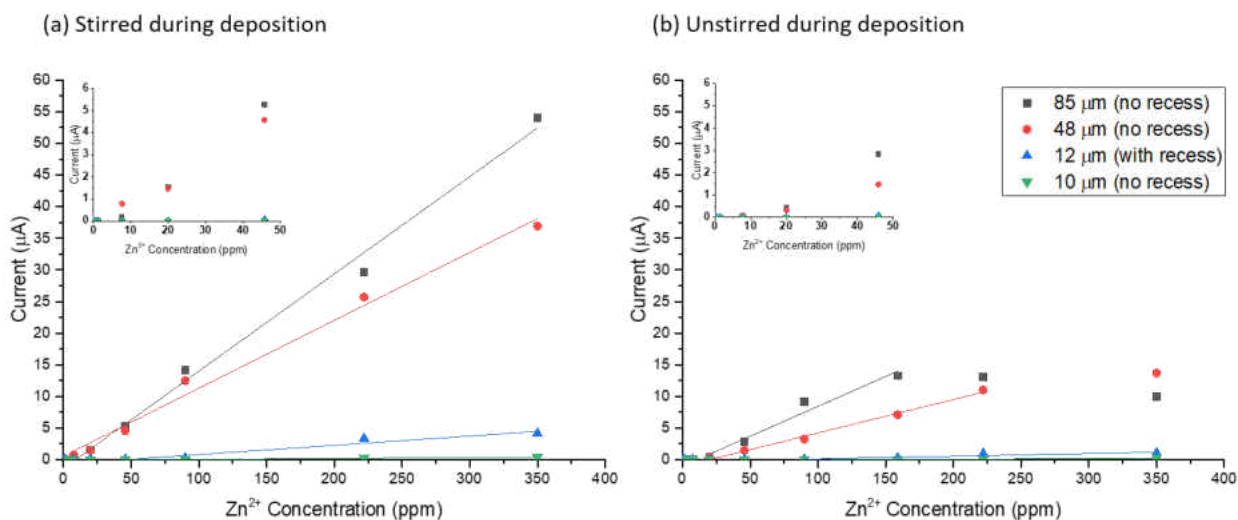


Figure 7- 4. Mass transfer effect on Zn^{2+} detection: Zn^{2+} SWASV calibration curves of various tip sizes of Bi microelectrodes under (a) stirred and (b) unstirred conditions during a deposition step. Insets: Expanded view of sensor response from 0 to 50 ppm Zn^{2+} .

The effect of mass transfer on SWASV response was also investigated (stirred vs. unstirred). Conventional SWASV measurements use stirring during the deposition step to increase mass transport of target heavy metal ions to the electrode; however, under unstirred conditions, which simulate inside the vascular bundle of citrus plants, the reduced mass transport may be a limiting factor during *in situ* deposition of Zn^{2+} . Figure 7-5(b) shows the calibration curves of various microelectrode tip sizes under unstirred conditions. The slope and LOD is severely affected under unstirred conditions for the 85 , 48 and $12 \mu\text{m}$ tip sizes. There was a 3,440%, 1,710%, 500% and 80% increase in the LOD for the 85 , 48 , 12 and $10 \mu\text{m}$ tip sizes, respectively. Similarly, the linear range also decreased for the 85 and $48 \mu\text{m}$ tip sizes probably

due to mass transport limitations, but stayed the same for 12 and 10 μm tip sizes between stirred and unstirred conditions. Table 7-1 compares the slope, linear range, and LOD between stirred and unstirred conditions. These results show that there is lesser effect of mass transport limitations on smaller sizes, compared to larger tip sizes. It is also clear that the recess enhances the effect of stirring on the sensor response. For example, the LOD of the 12 μm sensor with a recess was decreased by 500% when there was no stirring during the deposition, but a similarly sized sensor (10 μm) without a recess did not show a significant decrease in LOD. These findings agree with other literature (Bartlett et al. 2000) and is particularly important since microelectrodes with a smaller tip sizes could alleviate the need for stirring during the pre-concentration step and allow *in situ* measurements. Overall, a bismuth tip size in the range of 45–90 μm (as a working electrode) was used for the biological application to minimize mass transport interference and maximize LOD and slope.

Table 7- 1. The effect of tip size on the mass transport interference of SWASV response to Zn^{2+} using the developed Bi microelectrode

Parameter and condition		85 μm (without recess)	48 μm (without recess)	12 μm (with recess)	10 μm (without recess)
Slope ($\mu\text{A/ppm Zn}^{2+}$)	Stirred	0.1537	0.1073	0.0147	0.0012
	Unstirred	0.0945	0.0527	0.0041	0.0011
	% change	38%	50%	72%	8.3%
LOD* (ppm Zn^{2+})	Stirred	<0.65	1.27	7.71	11
	Unstirred	13.5	23	46.2	19.9
	% change	-3440%	-1710%	-500%	-80%
Linear range (ppm Zn^{2+})	Stirred	>350 to <0.65	>350 to 1.27	>350 to 7.71	>350 to 19.9
	Unstirred	145.4 to 13.5	268.3 to 23.0	>350 to 46.2	>350 to 19.9
	change	Decrease	Decrease	Decrease	Same

In situ detection of Zn^{2+} using SWASV in the vascular bundle of citrus plants

The combined Bi/Pt microelectrode was applied for Zn^{2+} detection in the vascular bundle of citrus plants. The configuration of the double barrel microelectrode allowed for simultaneous penetration of the working and reference electrode into the vascular bundle of citrus leaves for SWASV determination of Zn^{2+} . The combined Bi/Pt microelectrode showed improved durability over the single barrel Bi microelectrode and was not damaged by the leaf surface. The double barrel Bi/Pt microelectrode had an overall tip diameter of 110 μm and a working bismuth diameter of 70 μm . A calibration curve showed an excellent sensitivity toward Zn^{2+} with 0.172 $\mu A/ppm Zn^{2+}$ slope and an R^2 value of 0.996 (Fig 7-5(a)). The calibration curve after application to the plant showed a response of 0.187 $\mu A/ppm Zn^{2+}$ and demonstrated that the microelectrode was not damaged during the penetration. By microscopic observation, it was also found that the direct contact with plant tissue had no impact on the microelectrode tip. The pre- and post-calibration curves (Fig. 7-5(a)) also showed a LOD of 0.92 ppm and a life time study showed the sensor's response does not change over 18 uses (Appendix E) which is acceptable for the purpose of detection of Zn^{2+} in plants.

Figure 7-5(b) shows the microelectrode's response to Zn^{2+} concentrations in the midrib of treated (1 mM $ZnCl_2$ for 6 hrs) and untreated (DI for 6 hrs) citrus leaves. The two separate treated leaves (1 and 2) produced a SWASV response of 1.2 μA (treated 1) and 1.4 μA (treated 2) and the two separate untreated leaves showed a negligible response (0.06 μA and 0.003 μA) to Zn^{2+} compared to the treated leaves. Using the pre-and post-calibration curves (Fig. 7-5(a)), it was determined that the treated leaf contained 5.73 ± 0.88 ppm Zn^{2+} while the untreated leaf contained undetectable amounts of Zn^{2+} . While the increase in Zn^{2+} concentration was expected in the treated leaf, the measured values were difficult to validate with existing literature due to

the use of different analytical methods. Most studies primarily detect Zn^{2+} using inductively coupled plasma atomic emission spectroscopy (ICP-AES) or atomic absorption spectroscopy (AAS) for which samples need to be dried, grounded, and digested before analysis (1998). This causes zinc concentrations being reported in mg per kg dry weight. A study using a more direct Zn measurement, micro X-Ray Fluoresce (μ -XRF), reported Zn^{2+} concentrations in $mg\ kg^{-1}$ dry weight (34.6 to 42.4 $mg\ kg^{-1}$ in sour orange plants) (Tian et al. 2014). Considering μ -XRF determines total zinc concentration and there will be a difference between dried ($mg\ Zn\ kg^{-1}$ biomass) and *in situ* measurements ($mg\ Zn^{2+}\ L^{-1}$), the measurement using *in situ* SWASV seems reasonable.

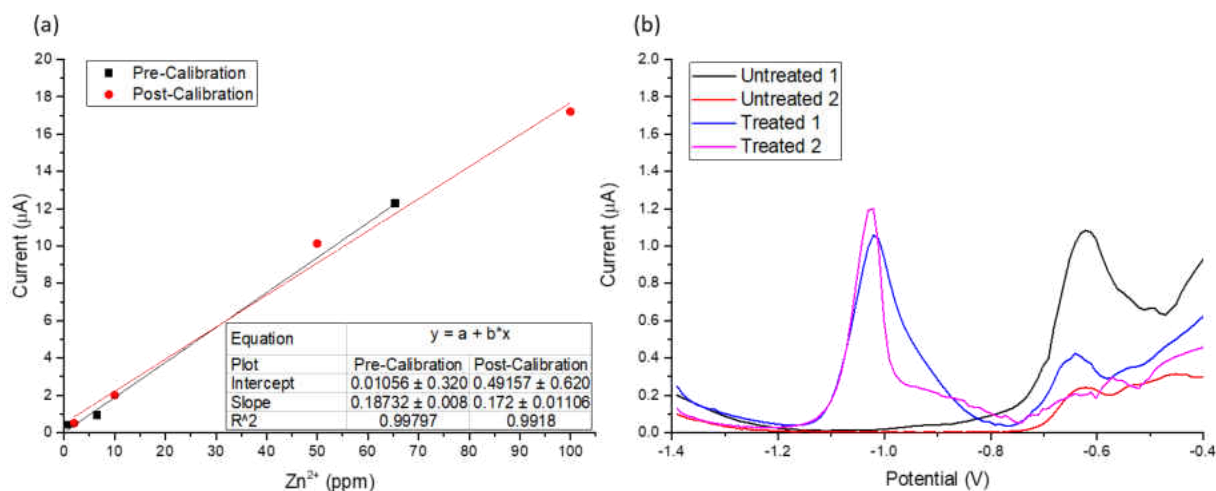


Figure 7- 5. In situ application of the developed microelectrodes for plants. (a) Pre- and post-calibration curves of combined bismuth/Pt reference microelectrode using a two-step SWASV method. (b) In situ detection of Zn^{2+} in untreated (DI water) and treated (1 mM $ZnCl_2$) citrus leaves using the double barrel Bi/Pt microelectrode.

While the benefits of using a SWASV-based microelectrode for monitoring Zn^{2+} concentrations in citrus plants are clear, there are still limitations that need to be addressed. In particular, Cu-Zn intermetallic species are known to develop during the deposition step and interfere with the sensor response (Sanna et al. 2000). However, the quantification of the interference from intermetallic Cu-Zn compounds is beyond the scope of this paper, as it is

assumed that Cu^{2+} concentrations in citrus leaves will be significantly lower than Zn^{2+} (Sanna et al. 2000). For other applications where both Zn^{2+} and Cu^{2+} exists in high concentrations, we suggest that one possible solution for determining the amount of copper in a sample would be to use a different deposition potential (e.g., -0.6 V) that is more anodic than that required for the reduction of Zn^{2+} to determine if the formation of Cu-Zn compounds may be a problem for sensor responses. With more validation regarding reproducibility and representativeness, it is expected that this novel approach of using two-step SWASV would provide a simple, fast and reproducible detection of Zn^{2+} in plants, capable of distinguishing between treated and untreated samples. Overall, this study demonstrates the feasibility of using a SWASV-based microelectrode technique as a direct and rapid method for monitoring of Zn^{2+} concentration in phloem tissue in a minimally invasive way.

Conclusions

A metallic bismuth (Bi)-based microelectrode was constructed and tested for concept proof of two-step SWASV for detecting Zn^{2+} . We were able to demonstrate to feasibility of a two-step SWASV measure using *in situ* deposition of Zn^{2+} and *ex situ* stripping. It was also found that the tip size can be optimized to reduce mass transport limitation and improve LOD. The Bi microelectrode was then combined with a platinum microelectrode in a double barrel microelectrode configuration for direct measurement of Zn^{2+} in plants. Our results showed that the solid metal tip (110 μm in diameter) of the Bi/Pt microelectrode is durable enough to penetrate the thick skin of the citrus leaves. Overall, the developed Bi/Pt microelectrode was able to respond to Zn^{2+} in the midrib of a citrus leaves and distinguish the Zn^{2+} concentrations between Zn^{2+} treated and untreated samples with high resolution. This novel *in situ* detection method, capable of tracking its systemic Zn^{2+} activity directly in plants will lead to better

understanding of its potential fate in plants for effective HLB management in agriculture industry.

References

- (1998) Handbook of Reference Methods for Plants Analysis, Taylor & Francis Group, Boca Raton, FL.
- Bartlett, P.N., Denuault, G. and Sousa, M.F.B. (2000) A study of the preconcentration and stripping voltammetry of Pb (II) at carbon electrodes. *Analyst* 125(6), 1135-1138.
- Church, J., Armas, S.M., Patel, P.K., Chumbimuni-Torres, K. and Lee, W.H. Development and Characterization of Needle-Type Ion-Selective Microsensors for in situ Determination of Foliar Uptake of Zn²⁺ in Citrus Plants. *Electroanalysis*.
- Commerford, S., Gerberich, K., Rajasekaran, P., Young, M., Das, S., Graham, J., Santra, S. and Johnson, E. (2016) Citrus Canker as a bioassay for systemic bactericidal activity of Zinc nanoparticles, pp. 62-62, AMER PHYTOPATHOLOGICAL SOC 3340 PILOT KNOB ROAD, ST PAUL, MN 55121 USA.
- Hijaz, F. and Killiny, N. (2014) Collection and chemical composition of phloem sap from Citrus sinensis L. Osbeck (sweet orange). *PloS one* 9(7), e101830.
- Hodges, A.W. and Spreen, T.H. (2006) Economic impacts of citrus greening (HLB) in Florida.
- Hwang, G.H., Han, W.K., Park, J.S. and Kang, S.G. (2008) Determination of trace metals by anodic stripping voltammetry using a bismuth-modified carbon nanotube electrode. *Talanta* 76(2), 301-308.
- Lee, W.H., Lee, J.-H., Choi, W.-H., Hosni, A.A., Papautsky, I. and Bishop, P.L. (2011a) Needle-type environmental microsensors: design, construction and uses of microelectrodes and multi-analyte MEMS sensor arrays. *Measurement Science and Technology* 22.
- Lee, W.H., Pressman, J.G. and Wahman, D.G. (2018) Three-dimensional Free Chlorine and Monochloramine Biofilm Penetration: Correlating Penetration with Biofilm Activity and Viability. *Environmental Science & Technology*.
- Lee, W.H., Wahman, D.G., Bishop, P.L. and Pressman, J.G. (2011b) Free chlorine and monochloramine application to nitrifying biofilm: comparison of biofilm penetration, activity, and viability. *Environmental Science and Technology* 45, 1412-1419.
- Ma, X., Armas, S.M., Soliman, M., Lytle, D.A., Chumbimuni-Torres, K.Y., Tetard, L. and Lee, W.H. (2018) In situ monitoring of Pb²⁺ leaching from the galvanic joint surface in a prepared chlorinated drinking water. *Environmental Science & Technology*.
- Miller, A.J., Cookson, S.J., Smith, S.J. and Wells, D.M. (2001) The use of microelectrodes to investigate compartmentation and the transport of metabolized inorganic ions in plants. *Journal of Experimental Botany* 52(356), 541-549.
- Miller, A.J. and Smith, S.J. (1996) Nitrate transport and compartmentation in cereal root cells. *Journal of Experimental Botany* 47(7), 843-854.
- Newman, I. (2001) Ion transport in roots: measurement of fluxes using ion-selective microelectrodes to characterize transporter function. *Plant, Cell & Environment* 24(1), 1-14.

Newman, I.A., Kochian, L.V., Grusak, M.A. and Lucas, W.J. (1987) Fluxes of H⁺ and K⁺ in corn roots characterization and stoichiometries using ion-selective microelectrodes. *Plant Physiology* 84(4), 1177-1184.

Rehacek, V., Hotovy, I. and Vojs, M. (2014) Bismuth Film Voltammetric Sensor on Pyrolyzed Photoresist/Alumina Support for Determination of Heavy Metals. *Electroanalysis* 26(5), 898-903.

Sanna, G., Pilo, M.I., Piu, P.C., Tapparo, A. and Seeber, R. (2000) Determination of heavy metals in honey by anodic stripping voltammetry at microelectrodes. *Analytica Chimica Acta* 415(1), 165-173.

Tian, S., Lu, L., Labavitch, J.M., Webb, S.M., Yang, X., Brown, P.H. and He, Z. (2014) Spatial imaging of Zn and other elements in Huanglongbing-affected grapefruit by synchrotron-based micro X-ray fluorescence investigation. *Journal of experimental botany* 65(4), 953-964.

Wang, J., Lu, J., Hocevar, S.B., Farias, P.A. and Ogorevc, B. (2000) Bismuth-coated carbon electrodes for anodic stripping voltammetry. *Analytical chemistry* 72(14), 3218-3222.

Wang, J., Lu, J., Kirgöz, Ü.A., Hocevar, S.B. and Ogorevc, B. (2001) Insights into the anodic stripping voltammetric behavior of bismuth film electrodes. *Analytica chimica acta* 434(1), 29-34.

Yi, W.J., Li, Y., Ran, G., Luo, H.Q. and Li, N.B. (2012) Determination of cadmium (II) by square wave anodic stripping voltammetry using bismuth–antimony film electrode. *Sensors and Actuators B: Chemical* 166, 544-548.

CHAPTER EIGHT: CONCLUSIONS, IMPACTS, AND OUTLOOK

Conclusions

Microsensors are powerful and nondestructive tools for quantifying interfacial reactions at the microscale in aquatic systems. They provide information that cannot be obtained by bulk solution measurements. Their small tip size and the capability of measuring compounds in high spatial and temporal resolution are vital for determining (time-course) mass transport of chemicals of interest which is needed for understanding many engineering systems. The work presented in this dissertation has demonstrated the unique contribution of microelectrodes in several environmental engineering research areas.

First, we demonstrated that microsensors can be used to characterize mixed biofilms grown in a novel microalgal-based treatment system where DO microsensors were used to quantify the photo-aeration by an algal biofilm present on top of a nitrifying biofilm. Ammonia microprofiles also demonstrated that there was no consumption of ammonia in the upper portion of the biofilm, indicating that the algal portion of the upper biofilm was not consuming ammonia. Hence, the role of algal biofilm in the MAIFAS reactor is mostly aiding photo-oxygenation. Overall, this study demonstrated microalgae photosynthesis as a way to provide sufficient oxygen for advanced wastewater treatment (>99% ammonia and 51% P removal in the MAIFAS reactor) and represents a novel strategy for reducing energy costs while meeting stringent effluent standards.

Second, we applied the pH, DO, and ORP microsensors to bilge water emulsions to demonstrate the relationship between mass transfer and emulsion stability over time. Microsensor characterization of emulsions proved to be a useful tool for *in situ* monitoring mass transfer across and oil-water interface and thus act as an excellent predictor of Marangoni

stabilities when combined with surface tension and particle size analyses. The study showed that emulsions stabilized with nonionic surfactants were, in general, more unstable than SDS stabilized emulsions. However, SDS emulsions were more susceptible to salinity than Triton X-100 emulsions. Furthermore, mass transfer in SDS emulsions were more affected by salinity than Triton X-100 emulsions. This lead us to believe that Marangoni instabilities had a more pronounced effect on SDS emulsions in bilgewater compared the Triton X-100 emulsions. The multi-scale approach of emulsion characterization proved to be beneficial for better understanding the emulsion stability. By combining with the innovative emulsion characterizing methods (e.g. CLSM and microsensors), the results provided better understanding of the effect of surfactant types and salinity in emulsion formation and stability for better management of bilgewater in shipboard applications.

Third, we discussed the characterization of a new photocatalyst using microsensors. Results showed that the rate of oxygen consumption by the MoS_2 had a linear relationship with ROS production (measured using XTT method). Therefore, microsensors represented a useful tool for characterizing photo-catalyst where photocatalyst performance can be evaluated in minutes rather than days. Using microsensor techniques we found that ROS production by the MoS_2 samples were not homogeneous and that active surface area may differ between samples. We also found that MoS_2 doped with Au/Pd and Pt showed significant improvement in ROS production over MoS_2 doped with Au or Cu or MoS_2 alone. Overall, we were able to prove that MoS_2 films with vertically-aligned 2D layers exhibit excellent visible light responsive photocatalytic activities for efficiently degrading organic compounds in contaminated water such as harmful algal blooms. We also demonstrated the visible light-driven rapid degradation of microcystin-LR, one of the most toxic compounds produced by the algal blooms, and revealed

that the degradation efficiency can be significantly improved by incorporating noble metals. This study exhibits a high promise of these emerging 2D materials for water treatment, significantly broadening their versatility for a wide range of energy and environmental applications.

In Chapter 6 and 7, we looked at developing microsensors for *in situ* monitoring of Zn^{2+} in plants. we have developed and characterized a solid contact micro-ion-selective electrode (SC- μ -ISE) for the determination of zinc transport in sour orange seedlings using a non-invasive microelectrode ion flux estimation (MIFE) technique. The SC- μ -ISE displayed a 26.05 ± 0.13 mV decade⁻¹ Nernstian response and a LOD of $(3.96 \pm 2.09) \times 10^{-7}$ M. Results showed a significant Zn^{2+} uptake in the leaves and roots of sour orange seedlings when bulk concentrations were higher than 5.99 mM. Above this concentration, a linear relationship between flux and bulk Zn^{2+} concentration was observed. This relationship suggests passive diffusion may be a key mechanism for Zn^{2+} transport into plants. Then we miniaturized square wave anodic stripping voltammetry into a microelectrode platform for measuring Zn^{2+} within the vascular bundle on citrus plants. Our results showed that the solid metal tip (110 μm in diameter) of the Bi/Pt microelectrode was durable enough to penetrate the thick skin of the citrus leaves and the developed Bi/Pt microelectrode was able to respond to Zn^{2+} in the midrib of a citrus leaves and distinguish the Zn^{2+} concentrations between Zn^{2+} treated and untreated samples with high resolution. It was found that the tip size can be optimized to reduce mass transport limitation and improve LOD. These novel tools can be used to further knowledge the effect of nutrient therapy and disease progression on HLB infected citrus plants.

Overall, the research presented in this dissertation demonstrates the importance of understanding of mass transport in environmental engineering and the usefulness of

microsensors for extending our current understanding of mechanisms and critical factors in natural and engineered systems.

Broader Impacts and Outlook

Impacts of this research transcends several disciplines of study. In the field of wastewater treatment engineering, the application of microsensors helped improve our understanding of algal-bacterial biofilm interactions that may one day lead to more sustainable wastewater treatment options. In the field of emulsion chemistry, information gained on how mass transport effects emulsion stability not only contributed to an improved scientific understanding of emulsion stability but may also lead to enhanced oily wastewater treatment. In the field of material science, microsensor characterization of photocatalysts allowed for rapid determination of ROS production and could change the way photocatalysts are studied. Lastly, in the field of agriculture, the developed Zn²⁺ microsensor demonstrated, for the first time, the rate of foliar uptake of zinc in citrus plants and the SWASV sensors showed the transport of zinc in the vascular bundle of plants. This work could one day lead to improved treatment options for HLB infected citrus.

Future research could further develop algal biofilm models for scale-up in terms of photo-aeration and advanced nutrient removal. Further development of mass transport of oxygen in photocatalytic systems could also improve advanced oxidation processes along with material developments. Lastly, additional research of the use of microsensors in citrus plants could be expanded to a plant and agriculture research were microsensors have not yet gained traction.

APPENDIX A: COPYRIGHT USE OF PUBLISHED MANUSCRIPTS



Title: In Situ Characterization of Oil-in-Water Emulsions Stabilized by Surfactant and Salt Using Microsensors

Author: Jared Church, Danielle M. Paynter, Woo Hyoung Lee

Publication: Langmuir

Publisher: American Chemical Society

Date: Sep 1, 2017

Copyright © 2017, American Chemical Society

LOGIN

If you're a [copyright.com user](#), you can login to RightsLink using your copyright.com credentials. Already a [RightsLink user](#) or want to [learn more?](#)

PERMISSION/LICENSE IS GRANTED FOR YOUR ORDER AT NO CHARGE

This type of permission/license, instead of the standard Terms & Conditions, is sent to you because no fee is being charged for your order. Please note the following:

- Permission is granted for your request in both print and electronic formats, and translations.
- If figures and/or tables were requested, they may be adapted or used in part.
- Please print this page for your records and send a copy of it to your publisher/graduate school.
- Appropriate credit for the requested material should be given as follows: "Reprinted (adapted) with permission from (COMPLETE REFERENCE CITATION). Copyright (YEAR) American Chemical Society." Insert appropriate information in place of the capitalized words.
- One-time permission is granted only for the use specified in your request. No additional uses are granted (such as derivative works or other editions). For any other uses, please submit a new request.

**JOHN WILEY AND SONS LICENSE
TERMS AND CONDITIONS**

Jun 11, 2018

This Agreement between University of Central Florida -- Jared Church ("You") and John Wiley and Sons ("John Wiley and Sons") consists of your license details and the terms and conditions provided by John Wiley and Sons and Copyright Clearance Center.

License Number	4365951041503
License date	Jun 11, 2018
Licensed Content Publisher	John Wiley and Sons
Licensed Content Publication	Electroanalysis
Licensed Content Title	Development and Characterization of Needle-type Ion-selective Microsensors for in situ Determination of Foliar Uptake of Zn ²⁺ in Citrus Plants
Licensed Content Author	Jared Church, Stephanie M. Armas, Parth K. Patel, et al
Licensed Content Date	Dec 4, 2017
Licensed Content Volume	30
Licensed Content Issue	4
Licensed Content Pages	7
Type of use	Dissertation/Thesis
Requestor type	Author of this Wiley article
Format	Electronic
Portion	Full article
Will you be translating?	No
Title of your thesis / dissertation	Electrochemical microsensors for in situ monitoring of chemical compounds in engineered and natural aquatic systems
Expected completion date	Aug 2018
Expected size (number of pages)	180
Requestor Location	University of Central Florida 12800 Pegasus Drive, Suite 211 ORLANDO, FL 32816 United States Attn: Jared Church
Publisher Tax ID	EU826007151
Total	0.00 USD
Terms and Conditions	

**APPENDIX B: SUPPLEMENTAL INFORMATION: APPLICATION OF
MICROSENSORS TO ALGAL-BACTERIAL BIOFILMS FOR
ADVANCED WASTEWATER TREATMENT**

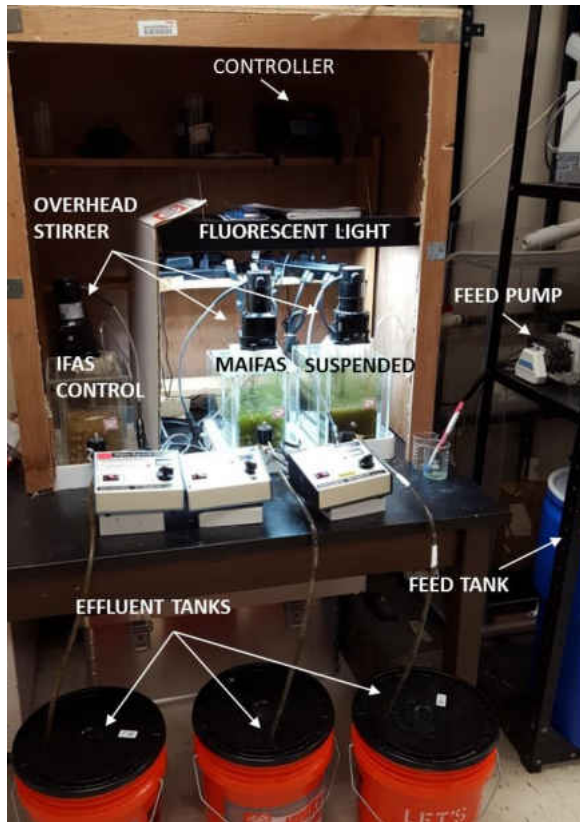


Figure B1. Experimental set-up of IFAS control, MAIFAS, and suspended algae-bacteria reactors.

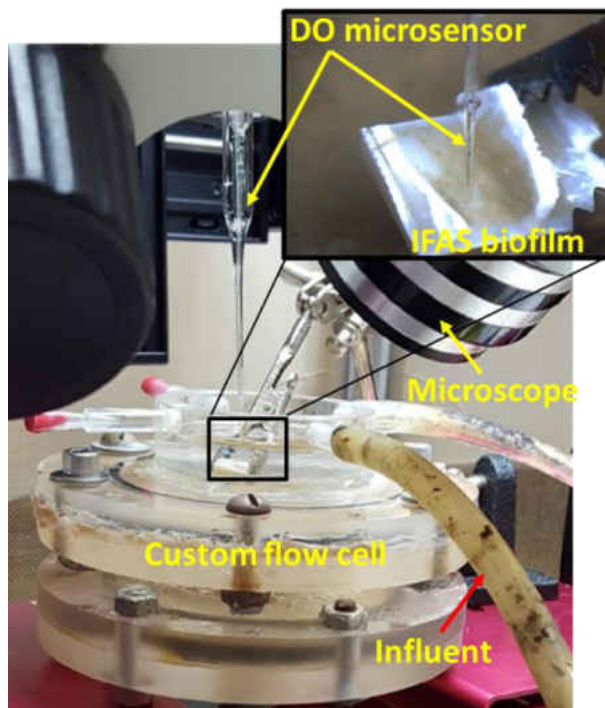


Figure B2. DO concentration microprofile measurements of IFAS biofilm.

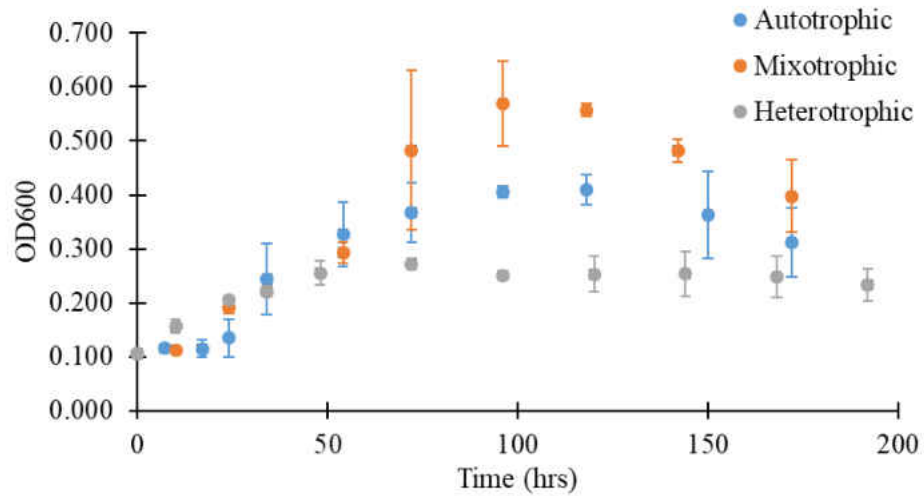


Figure B3. Concentration of *C. vulgaris* under autotrophic (BBM + light), mixotrophic (BBM + light + glucose) and heterotrophic conditions (BBM + glucose + dark).

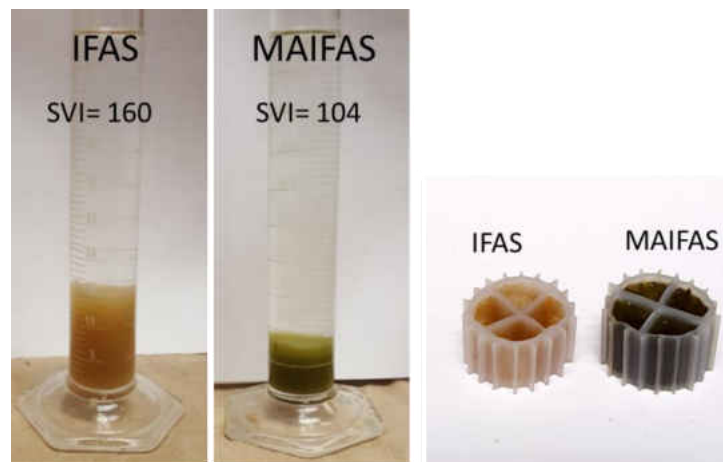


Figure B4. Settling test of IFAS and MAIFAS sludge and biofilm formations between IFAS and MAIFAS media.

**APPENDIX C: SUPPLEMENTAL INFORMATION: APPLICATION OF
MICROSENSORS TO BILGE WATER EMULSIONS FOR *IN SITU*
CHARACTERIZATION**

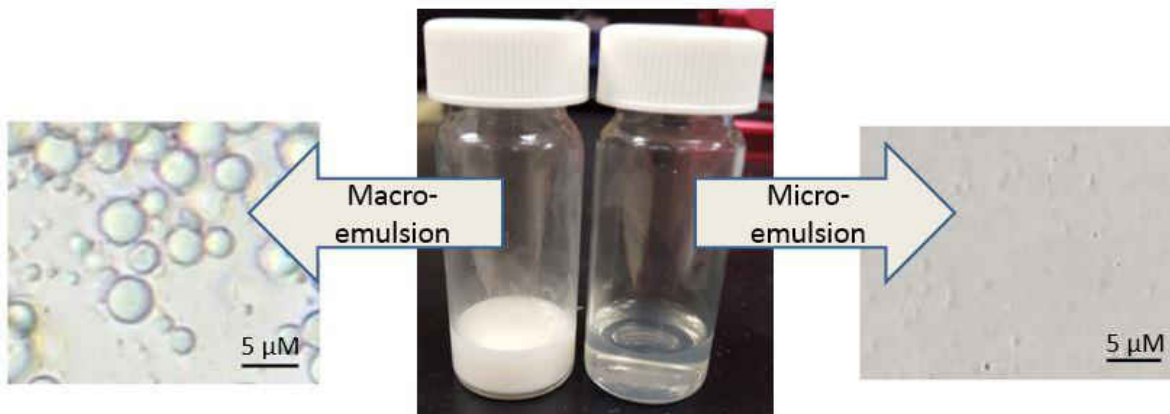


Figure C1. Synthetic oil-in-water macro and microemulsion samples prepared using 0.1% NSBM#4 and 100 ppm Triton X100.

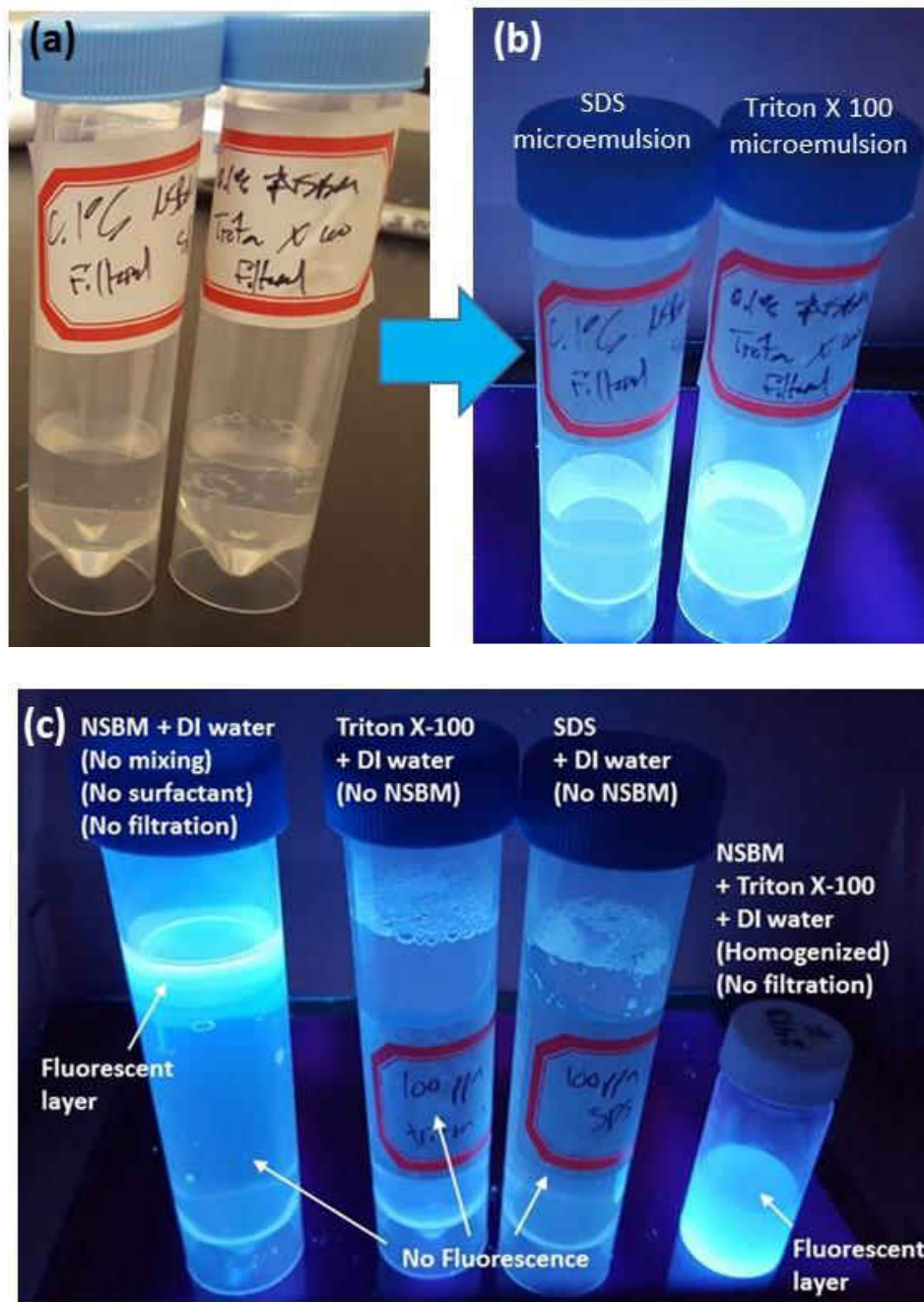


Figure C2. Fluorescence of emulsions. (a) photographs of SDS microemulsion and Triton X-100 microemulsion, (b) photographs of microemulsion samples under UV light, and (c) photographs of various oil and water samples under UV light.

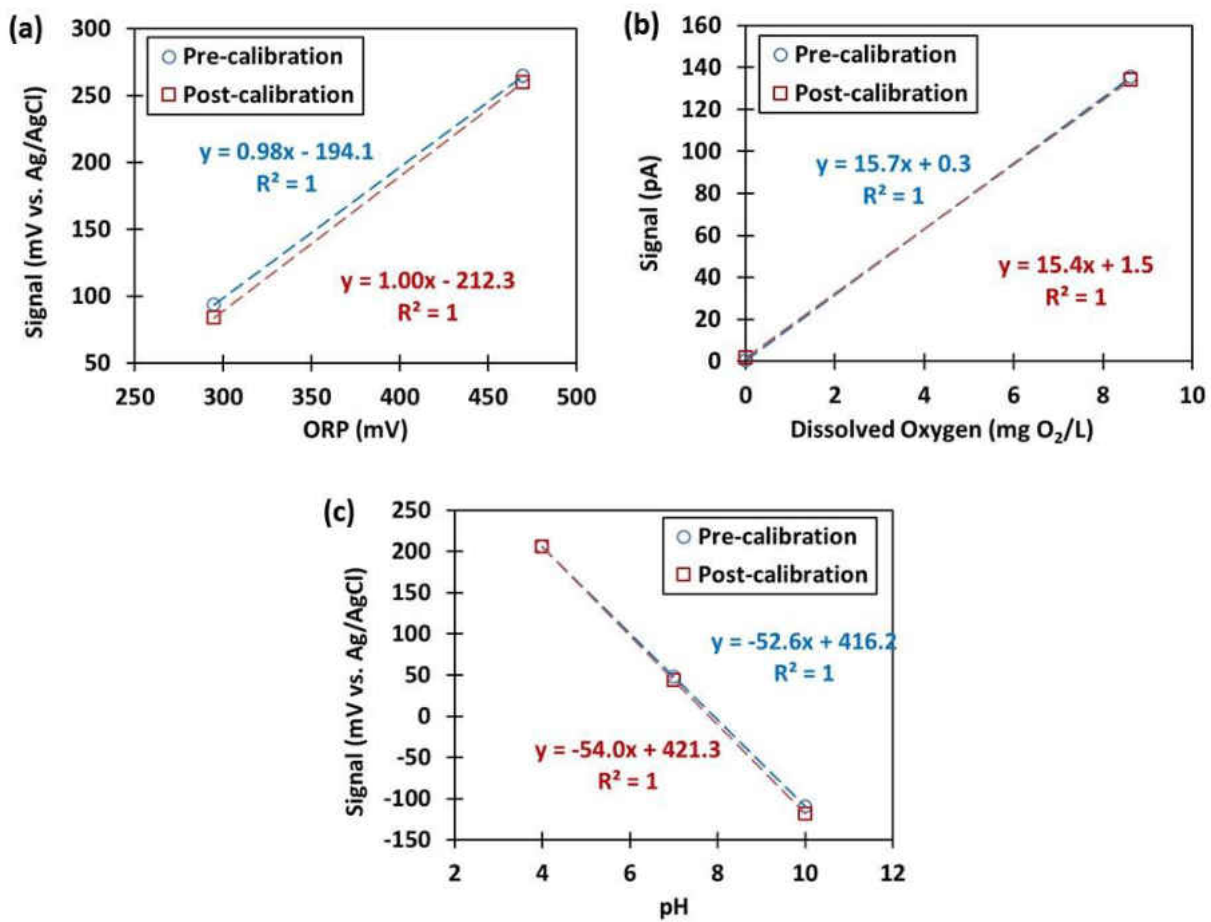


Figure C3. Calibration curves before and after emulsion sample profiling for (a) ORP, (b) DO and (c) pH microsensors.

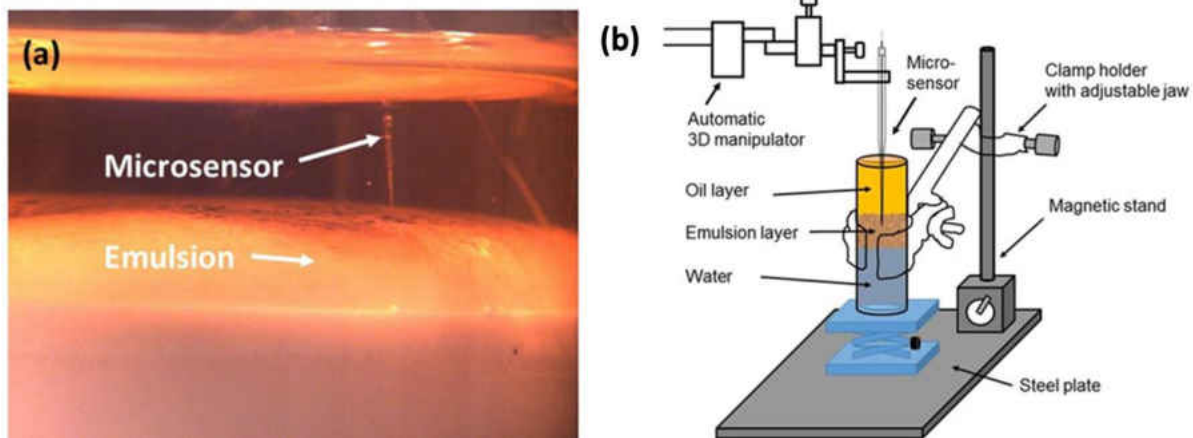


Figure C4. Microsensor emulsion characterization experimental set up. (a) a microscopic image of microsensor approaching to emulsion layer. (b) a schematic diagram of experimental set up.

Contact angle measurements. Contact angle measurements of surfactant water on glass (quartz) substrate was not possible because the glass substrate used in the test is hydrophilic and surfactants are inherently water soluble (hydrophilic) based on their hydrophilic-lipophilic balances (HLB). Therefore, the contact angle of surfactant water was measured in NSBM #4 solution (surrounding media) (Fig. S5). Samples prepared using Triton X-100 showed dynamic changes over time and contact angles of Triton X-100 solution decreased over time from 160 to 92° (Fig. S6). This decrease is much slower in higher salinities probably due to increased ion strength. The static contact angles for Triton X-100 solutions were measured after 60 seconds.

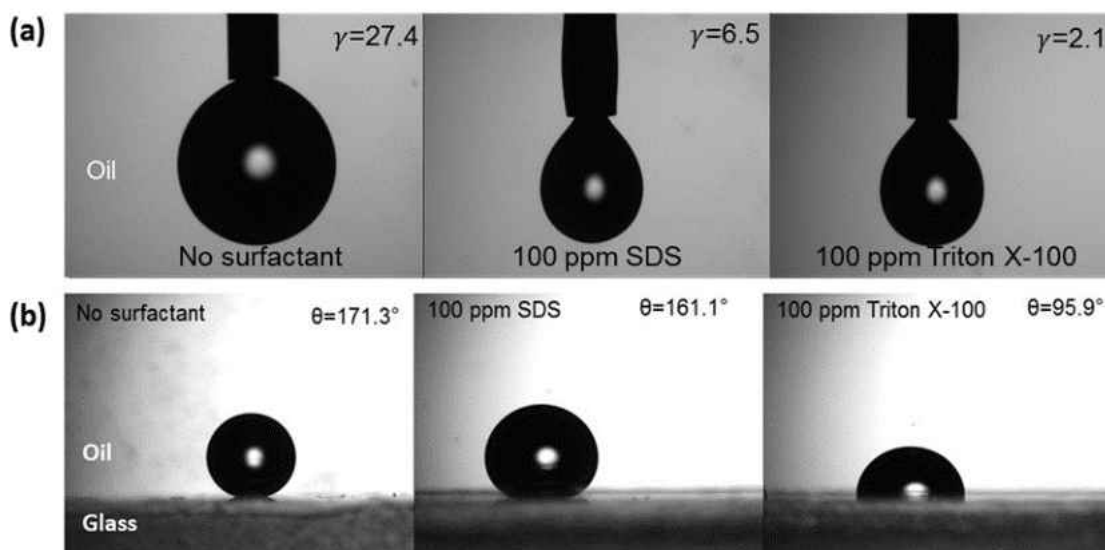


Figure C5. Photographs of (a) water-in-oil pendant drops and (b) contact angle for no surfactant, SDS (100 ppm) and Triton X-100 (100 ppm) at 10^{-4} M NaCl in NSBM#4. Surrounding media in all tests was NSBM#4.

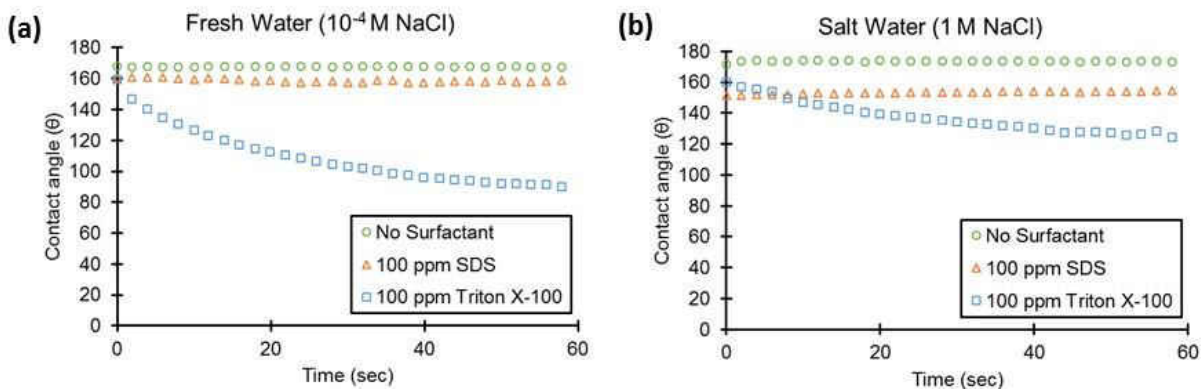


Figure C6. Contact angles of no surfactant (DI water only), SDS, and Triton X-100 solutions over time in (a) 10⁻⁴ M and (b) 1 M NaCl in NSBM#4.

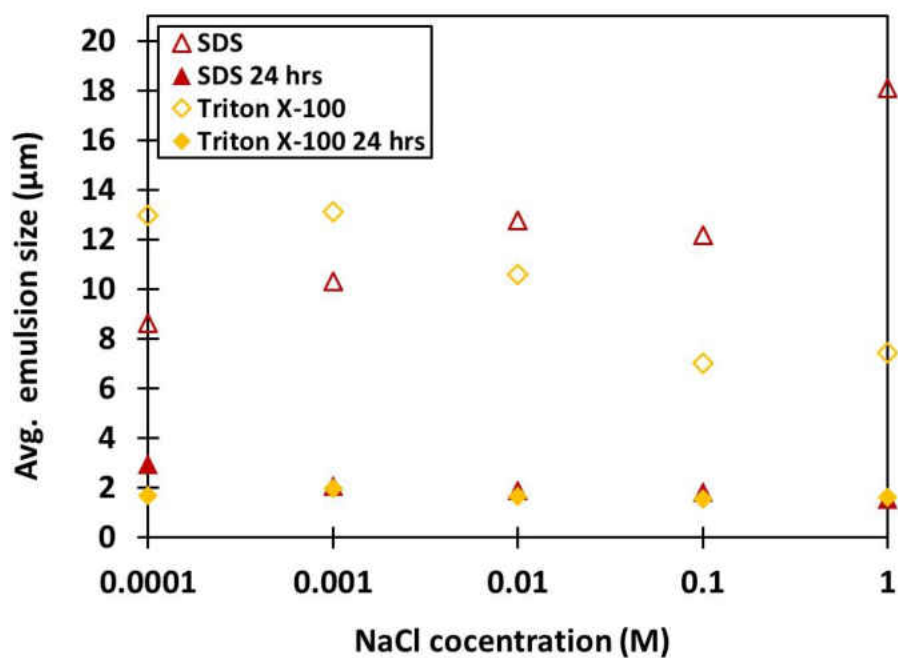


Figure. C7. Average emulsion size (n=20) a function of NaCl concentration at the initial and 24 hrs time intervals. Two different emulsion samples were prepared with SDS and Triton X-100. All samples were taken at the middle of the emulsion layer. At least 20 emulsion droplets were measured and averaged for each condition.

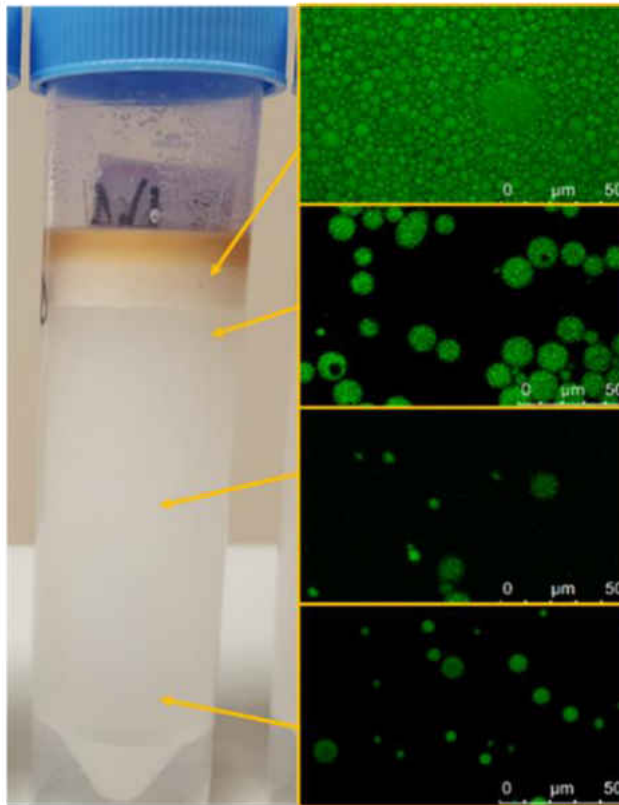


Figure C8. CLSM images of spatial emulsion distribution at different locations. The sample was prepared with 100 ppm Triton X-100 solution and 1% NSBM #4 (no NaCl). The top CLSM image was taken from the cream layer, showing a high density of emulsion droplets, while the emulsion droplets at the bottom layer are scattered.

Microsensor performance validation in oil-water mixture. To validate the electrochemical microsensor performance in oil-water mixtures, a well-known microsensor, a DO microsensor, was used under various oil-water conditions. The DO microsensor is the Clark type sensor combined with a reference electrode in the same casing and was expected to provide stable signals (pA) for oxygen contents regardless of the phase being measured (e.g. gas, oil, or aqueous phase). A simple experiment was designed to measure oxygen concentrations through an air, oil, and water phase. Measurements for all oxygen microprofiles were conducted at 100 μm interval with 30 seconds of wait time between each measurement for signal stabilization. Duplicate profiles were averaged together to obtain the DO profile and three signals were taken for each distance during each profile. First, an oxygen microprofile was measured in a sample that contained a top layer of mineral oil and a bottom layer of DI water saturated with oxygen (21% DO). Oxygen has a known solubility of 3,345 $\mu\text{L/L}$ in mineral oil (1); thus, it was expected that oxygen can be measured in the mineral oil layer. In a saturated condition, oxygen concentrations in all three phases were around 21% DO (Figure C9). A similar oxygen microprofile was also measured using NSBM #4 instead of mineral oil and the result was similar. Then, oxygen microprofiles were measured in a different sample that contained a top layer of mineral oil and a bottom layer of DI water with the addition of oxygen scavenger (0.1 M ascorbic acid). It was clear that there are two diffusion processes occurring, one within the water phase and one within the oil phase. A similar profile was taken using NSBM #4 and DI water with an oxygen scavenger and the similar trend was observed throughout the oil and water phases. These profiles clearly showed a diffusion of DO from the oil phase (21%) to the water phase (0%) with the oxygen scavenger. The test proved that the electrochemical sensor technique is appropriate for characterizing emulsion stability and chemical species transport from oil to

water or water to oil phases.

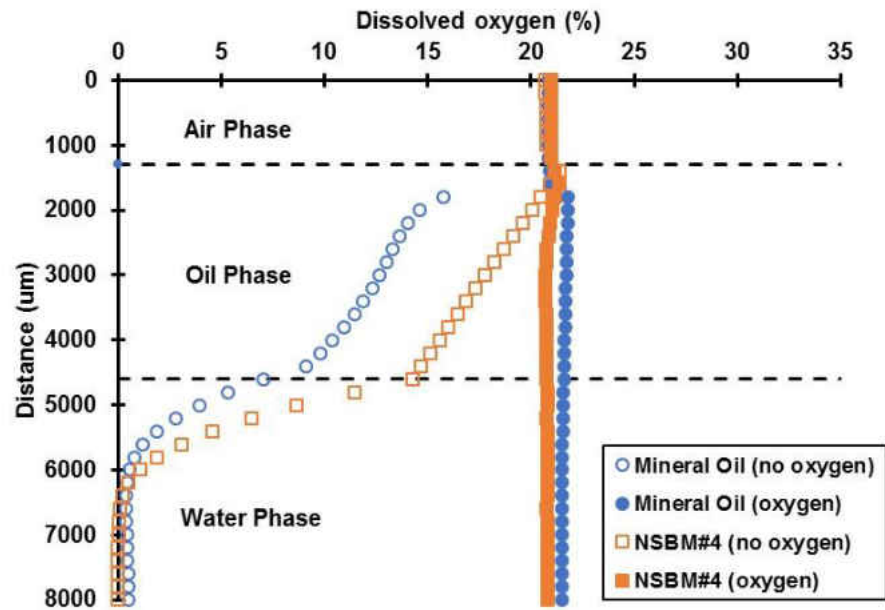


Figure C9. DO microprofiles through an air, oil and water phase. The water phase was fully saturated with oxygen (21% DO) or containing no oxygen (0% DO).

A. Müller, M. Jovalekic, and S. Tenbohlen, "Solubility Study of Different Gases in Mineral and Ester-based Transformer Oils," in *Condition Monitoring and Diagnosis (CMD), 2012 International Conference on*, 2012, pp. 937-940.

**APPENDIX D: SUPPLEMENTAL INFORMATION: APPLICATION OF
MICROSENSORS FOR CHARACTERIZATION OF A NOVEL NOBLE
METAL-COATED MoS₂ NANOFILM PHOTOCATALYST FOR
DEGRADATION OF EMERGING WATER CONTAMINANTS**

MoS₂ adsorption model

Several well-known adsorption models (pseudo first order, pseudo second order, Elovich, Avrami and fractional power models) were fit to the experimental data and validated using Chi square and normalized standard deviation. The Type II pseudo second order adsorption model best represented our data ($X^2=2.45*10^{-6}$, $R^2=1$). This model is the most commonly used mathematical expression for the kinetic data monitored in solid/solution sorption systems¹⁻³. The nonlinear form of pseudo second order adsorption is shown in the following equation:

$$q(t) = \frac{k_2 q_e^2 t}{1 + k_2 q_e t}$$

Where $q(t)$ and q_e are the total adsorbed amounts of MC-LR per surface area of sorbant at time t and equilibrium, respectively. K_2 and q_w were determined by plotting $1/q(t)$ vs. $1/t$. Pt-MoS₂ catalysts displayed faster kinetics compared to Au/Pd-MoS₂ catalysts ($K_2=0.47$ vs. $K_2=0.57 \mu\text{g cm}^{-1} \text{hr}^{-1}$) and had higher absorption capacity ($q_e=0.871 \mu\text{g cm}^{-1}$ vs. $q_e=1.40 \mu\text{g cm}^{-1}$). The figure below shows that once the samples are illuminated the MC-LR kinetics are increased and exceed the adsorption equilibrium predicted by the dark adsorption model. This finding shows that MC-LR degradation is a function of both adsorption and photocatalytic reactions.

As we clarified that there is no noticeable production of ROS which is to come from the photo-excited e-h pair generation in the catalysts, this observation evidences the insignificant “dark” removal of MC-LR driven by photocatalytic reactions, which, in turn, strongly supports the adsorption-driven degradation in dark.

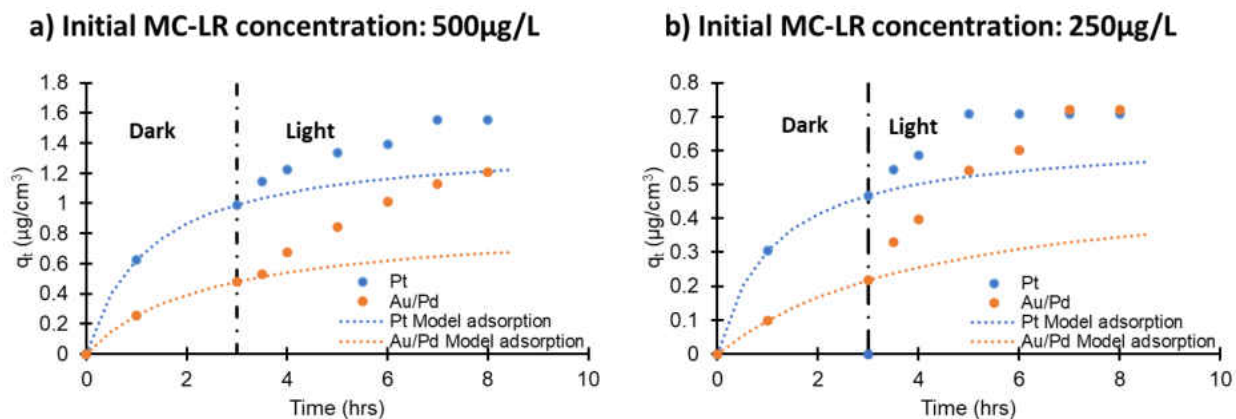


Figure D1. Type II pseudo second order adsorption model and experimental data of MC-LR adsorption to MoS₂ films

ROS monitoring using XTT

To monitor ROS production by MoS₂, the possibility of superoxide radical anion (O₂^{•-}) production from MoS₂ was monitored using XTT (2, 3-bis (2-methoxy-4-nitro-5-sulphophenyl)-2H-tetrazolium-5-carboxanilide, Fluka). XTT can be reduced by superoxide radical anions (O₂^{•-}) to generate water-soluble XTT-formazan with the maximum absorption at 470 nm⁴. Thus, an increase in absorption at 470 nm indicates an increase of ROS concentration. Figure 1 shows a preliminary data of ROS production. Au/Pd coated-MoS₂ with vertically aligned layers shows higher production of ROS compared to control and MoS₂ only within a time frame of 4 hours.

Before photoreaction tests, it was confirmed that there is no ROS production under dark condition using XTT. The sample was colorless throughout the control check in dark which is the same as MoS₂ only and Si only as shown in Figure D2.

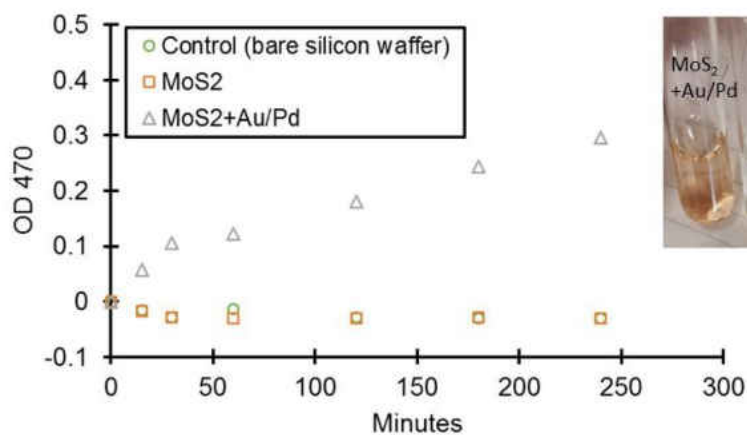


Figure 1. Absorbance of XTT-formazan at 470 nm as a method to monitor the production of ROS from MoS₂, Au/Pd modified MoS₂ nanofilms and a substrate only (silicon wafer without MoS₂ as a control). The surface area of each nanofilms was identical with 3 cm². 40 mL of XTT (0.4 mM) dissolved in phosphate buffered saline was used to submerge the samples while being exposed to 16,000 lx continuous cool-white fluorescent light illumination. Before tests, it was confirmed that there is no ROS production under dark condition using XTT.

**APPENDIX E: SUPPLEMENTAL INFORMATION: CHAPTER 7: A
NOVEL APPROACH FOR *IN SITU* MONITORING OF Zn²⁺ IN CITRUS
PLANTS USING TWO-STEP SQUARE WAVE ANODIC STRIPPING
VOLTAMMETRY**

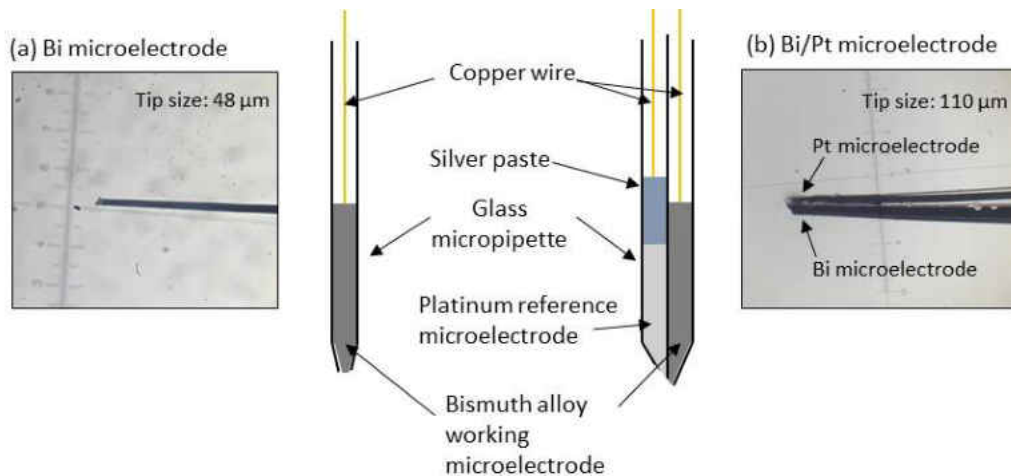


Figure E1. A schematic diagram and microscopic images of (a) the developed single barrel Bi microelectrode and (b) the double barrel Bi/Pt microelectrode for the detection of Zn^{2+} in citrus plants

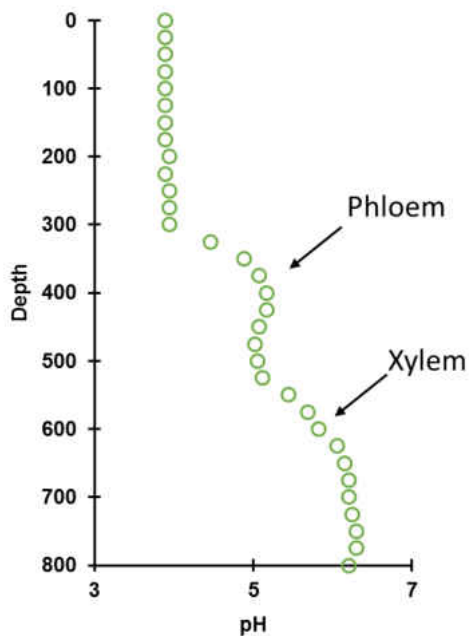


Figure E2. A representative pH microprofile of the midrib of a sour orange leaf using a pH microsensors.

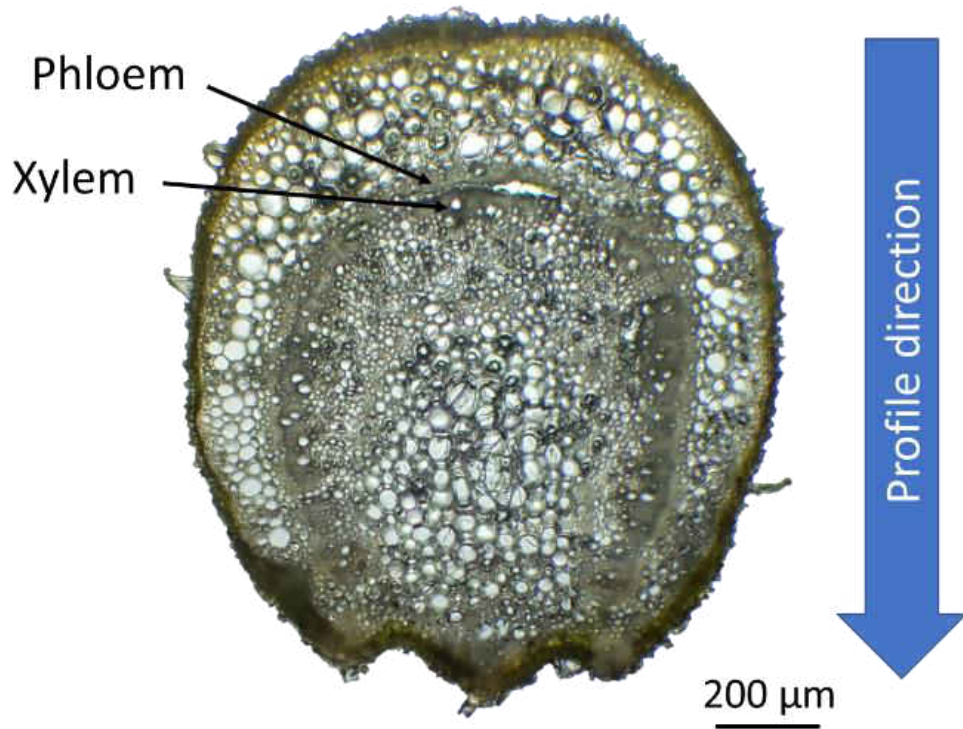


Figure E3. A cross-sectional photograph of a sour orange seedling leaf stem at 100x magnification.

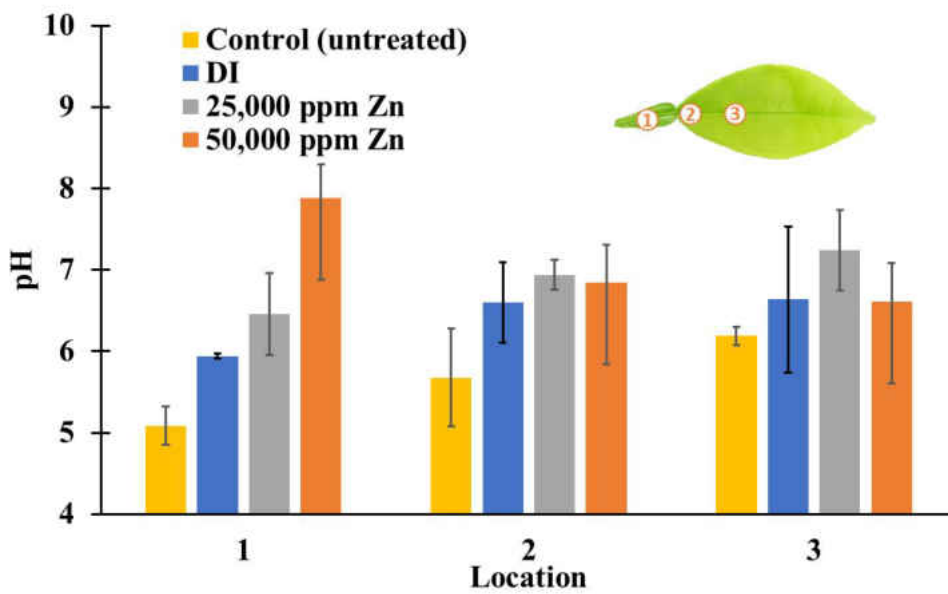


Figure E4. *In situ* pH measurements of a sour orange vascular bundle using a pH microsensor after 6 hours of exposure to various zinc treatments. $Zn(NO_3)_2$ was used for the zinc treatments.

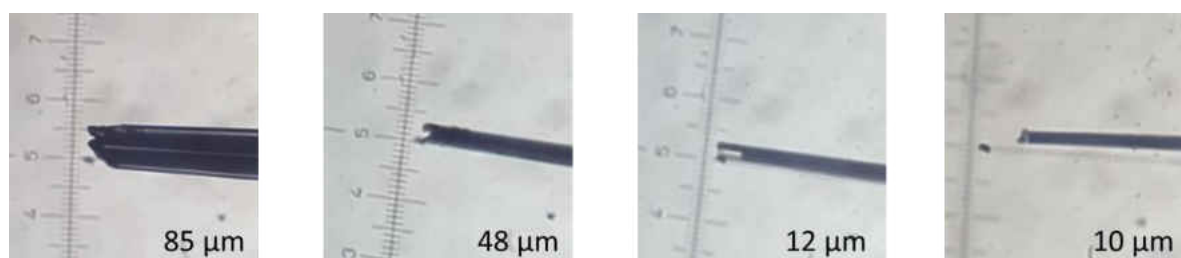


Figure E5. Microscopic images of bismuth microelectrodes for determination of tip size effect and recess on mass transport effects of SWASV response to zinc.

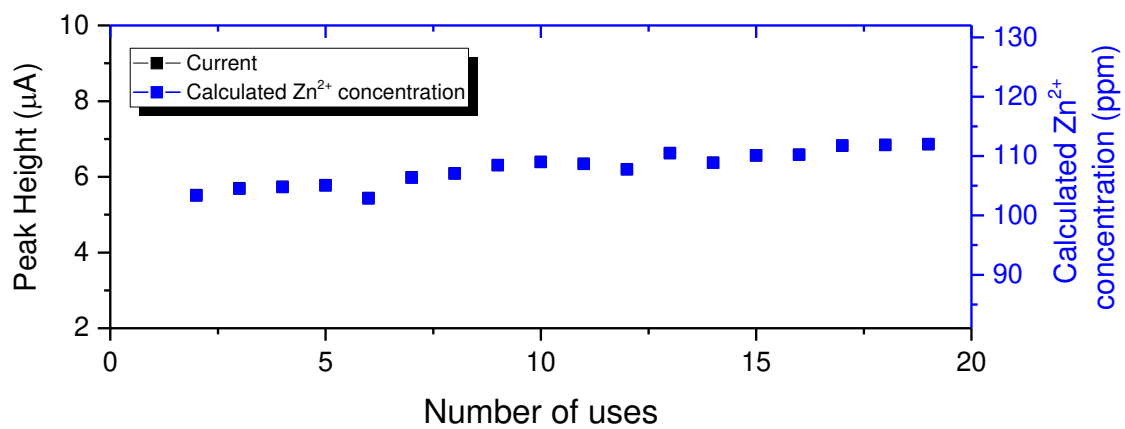


Figure E6. Response of bismuth sensor to 100 ppm Zn²⁺ over 18 uses